Design, Manufacturing and Testing of SMA-Based Smart and Cellular Structures

A thesis submitted for the degree of Doctor of Philosophy

July 2006

Mohd Roshdi Hassan

Department of Mechanical Engineering

University of Sheffield

Abstract

This work illustrates the design, manufacturing and testing of a novel concept of honeycomb made from Shape Memory Alloy (SMA). The aim of the work is to incorporate SMA into auxetic structure to create a new concept for a future deployable structure. An auxetic structure is a structure that exhibits a negative Poisson's ratio effect. The auxetic structures involved in this work include re-entrant and chiral honeycombs. The honeycombs, which include hexagonal honeycomb, are manufactured using NiTiCu SMA ribbons. Tensile tests at room temperature were performed on the hexagonal and re-entrant honeycomb. Finite element simulations have been carried out for the honeycomb. Cellular Material Theory (CMT) has been used to describe the linear elastic behaviour of the honeycombs. Good agreement is observed between numerical nonlinear simulations and the experimental results. An analysis of the Poisson's ratio effect of the honeycomb is also presented in this thesis. The work also involved describing the thermally induced transformation equivalent viscoelastic damping of NiTiCu SMA ribbon. The Dynamic Mechanical Analysis test has been carried out at different frequencies and temperatures, with increasing and decreasing temperature gradients. Thermally induced transformations (austenitic and martensitic) provide damping peaks at low frequency range excitations, while storage modulus is not affected by the harmonic pulsation. As the SMA ribbon increases its stiffness, the damping capacity reduces, and the loss factor drops dramatically at the austenite finish temperature.

Acknowledgements

Contents

1.0   INTRODUCTION

2.0   LITERATURE REVIEW – Shape Memory Alloys

6.0   SMA HONEYCOMB TESTING AND RESULTS

7.0   DISCUSSIONS

Nomenclatures

SMA	-	Shape Memory Alloys
NiTiCu	-	Nickel Titanium Copper
SME	-	Shape memory effect
TWSME	-	Two-way shape memory effect
DSC	-	Differential Scanning Calorimeter
DMA	-	Dynamic Mechanical Analysis
θ	-	Internal cell angle
α	-	Aspect ratio
β	-	Relative thickness
Mf	-	Martensite finish temperature
Ms	-	Martensite start temperature
As	-	Austenite start temperature
Af	-	Austenite finish temperature
E^*_X	-	elastic modulus in X direction
$(\sigma^*_{pl})_X$	-	elasto-plastic stress in X direction
E^*_Y	-	elastic modulus Y direction
$(\sigma^*_{pl})_Y$	-	elasto-plastic stress in Y direction
ν	-	Poisson's ratio

List of Figures

List of Tables

List of Publications

Hassan, M.R., Scarpa, F., Mohamed, N.A., 2006, In plane tensile behaviour of shape memory alloys hexagonal Honeycomb. Accepted Journal of Intelligent Material Systems and Structures.

Remillat, C., **Hassan, M. R.**, Scarpa, F., 2006, Small Amplitude Dynamic Properties of $Ni_{48}Ti_{46}Cu_6$ SMA Ribbons - Experimental Results and Modelling, Journal of Engineering Materials and Technology, Volume 128, Issue 3, pp. 260-267

Hassan, M.R., Scarpa, F.L., Mohamed, N.A., 2004, Shape memory alloys honeycomb: design and properties, Proc. SPIE Int. Soc. Opt. Eng. 5387, 557

Hassan, M.R., Scarpa, F., Mohamed, N.A., 2005, Conventional and Auxetic SMA Cellular Structures, IMECE2005-81075, ASME International Mechanical Engineering Congress and Exposition, Florida USA

Scarpa, F.L., **Hassan, M.R.**, Ruzzene, M., 2006, Modelling and testing of shape memory alloy chiral honeycomb structures, Proc. SPIE Int. Soc. Opt. Eng. Smart Structures and Materials 2006: Active Materials: Behaviour and Mechanics, Vol. 6170, Edited Armstrong

Hassan, M.R., Scarpa, F., Mohamed, N.A, Ruzzene,M, 2006, In-plane tensile properties of shape memory alloy hexagonal chiral honeycombs, Submitted to First International Conference on Auxetics and Anomalous Systems, 4 - 6 September 2006, Exeter, UK

Hassan, M.R., Scarpa, F., Ruzzene, M., Mohamed, N.A, 2006, Smart Shape Memory Alloys Chiral Honeycomb, submitted to The 7th European Symposium on Martensitic Transformations and Shape Memory Alloys, 10-15 September 2006 Bochum, Germany

Chapter 1

INTRODUCTION

1.1 Motivation for research

With the introduction of the De Havilland Mosquito in 1941, honeycomb materials have been used in lightweight aircraft construction. Since the end of the Second World War, sandwich structures using a cellular core have been applied also in ship building and rail vehicle construction. For a given weight, a sandwich structure offer better flexural strength and stiffness than a uniform construction. The ability of the core to maintain the separation of the face layer and to resist excessive shear is the key to the performance of the structure [Zenkert, 1997]. Foams and honeycomb structures are normally used as core materials or spacers for sandwich constructions. Honeycomb materials have been used since the second half of the 20th century because of their low mass and high shear stiffness. Sandwich panels are increasingly used on the airframe and spacecraft components such as deployable antennae on satellites [Taylor et.al, 1999]. The properties of such structures can be modified by altering the topology and core material.

The topology of honeycomb cores is defined by the unit cell, typically a shape with two axes of symmetry, which is repeated along one or two principal direction. Cores can be made from a variety of materials ranging from 2024 aluminum alloy to aramid paper, cardboard and recently carbon fibre composites [Hexcel Composites, 2005].

Over the last 20 years significant effort has been made to identify topologies of cellular structures that are able to provide enhanced mechanical and multifunctional characteristics. Amongst the new topologies proposed of particular interest are cellular structures featuring negative Poisson's ratio (NPR) characteristics. Negative Poisson's ratio behaviour does not contradict the laws of classical elasticity but provides an unusual volume deformation. This type of structure also defined as auxetic [Evans et.al, 1991], the term come from the Greek word, $\alpha\upsilon\xi\varepsilon o\sigma$, which means increase or grow. The use of an auxetic core offers the enhancement of some multifunctional characteristics, such as, for example, increased indentation resistance, augmented sound absorption and the possibility of designing tuned sandwich structures with selective acoustic and radar signatures.

In recent years, another major area of research has been the study and the introduction of smart materials and structures in several areas of technology. Smart materials are a range of new or modern solids whose properties or characteristics can be altered or controlled by modifying the environment in which they work [Gandhi and Thompson, 1992]. These materials have the ability to change their shape, rheological properties (like stiffness and

damping), or to change their internal electrical properties like dielectric constant or resistivity. With the application of the so-called "smart materials", engineering components may be able to modify their mechanical and physical characteristics, at different scale levels, in an autonomous way or when subjected to mechanical, electric, magnetic or thermal loading.

1.2 Smart Materials

Smart materials can come in a variety of sizes, shapes, compounds and functions. They can be considered, as the ultimate shape shifters, being able to alter their physical form, monitor their environment, and even diagnose their own internal condition. They can also perform all these tasks while interacting with the objects and operators around them. Although many smart materials and solids are currently under development, only a few are produced commercially at present. In some cases, the properties of these solids have long been known but only have recently their microstructure and manufacturing been refined for smart structures applications.

Amongst the smart materials categories currently accepted in the scientific literature [Culshaw,1996] one has to mention piezoelectrics, electrostrictive materials, shape memory materials, magnetostrictive materials, electrorheological and magnetorheological fluids and fibre optics. In a recent Material Foresight report, negative Poisson's ratio material has been included as part of the smart materials group [Davies, 2004]. Table 1.1 shows the summary of external response and stimuli for smart materials in the report.

Detailed explanations of some smart materials have been provided in Appendix A.

Response Stimulus	Electrical	Magnetic	Optical	Thermal	Mechanical
Electrical			Electrochromic Electroluminescent Electo-optic	Thermoelectric	Piezoelectric Electrostrictive ER fluids
Magnetic			Magneto-optic		MR fluids Magnetostrictive
Optical	Photoconductor		Photochromic		
Thermal			Thermochromic Thermoluminescent		Shape memory
Mechanical	Piezoelectric Electrostrictive	Magnetostrictive	Mechanochromic		Negative Poisson ratio

Table1.1:Stimulus-response matrix for selected smart materials[Davies, 2004]

A special subset of smart materials (and so far, probably the most successful in terms of market applications) is the one related to Shape Memory Alloy (SMA) materials. The term SMA is referred to a group of metallic materials that demonstrate the ability to return to some previously defined shape or size when subjected to the appropriate thermal procedure.

Recent attempts have been made at designing and manufacturing "smart honeycombs". Boundless Corporation (Boundless Corporation, Colorado) has recently introduced a structural battery design that can be embedded into hexagonal centresymmetric honeycombs, typically used in spacecraft. Truss core solutions [Sypeck and Wadley, 2002] have been proposed for optimised bulk lightweight sandwich concepts with enhanced thermal dissipation

capabilities. A transducer based on a ceramic honeycomb configuration with end caps made of thin layers of epoxy has demonstrated significantly high hydrostatic piezoelectric response [Zhang et.al 1996]. However, a honeycomb structure made of smart material with full structural capabilities has not been designed yet.

Payload and size are major constraints in the satellite industry. By using a SMA auxetic cellular solid, the structure can be compressed in a small volume and can be deployed into space. This solution would provide an alternative to inflatable deployable solutions, such as modular mesh deployable, balloon type portable and aperture unfurlable antennas. The shape restoring capabilities are also a feature that could be successfully employed in structural energy absorption applications. Currently, honeycomb structures are used in packaging, railway and aerospace industries in crashworthiness applications because of their energy absorption capabilities at different rates of loading [Gibson and Ashby, 1997]. However, a crushed and densified honeycomb does not retain its structural function. It is conceivable to design a cellular core with shape memory capabilities that, once heavily loaded, tends to return or oppose the external force and maintain to a certain extent its structural integrity capabilities.

1.3   Objectives of Research

The main objective of this work is to obtain a new functional structure combining the honeycomb topology and the use of shape memory alloys as core material for the new cellular solid. This new structure can be used for new type of deployable antenna reflectors, or in packaging applications to store strain energy during impact loading. Moreover, if the effective Poisson's ratio of the smart SMA cellular structure is made negative by using specific cell shapes, a domed or synclastic curvature can be achieved naturally [Evans,1990].

The work of this thesis describes the manufacturing and in-plane testing of centresymmetric and noncentresymmetric (chiral) honeycomb structures made of SMA Nitinol ribbons. Specifically, the analysis of the chiral honeycomb was related to the behaviour of the in-plane Poisson's ratio under large strains. Also, a set of finite element models using pseudoplastic and pseudoelastic material models has been developed to simulate the in-plane mechanical tensile properties and the Poisson's ratio behaviour under nonlinear material and geometric loading conditions. The numerical and experimental results are discussed, and recommendations related to the design and future directions of the work made.

In parallel to the static testing of the honeycomb samples produced, a viscoelastic analysis of the SMA ribbons used to manufacture the cellular structures has been performed. The rationale behind this part of the work is

the impact that random vibrations can have on the structural integrity of sandwich structures, such as the ones used in deployable antennas for satellites and space payloads. Random vibrations can induce fatigue-related failure in sandwich structures. Also, when the structural component is subjected to high-energy spectra related to frequencies close to the resonance ones further failure phenomena could occur.

The knowledge of damping properties is therefore needed if one wants to propose these cellular structures for aerospace applications. The peculiar nature of shape memory alloys, i.e., their dependence versus applied mechanical and thermal loading, also provides added damping mechanisms compared to "classical" material cores used in commercial honeycombs. The viscoelastic study has been carried using a dynamic mechanical analysis (DMA) over a specific range of frequency and temperature bandwidth. The results have shown the presence of peak loss factors during the temperature loading at small dynamic strains of significant value during phase transformation from martensite to austenite. These results are significant in the field of SMA ribbons, because attention so far has been placed on the equivalent damping under pseudoelastic behaviour (i.e., the typical deformation regime of SMA actuators and dampers), while small strain loading has been neglected.

1.4 Summary of Thesis

There were two major works in this research. First was the study of shape memory alloy ribbon and it behaviour including the damping properties of the material. Second was the design and analysis of SMA honeycomb. This included normal hexagonal honeycomb and auxetic honeycomb. The following paragraphs give a summary of the way in which the thesis is organised.

Chapter 1 relates to the scope and the objective of the work, providing an overall description of smart materials within the context of this work. The Chapter provides also an explanation about the general layout of the thesis.

Chapter 2 relates to the literature review of Shape Memory Alloy materials. The Chapter describes a general background of SMA materials and mechanics, with descriptions of constitutive modelling used within the context of this work. A brief explanation about the phenomenological modelling of SMA can be found in Appendix B.

Chapter 3 provides a literature review of honeycomb structures exhibiting positive and negative Poisson's ratio (auxetic) behaviour. The auxetic honeycombs developed and described in this work are the re-entrant centresymmetric and hexagonal chiral honeycomb configurations.

Chapter 4 describes the numerical modelling developed in this work. In particular, a description on how to model SMA behaviour in commercial finite element software, like ANSYS, is performed.

Chapter 5 describes the properties and testing for SMA ribbon. This chapter will explain about the mechanical and thermal properties of SMA and also the testing that has been involved. It also shows the results of the tests related to the SMA ribbon composing the core of the honeycombs, such as tensile static and DMA tests. This Chapter also desribes the results of the finite element modelling related to the SMA ribbon only.

Chapter 6 has been divided into two parts. The first part describes the manufacturing processes used to produce the SMA honeycombs and the experimental tests performed in this research. The second part presented the numerical and experimental results related to SMA honeycomb tensile loading, including modelling of the quasistatic mechanical loading and in-plane Poisson's ratio measurements.

Chapter 7 provides the discussions of the results. The first part of the chapter relates to the SMA ribbon behaviour, including damping properties of SMA material at low amplitude dynamic strains. The second part provides discussions on the results from the finite element modelling of the SMA ribbon. The last part is related to the SMA honeycombs, including comparisons between numerical and experimental results on the tensile loading and Poisson's ratio of auxetic honeycombs.

Chapter 8 provides the conclusions and proposes recommendation for future work.

Some explainations about types of smart material and finite element programs for ANSYS are presented inside the Appendices.

Chapter 2

LITERATURE REVIEW- Shape Memory Alloys

2.1   Background of shape memory alloys

In 1932, the Swedish physicist Arne Olander discovered an interesting phenomenon when working with an alloy of gold (Au) and cadmium (Cd). The Au-Cd alloy could be plastically deformed when cool and then be heated to return to, or "remember", the original dimensional configuration. This phenomenon is known as the Shape Memory Effect (SME) and the alloys that exhibit the behaviour are called Shape Memory Alloys (SMA). In 1958 Chang and Read demonstrated the Shape Memory Effect at the Brussels World Fair. Specifically, they showed that the SME could be used to perform mechanical work by cyclically lifting a weight using an Au-Cd SMA. Further research revealed other materials demonstrating this phenomenon. In 1961, a group of U. S. Naval Ordnance Laboratory researchers lead by William Beuhler stumbled across a significant discovery in the field of SME and SMA [Buehler et. al. 1963]. While testing an alloy of Nickel and Titanium for heat and corrosion resistance, they found that it too exhibited the SM effect. The

material was later identified as Nitinol. Compared with other SMAs, Nitinol is easy and cheap to manufacture, resist corrosion and is safe to handle. These factors refreshed interest and research in the Shape Memory Effect and its applications [Toki Corporation, 1987; Grant, 1995].

Since the early days Nitinol components have been used in aerospace applications. On the other hand, in Japan, researchers looked into potential applications in domestic products. Nitinol based components have been present in the market since late 1960's. The early products tended to utilised Nitinol's thermal shape memory behaviour, used especially in aerospace applications. Nowadays, Nitinol components are used in many different ways including vibration control of buildings during earthquakes, stents for the coronary artery and robot components for outer space activities like Mars exploration[Barras & Myers,2000].

Shape memory alloys are typically available in the form of wires, sheets, ribbons, films and tubes. A large part of the research activities in SMAs involves the material in form of wire as it is easy to manufacture at low costs and relatively easy to model because of established one dimensional micro-macro theories of SMA.

The shape memory effect means that when an alloy is plastically deformed at low temperatures and is subsequently heated, it reverts to its original shape or dimension [Buehler & Wang 1968]. During this process, the material undergoes a structure phase change called the martensite-austenite transformation. When the alloy is cooled below the temperature Mf,

(martensite finish) the alloy is completely composed of martensite phase, which can be deformed easily. If distortion occurs at low temperature, the original shape can be recovered by heating the material above the austenite temperature Af (austenite finish). The heat transferred to the SMA drives a molecular rearrangement of the alloy during this phase transformation. The deformed martensite is now transformed to the cubic austenite phase, which is configured in the original shape of the SMA. A sketch of phase transformation is presented in Figure 2.1.
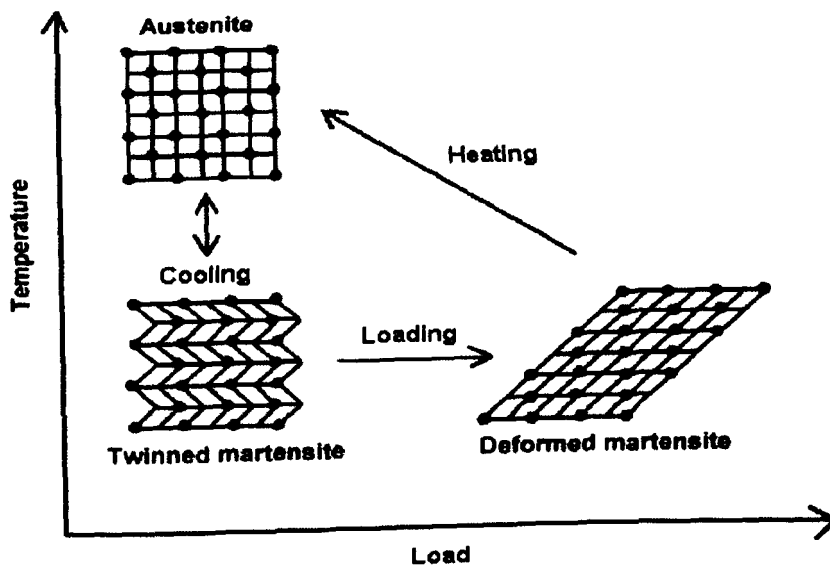
Figure 2.1 The phase transformation of SMA [Ryhanen,1999]

The addition of copper to the Nitinol was found to be effective in narrowing the stress hysteresis and in stabilizing the superelasticity characteristics against cyclic deformation, with the result that the slope of the load-deflection unloading curve of the alloy is lower than Nitinol. Moreover, it produced greater stability of both the transformation temperature and reduced the

ageing effect [Gil & Planell 1999]. In this work, the material used was Nickel Titanium Copper (NiTiCu).

2.2   Copper based SMA

The copper / aluminium binary alloy displays shape memory characteristics, with a transformation temperature generally considered too high for practical use. The addition of zinc to the system produces a new ternary system, CuZnAl, which is of commercial importance. These alloys have a useful transformation temperature that can be modified to lie between -100°C and 100°C.

Compared to other SMA's, CuZnAl SMAs have only modest shape memory properties, with a maximum recoverable strain of approximately 5%. Applications for CuZnAl alloys include fluid connectors and coupling, actuators, safety valves and other safety devices.

2.3   Magnetic shape memory alloys

Magnetic shape memory (MSM) alloys are a new type of material exhibiting magnetic field induced strains up to 10 %. As such they have potential for many technological applications. Also, the strong magneto-structural couplings of the MSM effect make the phenomenon very interesting from a scientific point of view. The alloys that exhibit MSM are NiMnGa and Ni_2MnGa alloy.

The magnetic moment is seen to originate mainly from Mn in the Mn-containing alloys and the existence of different structural phases is described to a band Jahn-Teller effect in the Ni band [Ayuela et.al 2002]. It refers to distortion of a highly symmetrical molecule, which reduces its symmetry and lowers its energy. In Ni_2MnGa the structural phase transformations are found to be driven by vibrational entropy at finite temperatures.

Analysis of the microscopic origins of the magnetic anisotropy shows that Ni gives the largest contribution to the magnetic anisotropy energy. Investigations of other structures show that in Ni_2MnGa the shortest crystal axis is always the easy axis of magnetization [Enkovaara et.al 2002]. From other magnetic properties, the Curie temperatures of Ni_2MnGa and Ni_2MnAl are estimated on the basis of total energy calculations of spin spirals. Ni is found to have an important effect also on the Curie temperatures despite its smaller magnetic moment when compared to Mn.

2.4 Current application of SMA

The majority of commercial and research-led applications make use of the thermal shape memory effect in an actuator in spacecraft, as well as in household applications. In medical applications, about 90% make use of the superelasticity, the remaining 10% use mainly the martensitic deformation characteristics. Examples of medical applications are tissue spreader, coronary probe, brain spatula and stents [Kulkarni & Bellamy,2001].

SMA also has been proposed for changing the area of nacelle nozzle for an aero engine [Rey et.al, 2001; Mitchell,2003]. The area of nozzle can be changed up to 20 percent, using a revolutionary lightweight SMA based actuator. This potentially improves efficiency and provides a measure of vectored thrust.

More recently, applications in Micro-Electro-Mechanical-Systems (MEMS) have led to the development of SMA in the form of a sputter-deposited thin film [Kahn et.al,1998]. The phase transformation in SMA thin film is accompanied by significant changes in the mechanical, physical, chemical, electrical and optical properties, such as yield stress, elastic modulus, hardness, damping, shape recovery, electrical resistivity, thermal conductivity, thermal expansion coefficient, surface roughness, vapour permeability and dielectric constant [Fu et.al.,2005]. These properties changes have led to the material to being used for microsensors and microactuators. The main advantages of SMA thin film include high power density, large displacement and actuation force, and low operation voltage. SMA films have been used to fabricate various MEMS devices such as micropumps, microvalves, micro-grippers, springs, microspacers, micro-positioners, and microrappers.

2.5 Shape memory alloy ribbon

Although a SMA wire can be considered as single degree of freedom component, SMA in the form of ribbon is categorised as a two degree of freedom system. The phenomenological models commonly used are based on equivalent one-dimensional applications. SMA models based on full 2D applications are still being developed. In certain applications, the use of a

SMA ribbon is necessary, for example in the manufacture of honeycomb core structures, which is the topic of this thesis.

Research on the application of SMA ribbons has been started by Jonnalagadda and co workers [Jonnalagadda et.al 1998, Jonnalagadda et.al 2000]. Their work consisted of embedding shape memory alloy (SMA) ribbons in epoxy resin to produce a SMA composite. A numerical simulation of the embedded ribbon was carried out using a fully coupled thermomechanical SMA constitutive model.

Fundamental research on SMA ribbons has only recently started. Recent work on the mechanical and thermomechanical properties of SMA ribbons has been performed by Liu [Liu 2003] and the pseudoelastic behaviour has been studied by Crone and co-workers [Crone et.al 2004]. Hee and Miyazaki [Hee & Miyazaki, 2004] have analysed the martensitic transformation behaviour in rapidly solidified alloys by using differential scanning calorimetry (DSC) and X-ray diffractometry (XRD) in melt spun ribbon.

2.6 Shape Memory Alloys damping characteristics

A high damping capacity is considered as one of the most important functional properties of shape memory alloys. Humbeeck and co-worker have done a work on SMA related to damping properties [Humbeeck 1996]. Damping is essentially related to the thermoelastic martensitic transformation. As a consequence of this transformation, the internal friction or damping can be

investigated for three different states. The first corresponds to a thermal cycling transformation, the second occurs during martensite induced strain cycling at constant temperature, while the third is related to the reorientation of martensitic state [Humbeeck 1996].

In the thermal cycling transformation, SMA provides the highest level of damping peak even though it is associated with low modulus. Under those conditions a highest level of loss factor will be observed during phase transformation. Therefore it is possible to use SMA for damping applications in this temperature range. However when the temperature is constant, the loss factor drops to a value closer to an average of the damping capacity of the two volume fractions of martensite and austenite. As a consequence, application of damping capacity in this temperature range and at constant temperatures becomes less attractive than for temperatures below Mf (martensite finish).

The second type of damping mechanism can be described as pseudoelastic damping [Gandhi & Chapuis, 2002], providing a high-energy dissipation due to the interaction between the martensite and austenite phases. These "pseudoelastic" properties are related to the formation of martensite from austenite, which has been induced by stress. Furthermore, these functional materials can operate at high stresses and thus have to withstand severe mechanical loadings [Predki et.al., 2004].

The third type of damping also offers high levels of energy dissipation due to movement and reorientation of martensite from twinned to detwinned state under an applied stress. This applied stress can be due to tension compression cyclic loading. Internal friction in thermoelastic martensitic alloys is generally attributed to the mobility of martensite-martensite interfaces. Martensite parent interfaces during the transformation give rise to a damping peak only if the heating or cooling is continuous. In this case the transformation itself is responsible for the damping.

2.7   Mechanics of Shape Memory Alloys

In this section the phase transformation will be explained briefly.

2.7.1 Transformation temperature

The phase stability of shape memory alloys is a function of both temperature and stress. The transformation temperature characterises the phase stability in the unstressed state. The transformation temperature is defined as the temperature at which a shape memory alloy changes from austenite to martensite or vice-versa. There are four different transformation temperatures in SMAs: martensite finish (Mf), martensite start (Ms), austenite start (As) and austenite finish (Af). The As and Af only been noticed when SMA being heated to above Af, while the Ms and Mf are only noticed when SMA is being cooled to below Mf temperature.

Several methods of determining these temperatures have been reported. The transformation temperatures of SMA are commonly measured by one of three

methods: differential scanning calorimeter (DSC), the electrical resistance method (ERM), which uses a sudden change in resistance as an indication of transformation and the applied loading method (ALM), where macroscopic displacement indicates the transformation. The DSC method is by far the most common method to determine the transformation temperature. Figure 2.2 shows how to determine the transformation temperature based on a DSC curve. For any particular alloy chemistry, the processing history and the stress conditions can change the transformation temperature.
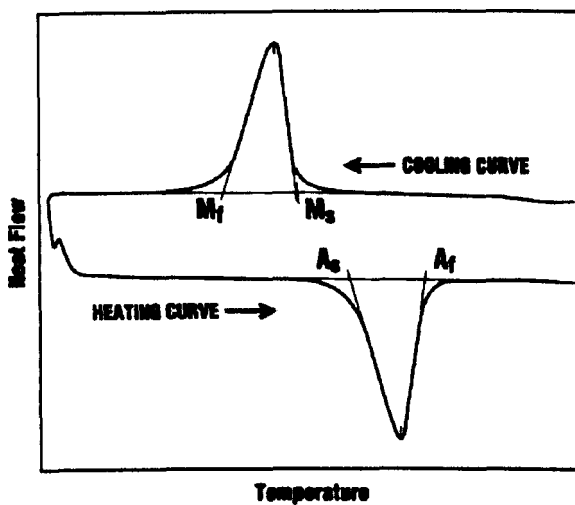
Figure 2.2 : A typical DSC curve for a NiTi shape memory alloy

2.7.2 Phase transformation

There are two principal mechanisms leading to phase transformation in SMAs: temperature change and mechanical loading. Upon heating, the martensite structure begins a reversible thermoelastic phase transformation to austenite when the temperature reaches the austenite start temperature (As). The transformation to austenite is completed when the temperature reaches

20

the austenite finish temperature (Af). Upon cooling, austenite begins to transform to martensite at a temperature equal to the martensite start temperature, and completes its transformation to martensite at a temperature equal to the martensite finish temperature.

Stress induced above the austenite finish (Af) temperature will result in phase transformation from austenite to detwinned martensite. A detwinned martensite phase can be obtained only by stress induced either in the austenite or martensite phases, while the twinned martensite phase only can be obtained at lower temperature, below the martensite finish temperature (Mf). These properties are associated with microscopic structure created due to material phase transformation. The phase transformation within this process is similar to the deformation process in plasticity. However, during SMA phase transformation, the yield stress strongly depends on environmental temperature. A schematic diagram of the crystallography of SMA structure is shown in Figure 2.3.
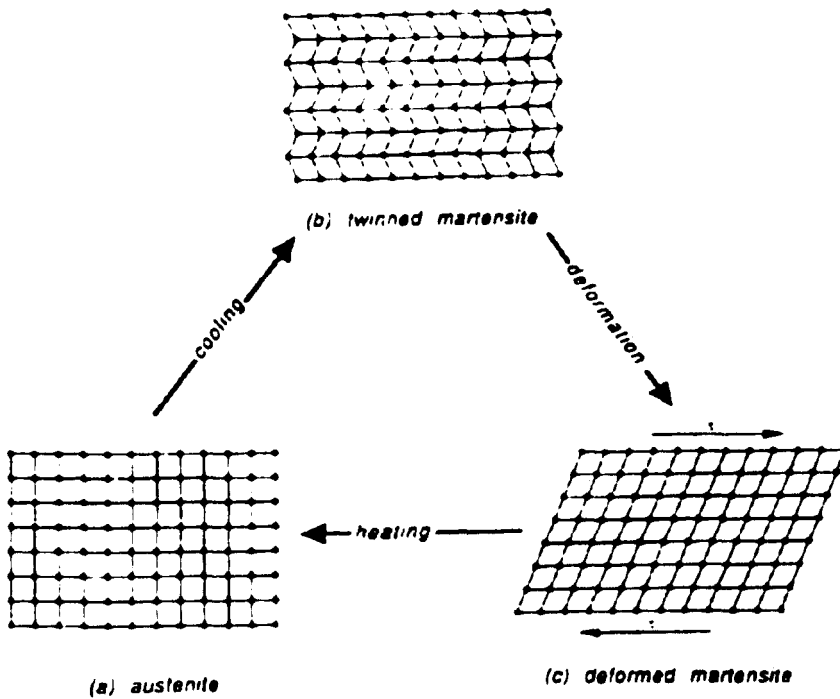
Figure 2.3 Crystallography of martensite-austenite phase
transformation [Wayman & Deurig 1990]

2.7.3 Shape memory effect

The shape memory effect is an important characteristic of SMA when designing actuators. When a SMA component is initially in the fully martensite phase, at temperatures between martensite finish and martensite start, stress induction leads to the so-called "forward phase transformation", i.e., transformation from the twin martensite phase into detwinned martensite one. During this process, we can obtain a large residual strain or plastic deformation, whose maximum value reaches up to 9% [Brinson,1992]. At this stage, upon heating above the austenite finish temperature, there occurs the removal of the transformation strain; called "reverse transformation". During the reverse transformation, large recovery forces of SMA can be obtained. In Nitinol, typical values of recovery stresses are between 500 MPa and 900

22

MPa. This cyclic process is called the shape memory effect (SME), sometimes also known as quasiplasticity [Bubner, 1996]

The shape memory effect of SMA is demonstrated by deforming the original shape of SMA, such as in form of spring, at below martensite start temperature. At that temperature, the material can be deformed to a second shape configuration while in the martensite state, but the macroscopic volume of the material has not changed. With small loads the specimen can be easily deformed, and the deformed shape remains after removing the loads. Upon heating to temperatures above the austenite transformation temperature, the material will return to its original shape configuration.

2.7.4 Pseudoelasticity

When a SMA component is at a certain temperature above Af, induced stress leads to a transformation from the austenite phase into the detwinned martensite. This effect is caused by the stress-induced formation of some martensite above its normal temperature. The application of stress beyond this critical stress results in a nonlinear stress-strain response due to the isothermal reversible transformation to martensite. Because it has been formed above its normal temperature, the martensite reverts immediately to undeformed austenite as soon as the stress is removed. This process provides a sort of "rubber like" elasticity in these alloys. This loading (forward transformation) and unloading (reverse transformation) process is known as pseudoelastic effect or superelastic.

Pseudoelasticity is also a behaviour of SMA components used widely in actuator applications. Conventional nitinol materials can typically recover principal strains of the order of up to 8%. The pseudoelastic behaviour of nitinol allows for the design of devices that exert a relatively constant stress over a wide range of strains or shapes. This unique behaviour has been used to design many implantable medical devices such as stents and stent grafts.

The difference between the pseudoelastic and shape memory effect is the environmental temperature: pseudoelastic only happen at temperature above Af, while shape memory effect or pseudoplastic is only happen in temperature below Mf. Most engineering applications using SMA take advantage of the above-mentioned two properties of SMA. The behaviour of the properties can be explained in Figure 2.4.
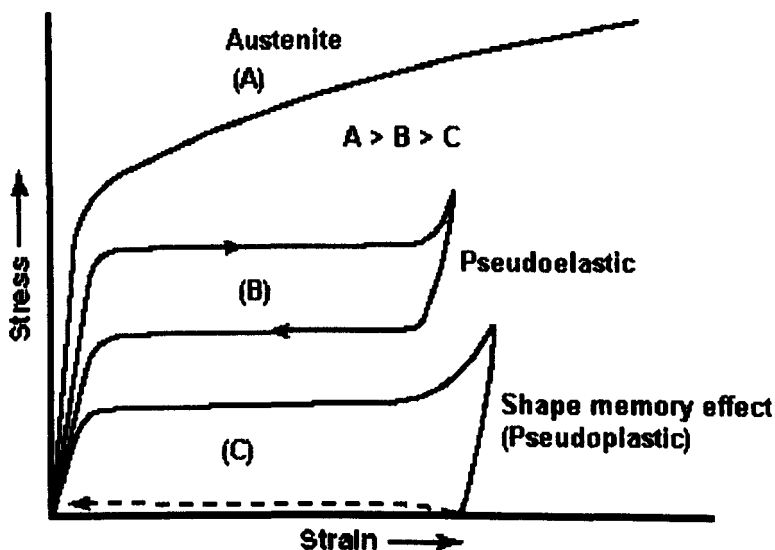
Figure 2.4   Typical stress-strain curves at different temperatures
[Hodgson,1988]

2.7.5 Hysteresis

Hysteresis represents the history dependence of physical systems when subjected to cyclic or time-dependent loading. If the component does not return to its initial position or strain condition it is exhibiting hysteresis, in some broad sense. Hysteresis, in its simplest formulation, is a loss of energy in a material during cyclic excitation [Gandhi & Wolons,1999]

In SMA, the temperature range for the martensite to austenite transformation, which takes place upon heating is somewhat higher than that for the reverse transformation upon cooling. The difference between the transition temperatures upon heating and cooling is a manifestation of the shape memory alloy hysteresis. Hysteresis in SMAs is defined as the difference between the temperatures at which the material is 50% transformed to austenite upon heating and 50% transformed to martensite upon cooling. This difference can be up to 20°C - 30°C [Abel et.al, 2004].

2.7.6 Two way shape memory alloys

Generally, SMA can have two shape memory phenomena, a one way shape memory effect (SME) and a two-way shape memory effect (TWSME). The basic difference between the one-way SME and the TWSME is that no reverse change of a shape occurs in the case of the one-way SME after subsequent cooling, whereas the TWSME is characterized by a shape change during the same cooling process. The TWSME exhibits switching between a "cold" shape and "hot" shape upon heating and cooling,

25

respectively. In the literature [Perkins & Hodgson, 1990], training procedures consisting of several heat treatments are required to develop the TWSME. In the processes, a stress field is introduced in the material. The resulting residual stress field assists the formation and growth of preferentially oriented martensite variants when the martensitic transformation proceeds in a specimen on cooling. Several different kinds of training procedures have been suggested. The repeated one-way SME process is one of those [Perkins & Hodgson 1990]. Better quality results are obtained if the specimen is constrained during heating to austenite finish temperature. Other methods include the repeated pseudoelastic process [Cingolani, 1999], and the repeated cycles of load-free heating followed by cooling under weak load [Perkins & Hodgson, 1990].

It has been recognised that the effectiveness of training procedures also depends on the applied heat treatment [Perkins & Hodgson 1990]. The disadvantage of the aforementioned methods is that a relatively complicated training device to hold the SMA has to be applied to perform any of them, in addition to the great amount of time and labour required. Some examples of potential applications include reversible fasteners, temperature-sensitive actuators, retrievable medical implants and toys and novelty items [Stalmans, 1999].

2.8 Constitutive Modelling of SMA

The use of SMAs in smart material applications depends on our ability to understand and describe the thermomechanical behaviour of SMA. Constitutive models are being developed for this purpose. Constitutive equations of SMAs are highly dependent on the temperature and the stress fields. Figure 2.5 illustrates the change of martensite structure as the load increases in a tensile test.
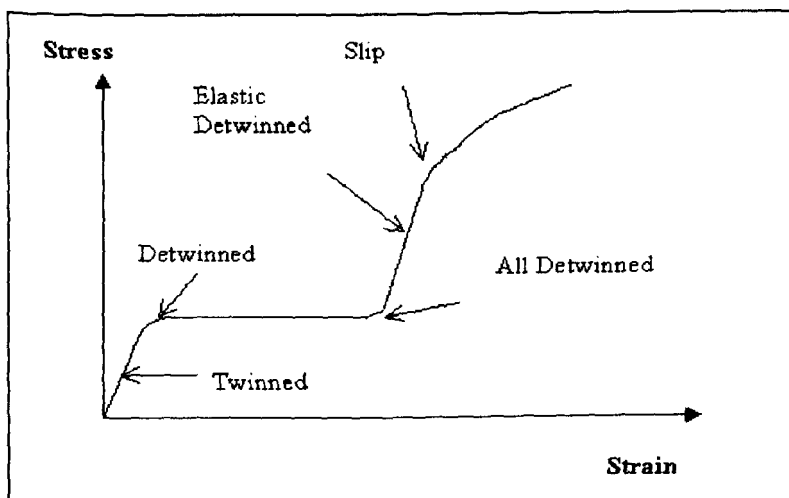
Figure 2.5 The state of martensite structure during tensile test

In general, the constitutive equations of SMAs can be divided into two main categories: the phenomenological ones and those based on micromechanics [Saadat et al, 2001]. The phenomenological approach has implemented various thermodynamic models and averaging schemes to explain the SMA constitutive behaviour resulting from martensitic transformation, while micromechanical models examine the effect of microstructural mechanisms on SMAs transformation behaviour. In these models, the mechanism of

orientation of martensite variants is then taken into account. These models have been discussed extensively by Nae et.al (2003).

Amongst the phenomenological models existing in open literature it is customary to mention the ones developed by Tanaka (1986), Mueller-Archenbach (1985), Liang-Roger (1990) and Brinson (1992). These models describe the mechanism of SMA in one dimension. As examples, we will discuss the Mueller-Achenbach model and the Tanaka Model including the modification done by Liang & Rogers and Brinson.

Mueller-Archenbach and Tanaka have used different approaches in deriving their theoretical frameworks. The Mueller-Archenbach model has made use of the non-convexity of the Helmholtz free energy function and its corresponding non-monotonic stress-strain curve to give the analytical description of phase transition and hysteresis of SMA [Mueller&Archenbach,1985]. The Tanaka model uses the energy balance and Clausius-Duhem principle to describe the hysteresis from phase transformation [Liang-Roger,1990].

The models from Liang & Roger [Liang&Roger,1990] and Brinson [Brinson,1992] were modifications of the Tanaka model, to provide a simplified formulation and, at the same time, more detail about the micromechanical evolution of SMAs. However, both Mueller and Tanaka models have been derived based on the original concept proposed by Falk [Falk,1983], who described the phase transformation stabilization based on

the Helmholtz free energy with the incorporation of Landau theory from physical statistics. The details about each model are described in Appendix B.

Some advanced models have been developed to simulate the application of SMA. Most of these models represent one dimensional structure related to SMA wires. Amongst the most used theoretical approaches present in the literature, one can cite the works of Boyd and Lagoudas (1996), Oberaigner et.al(1996) and Amalraj et.al (2000). Boyd & Lagoudas [Boyd & Lagoudas,1996] have proposed a phenomenological thermodynamic theory modelling an idealized SMA wire response. Oberaigner and co-workers [Oberaigner et.al, 1996] have established micromechanical a model consisting of a kinematic equation, a constitutive law, a heat conduction equation and a vibration equation to investigate a damping behaviour of a vibrating SMA rod. Amalraj and co-workers [Amalraj et.al., 2000] have modelled the temperature distribution in a shape memory alloy (SMA) wire with variable thermal and electrical properties. But this model is difficult to implement in a complex structure.

Chapter 3

LITERATURE REVIEW
- Honeycomb structures

In studying the deformation of honeycombs, research activities have focused on in-plane and out-of-plane mechanical properties. For the in-plane deformations, the various models developed involve combinations of bending and axial deformation of the ligaments for the hexagonal centresymmetric configuration, while cell collapse is identified as when the critical stresses in the cell ribs are reached. The out-of-plane deformation occurs when loading is acting on the transverse planes. This type of loading is acting perpendicular to the surface of sandwich structures. A comprehensive theory about both cases for hexagonal honeycomb has been described in the book by Gibson & Ashby [Gibson & Ashby, 1997]. This thesis is only concerned with the in-plane properties of the SMA honeycombs. Honeycombs with out-of-plane deformation mechanisms typical of sandwich panel applications will not be discussed.

3.1 In-plane properties of honeycomb

A significant amount of research activities have been carried out to examine the in-plane response of honeycomb materials in order to clarify the linear elastic properties and the collapse mechanisms that occur under static and dynamic loads. From a general point of view, the overall mechanical behaviour of a honeycomb under in-plane loading depends on the type of material from which the honeycomb core is made, its unit cell geometry, the deformation mechanisms of the single ribs composing the cell, and whether deformation occurs in tension or compression. The stress strain curves for general 2D honeycombs under in-plane loading are identified by three basic regions, a linear elastic portion, a plateau and a densification or fracture region, the latter in the case of tensile loading. Figures 3.1 and 3.2 show the typical behaviour of tensile and compression loading of hexagonal elastomer, elasto-plastic and brittle material honeycombs.

During tensile loading, two main stages of deformation can be identified. The first is related to elastic bending of the cell walls providing linear-elastic deformation. The second stage depends on the core material of the honeycomb. If the cellular solid is made from elastomeric material, the cell walls continue to rotate into the tensile direction and the stiffness rises because of densification. In the case of a plastic (or elasto-plastic) material, the plastic yielding of the hinges results in deformation at a constant stress in

31

the material, but because the walls of the cell are approaching each other, there is a gradual increase in density with a consequent stress rise. For the case of a brittle core material, the cell walls of the honeycomb will fracture.
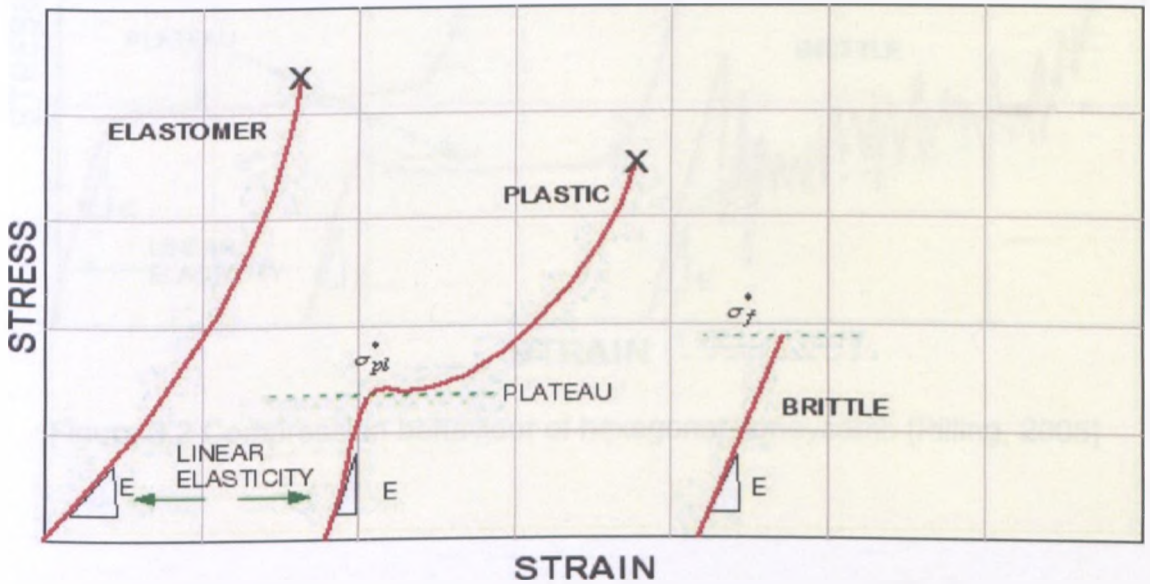
Figure 3.1 Tensile behaviour of hexagonal honeycomb [Pilling, 2005]

During compressive loading, three main stages of deformation will occur. In the first, the cell walls bend, where the flexure happens [Master & Evans, 1997]. The second stage is described by the reaching of the critical strain when the cell starts to collapse. During this stage the stress plateaus at the elastic buckling stress, giving rise to a series of brittle fracture events taking place in successive cell walls [Papka & Kyriakides, 1994]. The final stage is when the cell walls touch each other. At this stage, densification will take place and the stress will rise rapidly.
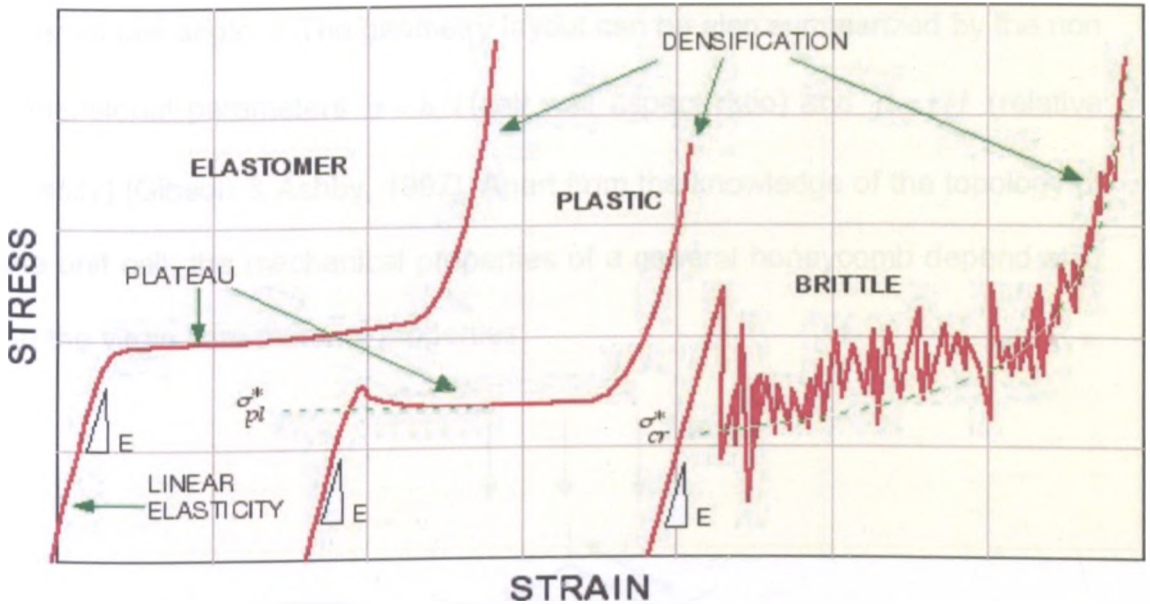
Figure 3.2 Compression behaviour of hexagonal honeycomb [Pilling, 2005]

3.2 Hexagonal honeycomb

The Cellular Material Theory (CMT) has been developed by Gibson and co-workers [Gibson et al, 1982] to describe the properties of centresymmetric honeycomb structures. According to the CMT, the cell walls are described as Euler-Bernoulli beams with bending deformation, to describe the in-plane linear elastic response of the honeycomb. An improved model considering also the axial deformation during uniaxial tensile in-plane loading has been proposed by the same authors [Gibson & Ashby, 1997].

Figure 3.3 shows the geometry layout of a typical hexagonal cell. General centresymmetric honeycomb unit cells can be characterised by cell walls of

length h and l, width b along the z direction (out-of-plane), thickness t and internal cell angle θ. The geometry layout can be also summarized by the non dimensional parameters $\alpha = h/l$ (cell wall aspect ratio) and $\beta = t/l$ (relative density) [Gibson & Ashby, 1997]. Apart from the knowledge of the topology of the unit cell, the mechanical properties of a general honeycomb depend also on the virgin core material properties.
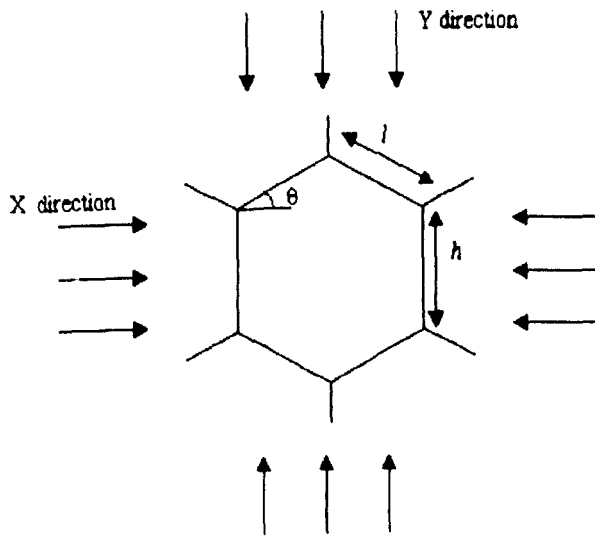
Figure 3.3 Hexagonal Honeycomb unit cell

Prior to the popular approach developed by Gibson and Ashby, El-Sayed et al. (1979) analysed the in-plane Young's modulus of honeycombs and the collapse stress when plastic hinges form at the ends of the single-thickness faces. Gibson et al. (1982) extended this analysis, and established clearly the moduli and collapse stresses of honeycombs. They confirmed El-Sayed et. al's result that the initial Young's modulus of a regular honeycomb E_H is isotropic in the plane, related to the wall thickness t to length l ratio, with equal thickness walls   by

$$E_H = \tfrac{4}{\sqrt{3}} E_c \beta^3 \qquad \qquad \text{...(3.1)}$$

where E_c is the Young's modulus of the core material considered as an isotropic medium. For low-density honeycombs having uniform wall thickness, where the volume of the vertices can be ignored, the ratio R between the honeycomb density and the core material is given by:

$$R = \tfrac{2}{\sqrt{3}} \beta \qquad \qquad \text{...(3.2)}$$

Following (3.1) and (3.2) the Young's modulus of a regular honeycomb ($\theta = 30°$, $\alpha = 1$) is related to the ratio R by:

$$E_H = 1.5 E_c R^3 \qquad \qquad \text{...(3.3)}$$

This result can be used as a check on the validity of low-strain, or small deformation computations. The predicted elastic collapse stress σ_{CE} of a regular honeycomb, with uniform thickness faces, is [Gibson & Ashby, 1997]

$$\sigma_{CE} = \tfrac{0.343^2 \pi^2}{3\sqrt{3}} E_c \beta^3 = 0.223 E_c \beta^3 \qquad \qquad \text{...(3.4)}$$

Gibson and Ashby (1997) divided the elastic buckling stress of Equation 3.4 by the Young's modulus of Equation 3.1 to estimate that buckling initiated at a strain of 10%. This assumes that the stress–strain curve remains linear to the point of buckling. In their analysis of plastic collapse for stresses in the x- or y-directions, it is assumed that the vertices do not rotate, and that the faces only bend around the plastic hinges. The predicted stress for collapse by yielding is, for both stress directions:

$$\sigma_{ys} = \tfrac{2}{3}\sigma_0 \beta^2 \qquad\qquad ...(3.5)$$

where σ_0 is the yield stress of the core material. Their analysis does not give the yield strain, or details of the stress–strain curve.

The models developed by El-Sayed et.al and Gibson and Ashby considered essentially the bending of the inclined rib of a centresymmetric hexagonal structure as the deformation mechanism inducing the overall in-plane mechanical elastic properties of the cellular material. In a seminal paper, Masters and Evans [Masters & Evans, 1996], also considered different mechanisms responsible for the mechanical performance of the honeycomb. In particular, they outlined that stretching, hinging and bending give different contributions based on the relative density β of the material. They found a significant correlation between bending deformation and low relative densities (i.e., lower than 5 %) for the in-plane mechanical properties. They also pointed out that stretching and hinging can be also derived by different material properties present at the base of the rib – a reality considering the commercial manufacturing process for hexagonal honeycombs.

In the 2nd edition of the book from Gibson and Ashby [Gibson & Ashby, 1997], an extension of the original model illustrated in the paper published in 1982 [Gibson & Ashby, 1982] including the axial and shear deformation of the honeycomb cell rib has been proposed. In their model, the axial stiffness of the rib is analogous to the stretching spring constant of [Masters & Evans, 1996], while the shear deformation (i.e., Timoshenko beam) can be equated to the hinging mechanism due to shear [Masters and Evans, 1996]. The

homogenised in-plane mechanical elastic properties result therefore as an explicit combination of the relative density β, the core material properties (including the Poisson's ratio of the core material for the rib shear deformation) and the shear correction factor depending on the cross-section of the cell rib. As pointed out, the expressions given by [Gibson and Ashby, 1997] are equivalent to the ones with concentrated spring constants [Masters and Evans, 1996]. However, they can be readily related to results coming from numerical simulations of honeycomb structures, where Timoshenko beam models with axial stiffness capabilities are used to model the single ribs of the cells [Scarpa et.al., 2000].

An alternative formulation to describe the second-order tensor of elasticity for centresymmetric honeycomb materials has been proposed by Lim [Lim, 2003]. The constants of the stress-strain tensor have been identified calculating the double derivative of the strain energy of a unit cell honeycomb (a quarter for symmetry reasons) versus the unit strain applied to calculate the same potential strain energy. Only the bending (or hinging) deformation mechanism have been considered, however.

Klintwood and Stronge (1988) assumed that the double-thickness cell faces with a layer of adhesive, of expanded honeycombs, were rigid and considered both elastic buckling and plastic collapse under plane stress loading. For uniaxial compression their equation, for the y-direction stress to initiate mode 2 buckling, reduces to:

$$\sigma_C = 0.346 \, \frac{\pi^2}{6\sqrt{3}} E_c \beta^3 = 0.328 \, E_c \beta^3 \qquad \ldots(3.6)$$

Papka and Kryriades (1994) presented an FEA analysis for the compression of an aluminium honeycomb with double-thickness vertical faces. When they assumed an elastic material for uniaxial compression, the elastic buckling strain was just over 15%, although they did not comment on the value. The boundary conditions were presumably periodic in both the x- and y-directions, to allow the alternating vertex rotation. In the same paper an elastic-plastic FEA analysis was also performed, in which the slope of the aluminium stress–strain curve fell by a factor of 100 once the yield strain of 0.423% was exceeded. With the variation of the aluminium yield strain from 0.3 to 1%, the 'limit stress' for the onset of plastic collapse increased almost linearly. For the 0.3% yield strain, the predicted yield stress was well in line with the value provided by Equation (3.5), while for the 1% yield strain the predicted stress was 90% of the value from the same equation. In their tensile tests on aluminium honeycombs, neighbouring vertices were observed to rotate in opposite directions, probably affecting the collapse stress variations. A high-strain deformation band also developed perpendicular to the stress axis, and propagating into the neighbouring layers of cells.

Hutzler and Weaire (1997) analysed the biaxial in-plane compression of honeycombs with uniform thickness faces. They imposed a strain in the Y-direction, then adjusted the X-axis strain to minimise the elastic energy of the honeycomb. They observed that a compressive strain of 8% would initiate the mode 2 elastic buckling pattern similar to the one presented in Figure 3.2. However, this energy approach could not be used to model uniaxial compression.

3.3   Auxetic materials

Negative Poisson's ratio materials expand transversely when stretched axially, and also undergo transverse contraction under axial compression. Materials with a negative Poisson's ratio [Lakes,1987;Caddock & Evans, 1989] have been called anti-rubber [Glieck,1987], dilational materials [Milton 1992], or auxetic materials [Evans et al, 1991]. The behaviour of auxetic material is exhibited in Figure 3.4. There is increasing interest in the development of these novel structural concepts, due to their counter-intuitive behaviour and also in applications where the auxetic property itself, or enhancements in other material properties due to a negative Poisson's ratio, may be exploited. For example, the development of auxetic nano materials is expected to lead to high modulus auxetic materials as well as having potential in sensor, molecular sieve and separation technologies [Grima et.al, 2000].
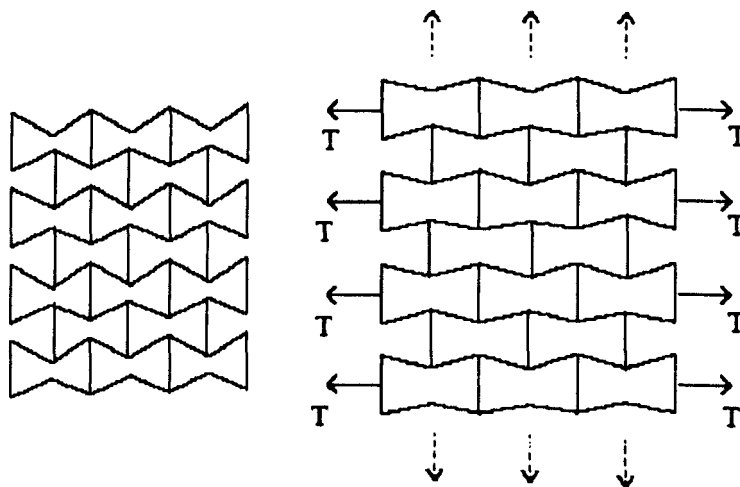
Figure 3.4   Auxetic in action

In the context of this work, we will consider only honeycomb structures made of centresymmetric (hexagonal) and non-centresymmetric (chiral) unit cells. For a broader introduction to auxetic materials and structures the reader is referred to the reviews of Alderson and Evans (2000) and Yang et al. (2004).

3.4   Auxetic centresymmetric honeycombs

Much interest has centred on the analysis of auxetic honeycomb made of unit cell hexagonal re-entrant structures, and their possible applications in classical sandwich structures. By centresymmetric one defines a unit cell with two perpendicular axies of symmetry. The honeycomb can therefore be produced by translation along the directions of the two axis of the original unit cell.

By taking a sheet of any "classical" material and bending it downwards, the top surface is inevitably slightly stretched. A normal material responds to this by attempting to shrink in the perpendicular direction, so the edges tend to curl upwards, producing a saddle-shaped surface. In auxetic materials, however, the response leads the edges to curve downwards, the same direction as the bending force as shown in Figure 3.5 [Evans & Alderson, 2000].

Anticlastic curvature
(non-auxetic)

Synclastic curvature
(auxetic)

(a)

(b)
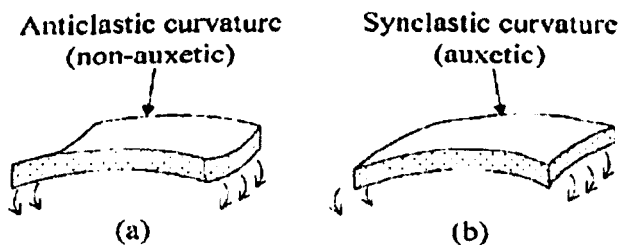
Figure 3.5 Out of plane bending a) Positif Poison's ratio plate b) Negative Poisson's ratio plate

This double curvature is just what is needed when it comes to moulding and shaping panels for car body parts or aircraft components, such as nose cones. These panels are often composites, consisting of two stiff skins of fibre-reinforced plastic with a layer of light, porous material sandwiched between them. To form a conventional composite panel into a dome-shaped double curve either requires machining or very high locus, which can cause damage. Auxetic honeycomb however will bend in both directions at once without weakening: the material bends over a double-convex surface, such as a dome, without any bonds breaking

The possibility of obtaining a honeycomb structure with in-plane negative Poisson's ratio behaviour has been highlighted by Gibson & Ashby (1982), with the development of their Cellular Materials Theory. The effective presence of an auxetic effect was recorded experimentally by Caddock et.al (1991), on aluminium and unstiffened cardboard honeycombs by measuring the curvature ratios with a optical system. As already pointed out, Masters and Evans [Master & Evans, 1996] modelled the deformation of hexagonal and auxetic honeycomb based on flexure, stretching and hinging deformation of the honeycomb cell walls. In the same period, Lee et.al (1996), performed a rigorous numerical homogenisation technique based on finite elements to calculate the coefficients of the stress-strain tensor of a re-entrant centresymmetric honeycomb for plane strain problems.

Scarpa and Tomlinson carried out an analysis related to the use of auxetic hexagonal honeycomb as the core structure of a sandwich panel undergoing

free vibration [Scarpa & Tomlinson, 2000]. In their work, it was suggested that the dynamic performance of a sandwich structure could be improved upon in terms of bending stiffness by using an auxetic honeycomb. Finite element simulations to calculate the in-plane Poisson's ratio and Young's moduli of auxetic honeycombs for different geometric layouts subjected to uniaxial loading have been presented by Scarpa and co workers [Scarpa et al. 2000]. When the honeycomb is loaded either in X- and Y-directions, the cell wall will bend. For linear elastic solids, the relationship of the four independent moduli can be described as,

$$E_x v_{yx} = E_y v_{xy} \qquad ...(3.7)$$

When considering axial and shear deformation effects, the in plane Poisson's ratio in X direction, v_{xy} can be computed as

$$v_{xy} = \frac{\cos^2 \theta}{(\alpha + \sin \theta)\sin \theta} \frac{1 + (1.4 + 1.5 v_c)\beta^2}{\left[1 + (2.4 + 1.5 v_c + \cot^2 \theta)\beta^2\right]} \qquad ...(3.8)$$

While in Y direction, v_{yx} can be computed as

$$v_{yx} = \frac{\sin \theta (\alpha + \sin \theta)}{\cos^2 \theta} \frac{1 + (1.4 + 1.5 v_c)\beta^2}{\left[1 + \left(2.4 + 1.5 v_c + \tan^2 \theta + \dfrac{2\alpha}{\cos^2 \theta}\right)\beta^2\right]} \qquad ...(3.9)$$

Where, v_c is the Poisson's ratio of the core material. A negative internal cell angle implies a re-entrant unit cell layout as shown in Figure 3.6. From Equation 3.8 and 3.9, it is clear that the negative Poisson effect in X direction is captured by the presence of a sine term in the denominator and in Y direction by the presence of cosine term. The experimental work for validation had been performed using an auxetic honeycomb made from aramid paper.

The study on the wave propagation of a sandwich plate and a sandwich beam with an auxetic core had been done by Ruzzene and co workers [Ruzzene et.al 2002; Ruzzene et.al, 2003]. The wave propagation analysis using Bloch Wave reduced finite element models demonstrated the possibility of using auxetic re-entrant configurations to tune the acoustic signature of a honeycomb material, by narrowing along specific directions the envelope of the flexural waves.

The dielectric properties within the J-band of a re-entrant honeycomb made of cast epoxy resin in laser stereolithography have been measured and simulated with a finite difference time domain technique by Smith et al. (2000). A combined analysis of the out-of-plane mechanical and electromagnetic properties of auxetic re-entrant using implicit and explicit finite element simulations for the flat wise compressive loading honeycombs has been presented by Scarpa and co workers [Scarpa et al., 2003]. Smith and Scarpa (2004) also developed closed-form solutions for the in-plane and out-of-plane complex dielectric properties using Hashin- Shtrikman bounds.

Using a finite element approach developed in-house, Whitty et al. (2003) could establish that conventional honeycomb cores could sustain less internal damage for the same mechanical loading, but re-entrant hexagonal configurations showed enhanced performance under thermal loading conditions.

A more recent development in the analysis of the in-plane properties of re-entrant hexagonal honeycombs is the study of the strain dependence of the Poisson's ratio under large nonlinear geometric loading by Wan et.al, (2004). In their study, the authors could determine closed-form solutions for the Poisson's ratio behaviour versus the large strain loading based on incomplete elliptical integrals of the first and second kind. The auxetic honeycomb configurations showed a tendency of reducing the magnitude of Poisson's ratio values when loaded along the direction X_2 of the cell defined by [Gibson & Ashby, 1982] for increasing strains along that direction.
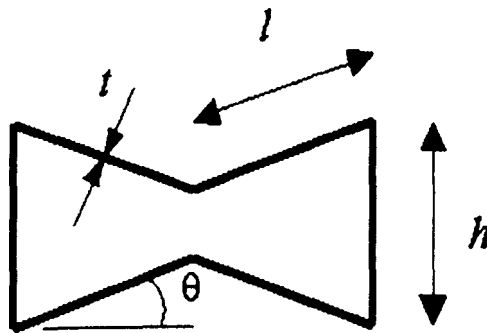
Figure 3.6   Re-entrant honeycomb unit cell

Between the centresymmetric auxetic structures, special mention should be made about the cellular solids designed using topology shape optimisation by Larsen et al. (1997) and Sigmund and Torquato (1996). However, the geometries involved in these specific structures show a significant departure from the centresymmetric hexagonal one which is one of the subjects of this work, and will not be considered further.

3.5 Non-centresymmetric (chiral) honeycomb

Another structure showing auxetic in-plane properties is the chiral honeycomb. Chiral topologies have been presented as a source of auxetic behaviour in 2D lattice models of hexagonal molecules at high density [Wojciechowski, 1989]. The first study of a structural chiral honeycomb has been reported by Prall and Lakes [Prall & Lakes, 1996]. A unit cell of chiral honeycomb is shown in Figure 3.7. The chiral hexagonal cell is composed of circular elements or nodes of equal radius r joined by straight ligaments or ribs of equal length L. The ligaments are constrained to be tangential to the nodes, with an angle between adjacent ligaments equal to sixty degrees. The honeycomb simultaneously possesses both hexagonal symmetry and a two-dimensional chiral symmetry. Structures exhibiting hexagonal symmetry are mechanically isotropic in-plane [Prall & Lakes, 1996]. The authors also provided experimental indications that the in-plane Poisson's ratio tends to minus unity even for large in-plane deformation (~ 20 % tensile strain).

The out-of-plane buckling properties of chiral hexagonal honeycomb assemblies have been analysed using a finite element approach with eigenvalue buckling by Spadoni et al. (2005). In their work the authors showed that local and global buckling of chiral honeycombs could outweigh the compressive strength in analogous iso-density centresymmetric honeycomb structures.

Recently, Lew and co workers have studied the vibroacoustic behaviour of chiral honeycomb for sandwich structures [Lew et.al, 2005]. They showed that the chiral hexagonal structure can enhance shear stiffness and compressive strength compared to classical cellular cores in sandwich components for structural and vibroacoustic applications.
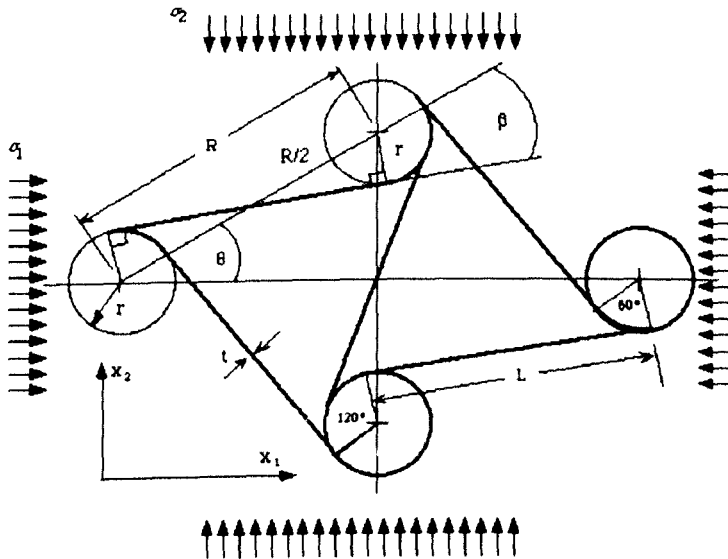
Figure 3.7 Chiral honeycomb unit cell

In experimental work to determine the Poisson's ratio of a chiral honeycomb [Prall& Lakes,1997], the chiral structure was manufactured from a wooden jig to position the circular nodes, the latter made from polystyrene. The chiral honeycomb structure was then placed on top of a high-quality photocopier machine and uniformly loaded along perpendicular directions. The displacements values in both directions were recorded xerographically from the motion of targets placed on the model. Thereafter, the measurements of displacements were used to calculate the Poisson's ratio value.

In the experiment, the authors identified the value of the Poisson's ratio to be consistent with the theoretical one of -1. The experimental results for Poisson's ratio vs. strain measured in the work of Prall and Lakes are shown in Figure 3.8. It is apparent from the figure that as the strain increases; the measurement errors decrease and the value tends to move consistently towards -1. The constancy of the Poisson's ratio in the Chiral Honeycomb structure is due to the ability of the cells or ligament to "wind" in upon themselves during compression [Prall & Lakes, 1996].
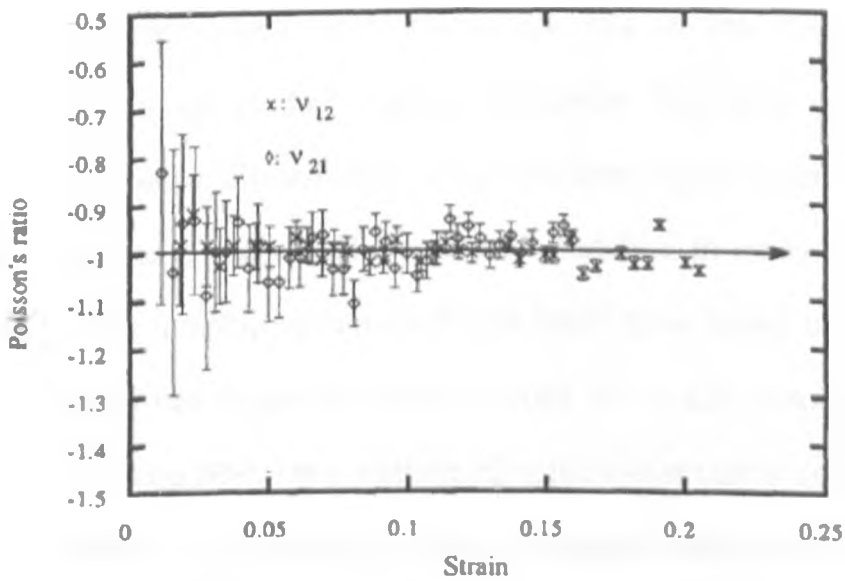
Figure 3.8 Experimental Poisson's ratio vs strain for chiral honeycomb
[Prall & Lakes, 1996]

Chapter 4

MODELLING

4.1 Finite Element Modelling

Numerical simulation plays an indispensable role in the manufacturing process, speeding up product design time while improving quality and performance. Recently, analysts and designers have begun to use numerical simulation alone as an acceptable means of validation. In many disciplines, virtual prototyping (employing numerical simulation tools based on the finite element methods) has replaced traditional build and break prototyping. The finite element method (FEM) is a mathematical technique that is used to solve physical problems in engineering analysis and design. It involves solution for partial differential equations (PDE) as well as of integral equations. The solution approach is based either on eliminating the differential equation completely or rendering the PDE into an equivalent ordinary differential equation. The method requires the discretisation of the domain into subregions or cells. The method is applicable to a wide range of physical and engineering problems, provided it can be expressed as a PDE.

4.2 Modelling SMA honeycomb behaviour in ANSYS

ANSYS is a general purpose finite element modelling package for numerically solving a wide variety of mechanical problems. It is a computer based finite element analysis to solve the underlying governing equations and tne associated problem with specific boundary conditions.

It must be pointed out that recent ANSYS versions [ANSYS 7.1 User's Manual, 2004], are able to model temperature dependent and pseudoelastic SMA materials using the approach outlined by Auricchio and Sacco [Auricchio & Sacco, 1997]. The elements with this capability are solid (2D or 3D) and therefore involve the creation of very large meshes for a single honeycomb cell. If one wants to represent the uniaxial tensile in-plane properties of a honeycomb, it becomes necessary to develop models with many thousands of degrees of freedom, therefore involving very significant computation effort [Scarpa et al, 2000]. Because the principal deformation mechanisms in the honeycomb ribs are in-plane bending and tension-compression, beam elements should provide a more efficient mesh. There is however, no beam element with embedded SMA characteristic in ANSYS.

The aim of FE modelling was to be able to represent the response of SMA honeycomb to applied loading. A critical part of these activities was the selection of suitable element and material behaviour that could simulate accurately and efficiently, the load/deformation behaviour of a honeycomb with the complex stress-strain characteristics seen in the martensite region.

Models based on beam elements also provided a comparison with the results from the Cellular Material Theory (CMT) [Gibson & Ashby, 1997], approximating the SMA behaviour in full martensite or austenite region using equivalent elasto-plastic models.

Within the context of this work, in the martensite region, BEAM3 has been chosen for the elastic element of SMA for the CMT approach while BEAM23 element has been selected to model the nonlinear elastic element of SMA. A special material model option has been selected with suitable numerical values to represent the pseudoplastic behaviour of shape memory alloys in the martensite phase. The type of modelling has been applied as shown in Figure 4.1.
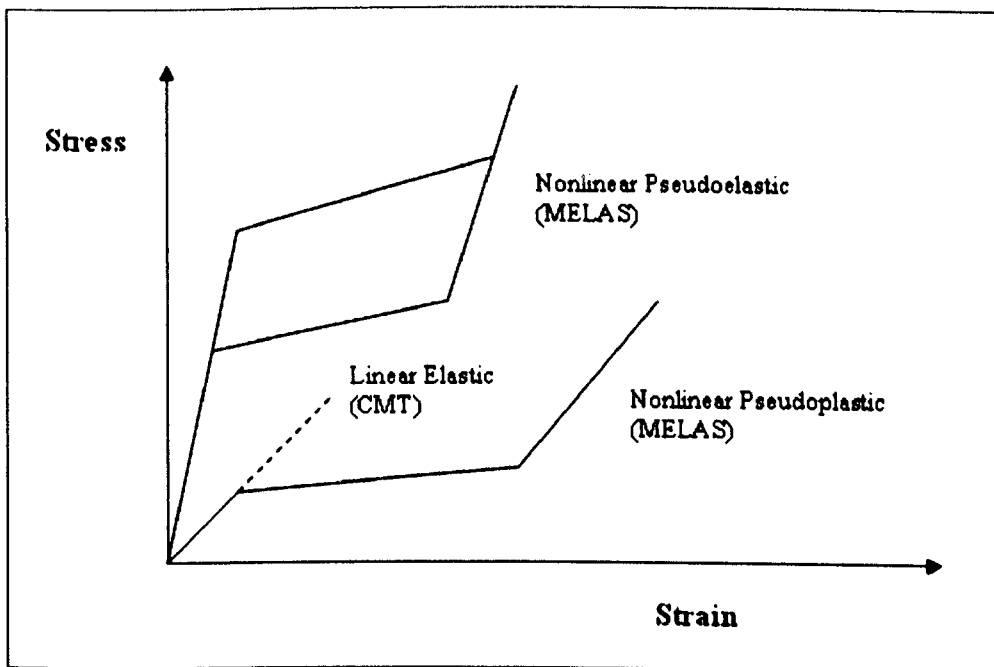
Figure 4.1 Type of modelling of SMA

In modelling chiral honeycomb in the austenite region, the approach outlined by Auricchio and Sacco [Auricchio & Sacco, 1997] has been used. In this work, this approach was able to model SMA for pseudoelastic behaviour. Plane 183 elements have been selected in this work.

4.2.1 BEAM3 2-D elastic beam
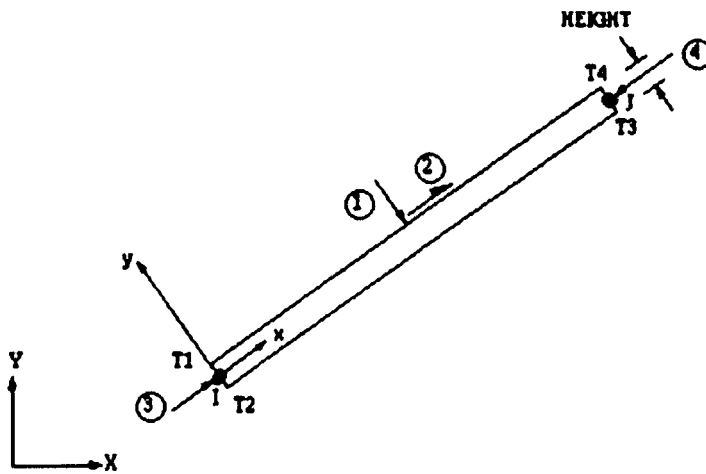
Figure 4.2 BEAM3 2-D

As shown in Figure 4.2 and 4.3, BEAM3 is an elastic element with tension, compression, and bending capabilities. The element has three degrees of freedom at each node: translations in the nodal x and y directions and rotation about the nodal z-axis. The element is defined by two nodes, the cross-sectional area, the area moment of inertia, the height, and the material properties.
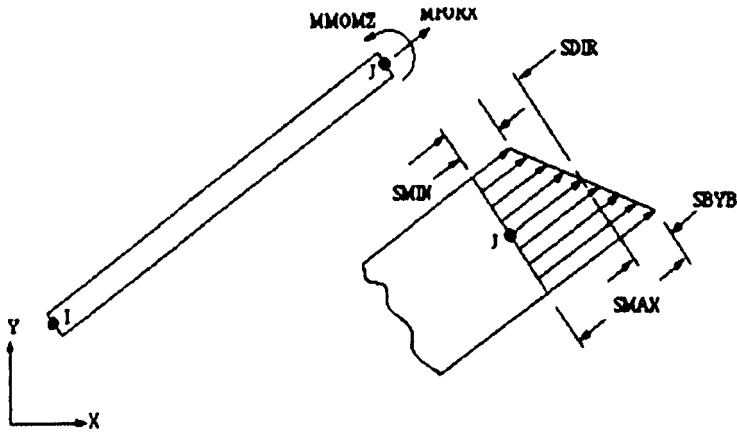
Figure 4.3 BEAM3 Stress Output

The beam element can have any cross-sectional shape for which the moment of inertia can be computed. However, the stresses are determined as if the distance from the neutral axis to the extreme fibre is one-half of the height. The element height is used only in the bending and thermal stress calculations. The applied thermal gradient is assumed linear across the height and along the length. The beam element must lie in an X-Y plane and must not have a zero length or area. The moment of inertia may be zero if large deflections are not used.

4.2.2 BEAM23 2-D plastic beam

As in Figure 4.4, BEAM23 is similar to BEAM3 except that, it calculates stress through its thickness more accurately and it allows plastic, creep and swelling.
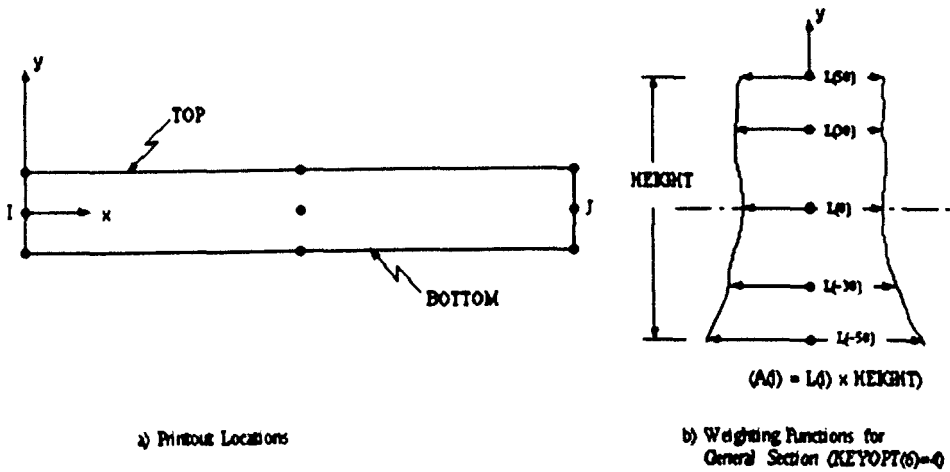
Figure 4.4   BEAM23 Characteristics

4.2.3   PLANE 183 2-D 8-Node Structural Solid

PLANE183 is a quadratic two-dimensional, eight-node element that can be used with irregular meshes. Its topology is shown in Figure 4.5.
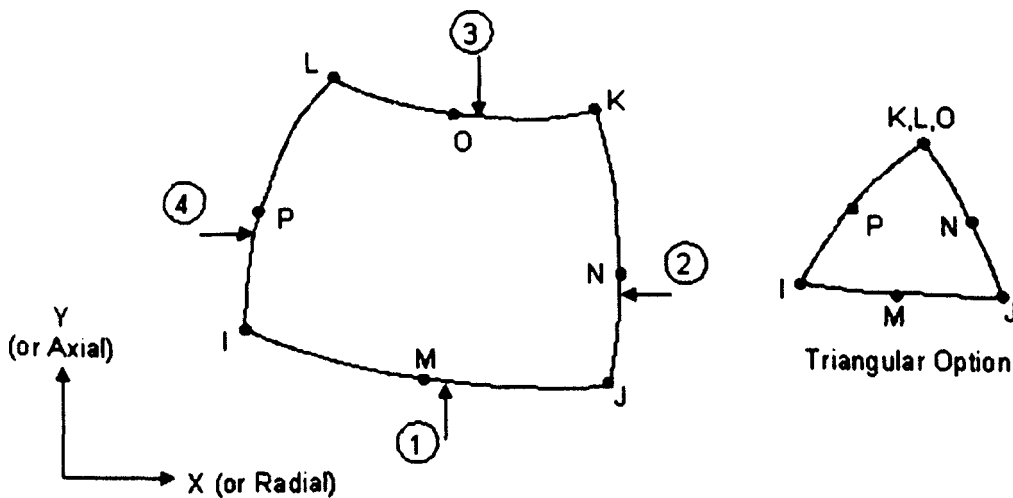
Figure 4.5   PLANE183 in ANSYS

This element is defined by eight nodes having two degrees of freedom at each node, translations in the nodal x and y directions. This element has plasticity, hyperelasticity, creep, stress stiffening, large deflection, and large strain capabilities. It also has mixed formulation capability for simulating deformations of nearly incompressible elastoplastic materials, and fully incompressible hyperelastic materials.

4.3   Modelling of SMA ribbon

Shape memory alloy wire has been used for engineering applications for a long time. A wire can be considered as a one-dimensional structure. Some one dimensional FEM models have been discussed in Chapter 2.

A SMA ribbon can be considered as a two dimensional structure. As mentioned before, an established micro-macro model for 2D SMA has not been fully developed, although some attempts have been made recently [Qidwai & Lagoudas, 2000], with special emphasis on the thermo-mechanical properties.

In this work the behaviour of the SMA ribbon in the fully martensitic state has been modelled using BEAM23 elements within the ANSYS code. The material properties have been entered as tabled data using the command TB-MELAS, from the experimental stress-strain curve obtained on a single ribbon under uniaxial tensile test at 25°C, where "MELAS" indicates a Multi-linear Elastic Material.

A single FE beam model representing the ribbon under uniaxial tensile loading was initially validated with the experimental results. This operation was necessary to assess the feasibility of the beam elements to represent correctly the single ribs of the honeycomb structures. The uniaxial tensile simulations were carried out by applying a concentrated tensile force on a 10-element FE model of the ribbon with fully clamped conditions at one end. The load was applied in 100 substeps, and the solution achieved using a Newton-Raphson algorithm with line-search method and constant stepping. At the end of each loading condition, the resultant deformation of the ribbon was calculated and the engineering strain obtained.

The objective of this step was to justify whether the TB-MELAS command is able to model stress-strain behaviour of the martensite phase of shape memory alloys in ANSYS. Satisfactory comparison between the FE and experimental results would allow implementation of nonlinear FE rib into the construction of the overall models for the uniaxial tensile properties.

4.4   Shape Memory Alloy Honeycomb

For a preliminary study of shape memory alloy honeycombs, it is important to understand the effect of changing cell angle during uniaxial loading on the elastic modulus of SMA honeycomb. Since SMA pnysically has elastic and plastic properties, therefore elasto-plastic collapse stress of SMA honeycomb must be defined first. Calculations were made according to Cellular Material

Theory [Gibson and Ashby, 1997]. When subject to loading in the X direction for elastic modulus, $E^{*}{}_{X}$ and elasto-plastic stress, $(\sigma^{*}{}_{pl})_{X}$ and in the Y direction for elastic modulus, $E^{*}{}_{Y}$ and elasto-plastic stress, $(\sigma^{*}{}_{pl})_{Y}$, the equations can be simplified as below,

In the X direction,

$$E^{*}{}_{X} = E_{s}\left(\frac{t}{l}\right)^{3}\frac{\cos\theta}{\left(\frac{h}{l}+\sin\theta\right)\sin^{2}\theta}\frac{1}{1+(2.4+1.5v_{s}+\cot^{2}\theta)(t/l)^{2}} \qquad ...(4.1)$$

$$\frac{\left(\sigma^{*}{}_{pl}\right)_{X}}{\sigma_{ys}} = \left(\frac{t}{l}\right)^{2}\frac{1}{2(h/l+\sin\theta)\sin\theta} \qquad ...(4.2)$$

In the Y direction,

$$E^{*}{}_{Y} = E_{s}\left(\frac{t}{l}\right)^{3}\frac{\left(\frac{h}{l}+\sin\theta\right)}{\cos^{3}\theta}\frac{1}{\left(1+(2.4+1.5v_{s}+\tan^{2}\theta+\left(\frac{2(h/l)}{\cos^{2}\theta}\right))(t/l)^{2}\right)} \qquad ..(4.3)$$

$$\frac{\left(\sigma^{*}{}_{pl}\right)_{Y}}{\sigma_{ys}} = \left(\frac{t}{l}\right)^{2}\frac{1}{2\cos^{2}\theta} \qquad ...(4.4)$$

where, E_{s} is Young's Modulus and v_{s} is Poisson's ratio for the SMA and σ_{ys} is yield stress for honeycomb material.

4.5 Finite Element Analysis of Hexagonal and Re-entrant Honeycomb Structure

The modelling of the SMA honeycomb structure consists of two parts. The first part was related to the simulation of the linear elastic tensile properties

which related to the CMT approach, while the second was concerned with the non linear tensile loading or pseudoplastic behaviour. The first part is very important to identify the Young's modulus of the honeycomb along the loading direction.

4.5.1 Uniaxial elastic tensile loading FE models

The Cellular Material Theory [Gibson & Ashby,1997] formulae have been benchmarked against finite element models developed using the commercial code ANSYS [Scarpa et.al, 2000]. The formula allowed representing the Young's modulus along the uniaxial loading direction. In order to simulate the pure uniaxial tensile test for an equivalent large honeycomb sample, the models were developed using 2340 BEAM3 beam element.

The honeycomb models were loaded with a uniform displacement along the loading direction at one end, and constrained in the normal direction at the opposite end. The constrained nodes (both clamped and loaded) were restrained from in-plane rotations for local stiffening [Silva et al, 1995]. This combination of boundary conditions corresponds to a guided roller model. The equivalent uniaxial stress was computed by averaging the reaction force of the sample over the length of the loaded side. The homogenised Young's modulus was therefore calculated as the ratio between the equivalent stress and the strain applied on the honeycomb model.

To take into account the effect on the mechanical properties of smaller honeycomb samples or clamped conditions that could occur during testing, models with fully clamped conditions at one end and with reduced cell numbers have also been prepared.

4.5.2 Uniaxial nonlinear tensile loading FE models

A similar approach to the single SMA ribbon was taken to simulate the uniaxial nonlinear tensile loading of the SMA honeycomb samples. The models were prepared using the validated beam elements to represent the single ribs of the cellular structures. Each model consisted of an average of 570 elements, with 10 elements per rib. Particular care had been paid to represent the effective boundary conditions of the honeycombs. The bottom end of honeycomb was fully clamped in the X and Y directions and also in rotations. The other end was allowed to have a displacement in the Y direction and was clamped in X direction and no rotations. Figure 4.6 shows the model of the honeycomb in ANSYS during testing in the Y direction. A similar model has been used with the auxetic honeycomb.
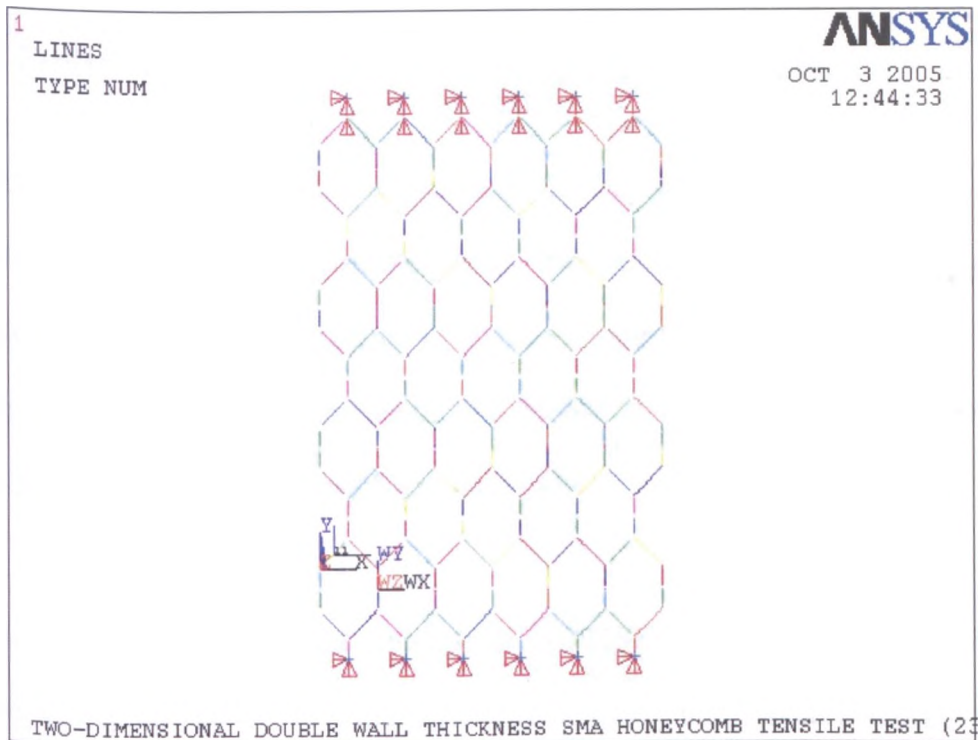
Figure 4.6 Finite element of SMA honeycomb for testing

Shape Memory alloys show nonlinear stress-strain behaviour. The non-linearity comes from the elastic plastic behaviour of SMA itself. The nonlinear simulation was carried out using similar solution options used to validate the single ribbon model, with only the substeps reduced to 50 to decrease the CPU time required. The calculation of the equivalent stress-strain curves was similar to the one performed for the single ribbon model. Equal nodal forces were applied to one edge of the honeycomb sample. The sum of the applied forces was averaged over the length of the loading segment to obtain the equivalent tensile stress. After solution of the related nonlinear static problem, the average displacement of the loaded segment was computed and the equivalent strain calculated.

4.6 Finite Element of Chiral Honeycomb Unit Cell

A compression test was carried out using a unit cell of the chiral honeycomb structure. A unit cell is described as the smallest, repeatable, oriented structural unit, which is capable of representing a whole periodic chiral honeycomb structure. In the work, the model of unit cell was based on the work by Prall and Lakes [Prall & Lakes, 1996].

A model of the unit cell was developed in ANSYS as a 2D object, which is shown in Figure 4.7. It has been developed using the TB-MELAS option for SMA as recommended by recent ANSYS version [ANSYS 7.1 User's Manual, 2004] to model the shape memory alloys element. The reasons for making it two dimensional were for ease of modelling and certainly to reduce the computational time. The model was designed using PLANE183 elements in ANSYS as shown in Figure 4.5. The choice of the element type was based upon the requirement given by ANSYS that shape memory alloys are only able to be modelled using 5 element types, which are Plane182, Plane183, Solid185, Solid186 and Solid187. Plane182 and Plane 183 are used for 2D modelling of solid structures while Solid185, Solid186 and Solid187 are for 3D modelling.

Two different materials were defined for the unit cell. One was shape memory alloy for the ligaments and the second was steel for the nodes. Steel was chosen to be the material for the nodes as it is stronger and stiffer therefore minimising deformation of the nodes under loading.
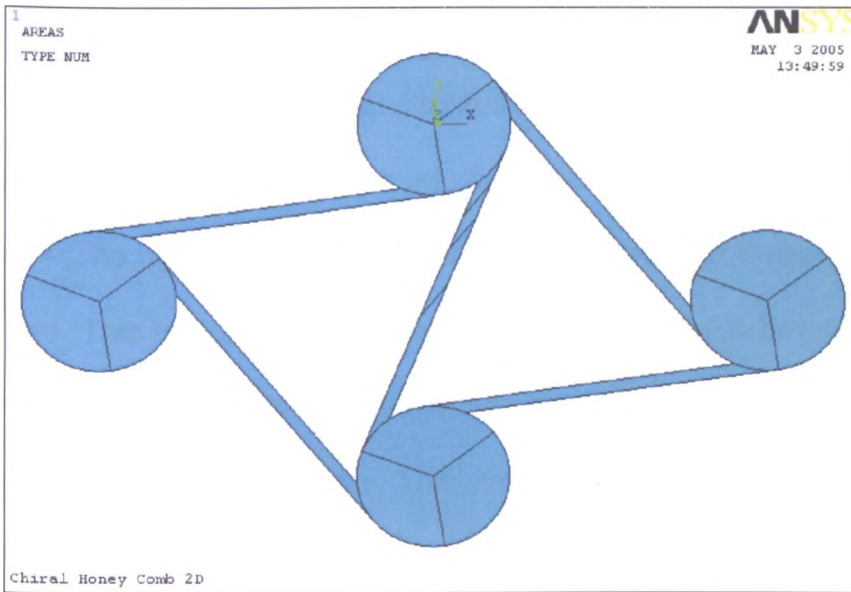
Figure 4.7 Unit cell modelling of the Chiral Honeycomb structure

Figure 4.8 shows the element mesh of the structure, which depicts a uniform and well coordinated meshing of the object. This unit cell of the chiral honeycomb structure is used to investigate the behaviour of the structure under uniaxial tensile loading, and observe the significant effect of having the shape memory alloy as the ligament.
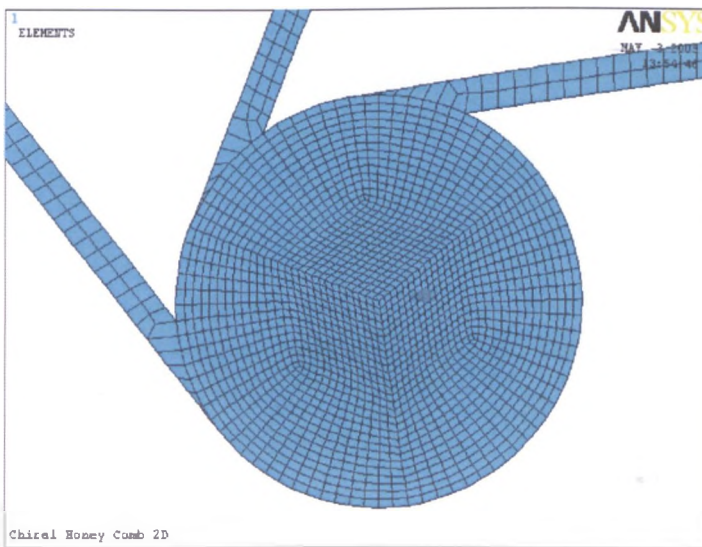
Figure 4.8 Element meshing of the unit cell

The unit cell of a chiral honeycomb structure is shown in Figure 4.7 has a R/r ratio of 5, which was similar to the geometry of Lakes's experiment [Prall & Lakes,1997]. The unit cell is used to study the behaviour of Poisson's ratio for the structure. This is done by applying a compressive force in both X and Y directions to the structure, and subsequently measure the displacement value for calculating the Poisson's ratio. This analysis was carried out to confirm whether the unit cell (with the shape memory alloy as the ligament) conforms to the theoretical value of -1 for the Poisson's ratio. Results for the analysis of the unit cell will be discussed in Chapter 6. The ANSYS code for the entire test carried out is presented in the Appendix C.

Chapter 5

SMA RIBBON TESTING AND RESULTS

5.1   Description of the ribbon

In this work, SMA ribbon has been used to manufacture the honeycomb. The ribbon was produced by @Medical Technologies n.v. with dimension of 0.27 mm thick and 4.67 mm wide. The product specification of the same material for the ribbon is given in Appendix E. The chemical composition is 48% Ni, 46% Ti and 6% Cu. The actual data for transformation temperature and mechanical characteristics have not been given by the manufacturer. Therefore, characterisation was done in laboratory. The data will change with the manufacturing process and heat treatment that has been experienced by the material. This ribbon was used because it was the only ribbon available at the time with a ratio of thickness to width less than 1:10.   Thin ribbon is advantageous for honeycomb manufacture, as it is flexible.

5.2 Differential Scanning Calorimeter (DSC) Test

The phase transformation behaviour of the SMA ribbon was determined using a high resolution modulated Perkin Elmer Pyris 1 Differential Scanning Calorimeter (DSC)- see Figure 5.1. A DSC device measures the amount of energy (heat) absorbed or released by a sample when subjected to thermal loading (heating or cooling), or held at a constant temperature.
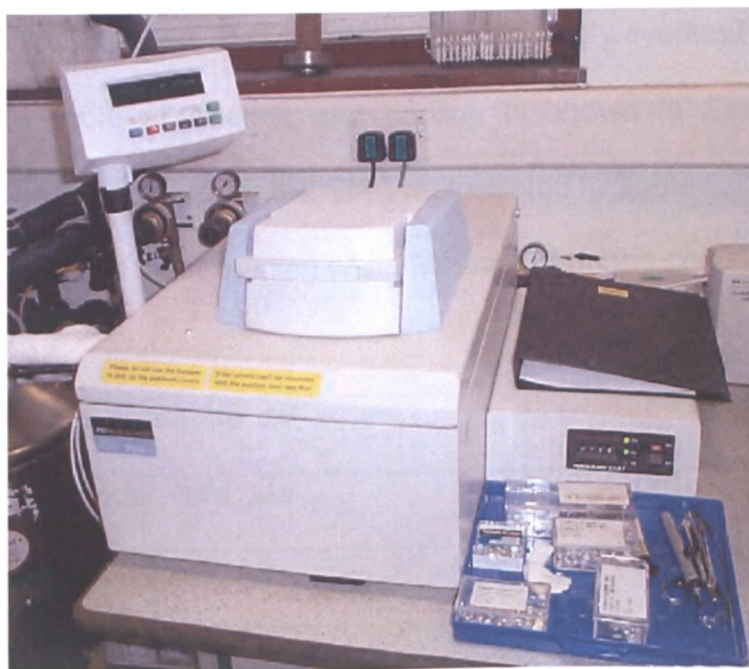
Figure 5.1   Perkin Elmer Pyris 1 Differential Scanning Calorimeter

Typical applications include determination of the melting point temperature and the heat of melting; measurement of the glass transition temperature; curing and crystallization studies; and identification of phase transformations. The temperature range of the DSC Pyris-1 is -170°C to 730°C. The temperature accuracy is 0.1°C, sensitivity , 1 mW and maximum scan rate is 100°C/min

The samples used for the DSC measurements contained approximately 7 mg of SMA ribbon. The temperature and energy flow were calibrated using an indium reference standard, while the specimens were placed in an aluminium pan with helium gas flowing through the chamber. A reference pan was used to host a sample of the matrix, having similar weight to the matrix fraction of the tested specimen. All specimens were heated to 150°C at a rate of 10°C/min. The specimens were then cooled to 0°C, reheated to 150°C and cooled again to 0°C. The cooling/heating rate was always kept at 10°C/min. The complete cycle of heating and cooling is shown in Figure 5.2. The transformation temperature for the SMA is illustrated in Table 5.1. The As and Af were determined during heating while Ms and Mf during cooling.

Martensite finish temperature, Mf	38° C
Martensite start temperature, Ms	50° C
Austenite start temperature, As	58° C
Austenite finish temperature, Af	76° C

Table 5.1   Transformation temperature of SMA Ribbon
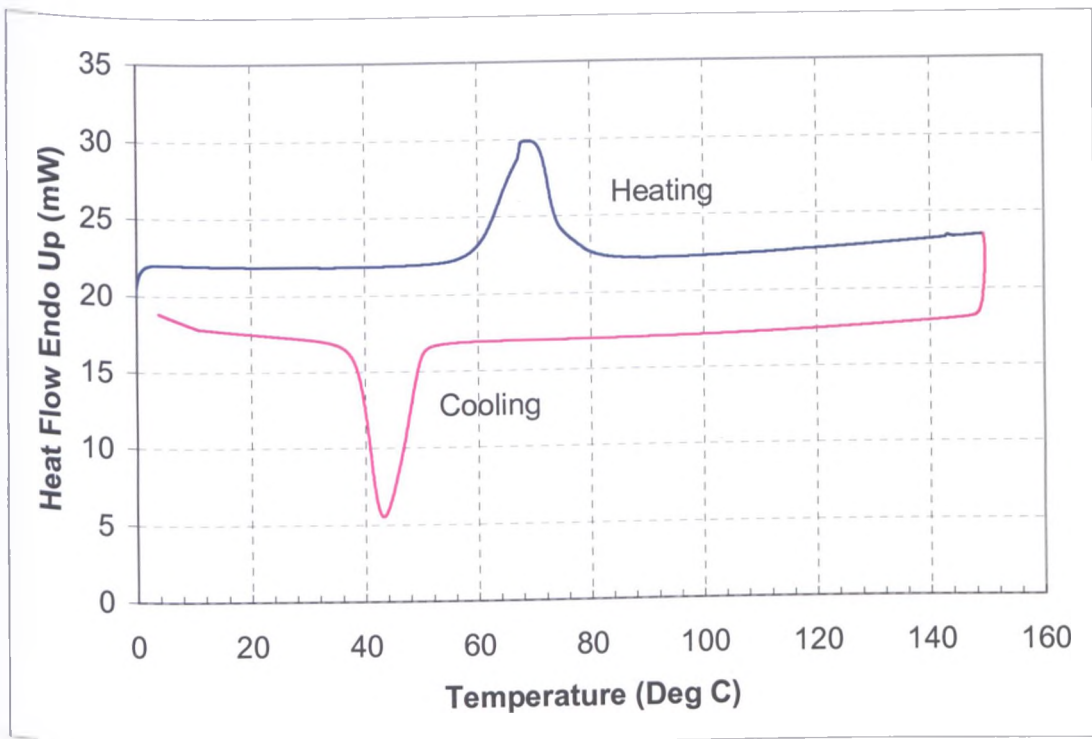
Figure 5.2 DSC Curve for SMA Ribbon

5.3   Tensile test of ribbon

The ribbon was first tested to determine its effective maximum strain as these properties depend on the type of SMA used. The overall tensile mechanical property of the SMA ribbon until failure was determined using an INSTRON 5567 universal testing machine with 15 kN load cell at room temperature. A very slow feed rate of 0.5 mm/min was used to avoid the influence of any strain rate effects.
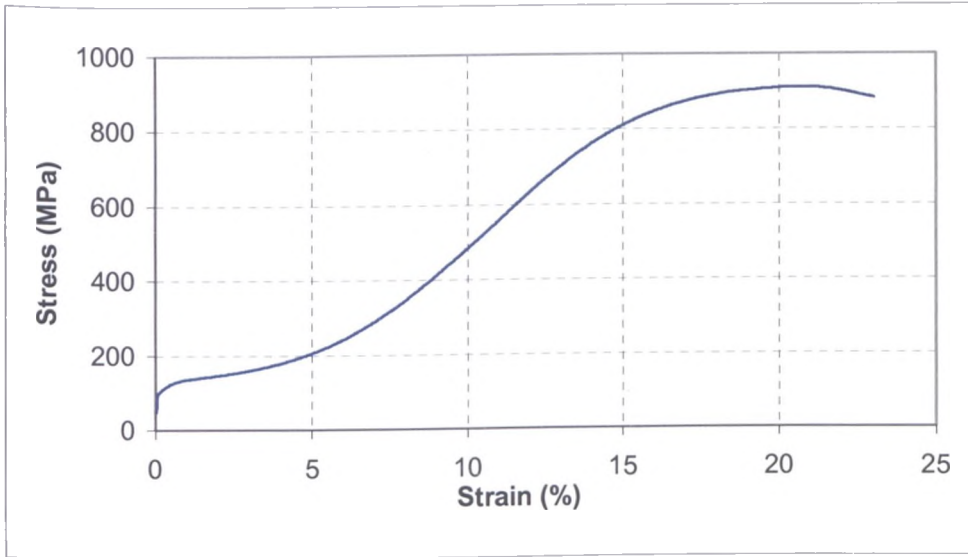
Figure 5.3 SMA ribbon tensile test – full martensite phase until fracture

The stress-strain curve shown in Figure 5.3 illustrates the first tensile test to depict the behaviour of the Nitinol alloy ribbon tested at room temperature (25°C) with loading in the full martensite phase. Tensile failure was reached at about 20% tensile engineering strain, with a pre-load of 100 Newton applied. To clearly visualise the elastic region of the alloy, another test was performed on a different sample. Figure 5.4 shows the tensile stress-strain curve loaded up to 8% of strain with 10 Newton of pre load. From the results shown, one can identify an elastic region up to 0.5%, with subsequent plastic and non-linear deformation up to 8%.
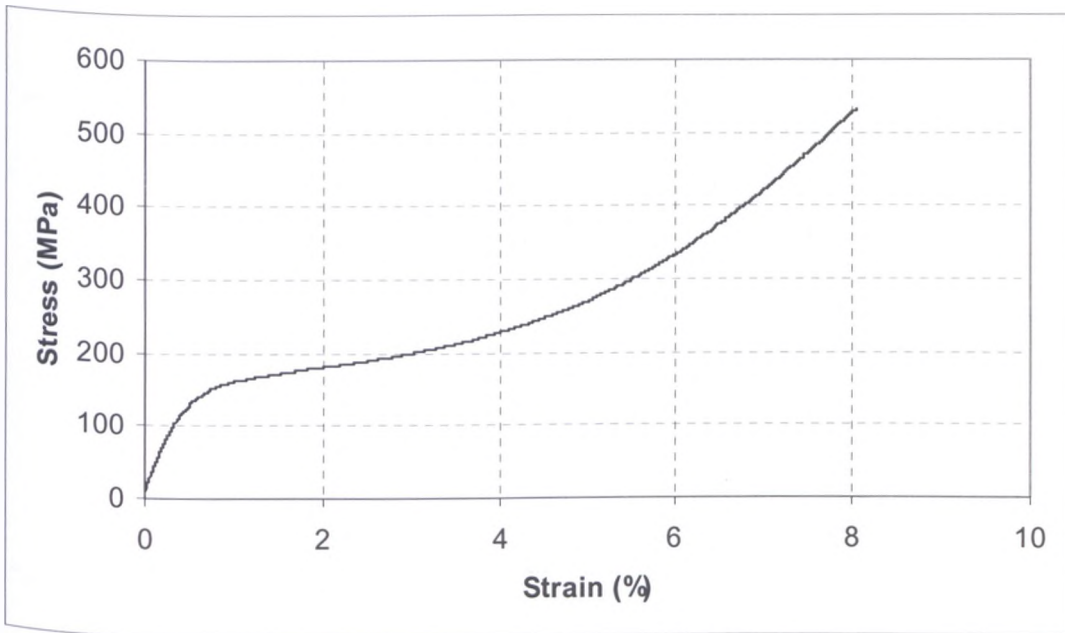
Figure 5.4 Tensile test for SMA ribbon to 8% strain

5.4 Cycle testing of SMA ribbon

The test performed was uniaxial loading and unloading of the SMA ribbon at full martensite (25°C) and above the austenite finish temperature (105°C). The single ribbon experiments were carried out using a Testometric M350-5KN tensile machine with environmental chamber as shown in Figure 5.5.

Figure 5.5 Testometric M350-5kN tensile machine

The tests were performed to determine the behaviour of the ribbon at martensite temperature and austenite temperature when subjected to cyclic loading conditions. It is very important to define the characteristic of the shape memory effect in the martensite region, as well as the pseudoelasticity in austenite region. This is important to determine the elastic and plastic region of the SMA. For this test, a feed rate of 0.5 mm/min was again chosen. From the test, residual strain for SMA at martensite region and permanent plastic deformation at austenite region can be determined. Figures 5.6 and 5.7 show the loading and unloading curves in the martensite phase (25°C) and austenite phase (105°C) respectively. Please be aware that the curve will always be different for different temperatures.
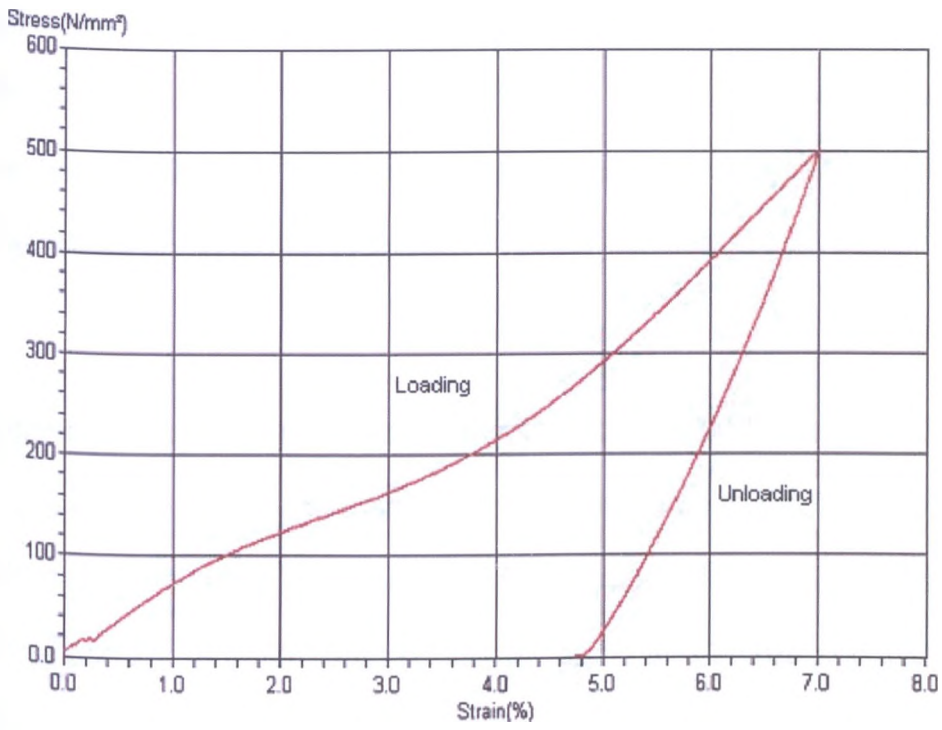
Figure 5.6 Cyclic test at full martensite (Temp 25°C)
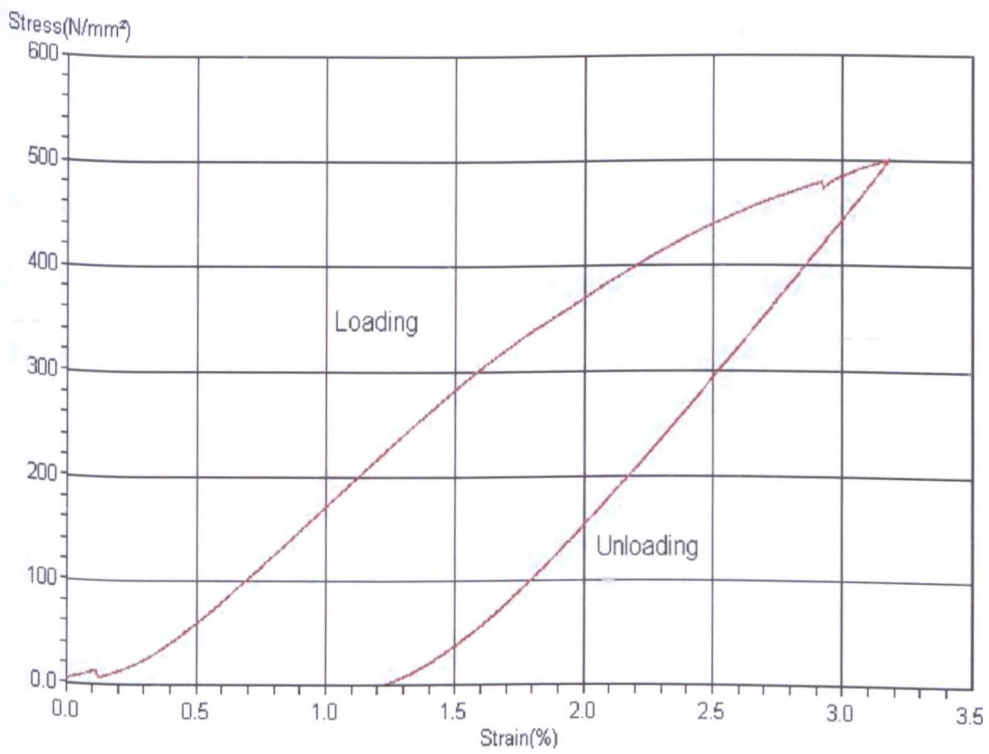
Figure 5.7 Cyclic test at full austenite (Temp 105°C)

From Figure 5.6, when the SMA ribbon is in full martensite structure, a residual strain of 4.8% can be noticed when the applied stress was released towards zero. Most of this residual strain can be eliminated upon heating to the austenite finish temperature.

However, for equivalent load at austenite phase, a permanent residual strain of 1.2% occurs, albeit with a smaller value compared to the one related to the martensitic structure. The linear elastic portion of the curves (during the loading phase) shows Young's modulus values of 8.7 GPa and 16.9 GPa for the martensite and austenite phases respectively. The stiffness ratio between austenite and martensite phases is therefore 1.9. Thus for a maximum load of 500MPa, in the martensite phases, the SMA ribbon can reach up to 7% strain, while in the austenite phase only 3.2% tensile strain.

The summary of the results is presented in Table 5.2. The modulus in the table was obtained based on the cyclic test. The ratio of modulus values between austenite and martensite of approximately 2 agrees with that reported in literature [Hodgson,1988].

	Modulus (GPa)	Max. tensile strain at 500MPa (%)	Residual Strain (%)
Martensite (25°C)	8.7	7	4.8
Austenite (105°C)	16.9	3.2	1.2

Table 5.2 : Summary of cyclic tests

5.5   Pre cycle the ribbon

In order to provide constant mechanical properties during the operational life of the component, in particular as an actuator, a SMA is usually subjected to a pre cycle process. In this work, the pre cycle ribbon was used for the DMA test. The process was similar to the training procedures that have been reported in the literature [Perkins & Hodgson,1990]. It was performed using a manual Hounsfield tensile machine. Initially the ribbon was loaded to 8% tensile strain at room temperature (full martensite), followed by the load release to zero. This operation resulted in a residual strain of 5%. The sample was then released from the machine and heated up to full austenite temperature (76°C). This caused the ribbon to return to the original length, eliminating the residual strain. The sample was again subjected, at room temperature, to a tensile load up to 8% of strain. The whole process (loading and unloading at martensite phase and heating until full austenite) was repeated for at least 30 cycles.

After the process, the SMA exhibited stable properties in terms of elongation and thermal profile, the latter being especially important for DMA tests. The curve of total length vs cycles for SMA ribbon at martensite and austenite region is shown in Figure 5.8. From the figure it is evident that length stability at martensite phase was reached after 30 cycle of training. This process can also be used to obtain the two way shape memory effect [Auricchio,2003]. Therefore, for the test similar to Figure 5.7, there will be no residual strain in the ribbon if it has already experienced more than 30 cycles of heating and cooling.
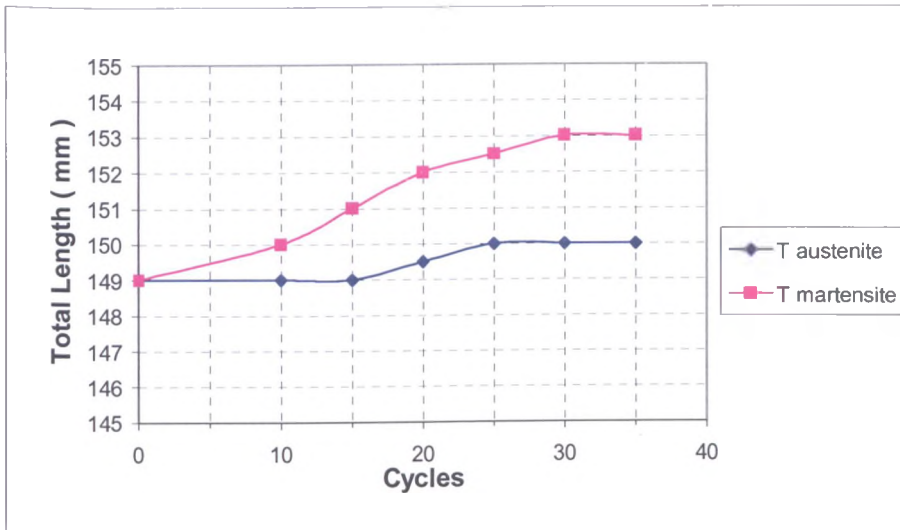
Figure 5.8   Pre-cycle of SMA ribbon

5.6   Dynamic Mechanical Analysis (DMA) Test

Dynamic Mechanical Analysis is a technique consisting of applying an oscillating strain to a sample and measuring the resulting stress developed [Metravib, 1999]. It is important to measure the viscoelastic properties of a material, in particular:

a. The stiffness of a specimen (*K*) is defined as the ratio of the force amplitude versus the displacement amplitude. The stiffness depends also on the specimen geometry.

b. The complex Modulus E* [Hu et al,2003] is calculated from the measured stiffness and intrinsic properties of the material.

c. The real part E' of the complex modulus is in-phase with the displacement. It is often called the storage modulus in the literature [Gandhi & Wolons,1999].

d. The imaginary part E" (viscous modulus or loss modulus) is out-of-phase with the displacement [Gandhi & Wolons,1999].

e. The phase shift (δ) between the force and the displacement is called the loss angle of the material.

f. The tangent of the loss angle (tan δ) is called the loss factor and corresponds to the damping of the material [Jones,2002].

In this study, the DMA machine used is a Viscoanalyser VA2000 developed by Metravib. In practice, the viscoanalyser was used to apply a displacement function of an harmonic pulsation d(ω) at the upper end of a sample. An harmonic force F(ω) was then measured, and the viscoelastic properties of the material then postprocessed.

The viscoanalyzer VA2000 can cover a combination of analysis domains, in terms of frequency range (0.001 Hz to 1000 Hz), available force range (+/- 0.001 N to +/- 450 N) and in terms of temperature (-150°C to + 450°C). The viscoanalyser that was used for the test is shown in Figure 5.9.

Figure 5.9   Viscoanalyser VA2000

The viscoanalyser test was carried out to determine the damping characteristics of the SMA ribbon. The equivalent viscoelastic tests (small dynamic amplitude) were performed on the trained ribbon, fixed to a custom-made aluminium clamp. Three different types of tests were performed, consisting of heating while applying a 5 Hz cycling loading (tension-tension), cooling while applying the same harmonic mechanical loading, and a master curve test for frequency range from 1 Hz to 60 Hz [Dimier et al,2004]. The ribbon was loaded with a sinusoidal excitation with constant dynamic displacement of 5.0 μm within the elastic region of the SMA ribbon.

For the first test, the ribbon was tested under tension-tension loading at 5 Hz for temperatures from 10° C to 110° C. At the beginning, the ribbon was

placed in the test chamber pre-loaded at room temperature with a 5N tensile load, corresponding to an offset tensile strain of 0.03 % in the full martensite phase. The temperature was then brought down to 10°C. The data were then collected for the test from 10°C to 110°C at a heating rate of 5°C/min. It has to be pointed out that the test chamber temperature was kept uniform across the volume using a fan, while the temperature was automatically monitored using a thermocouple inside the chamber.

The second test (cooling) was performed immediately after the heating process stopped at 110° C to obtain the complete cycle of heating and cooling of the ribbon. The data were collected using the cooling rate 5°C/min for the temperature from 110°C to 10°C.

The third test was performed to obtain the master curve for the SMA trained ribbon. In this test the values of loss factor and storage modulus, as well as shift factors [Hu et al,2003] were evaluated. From the previous tests (heating and cooling), the presence of significant changes in terms of loss factor between 50°C and 60°C were noticed. Therefore, for this test, over the temperature range from 10°C to 75°C, testing was carried out at the following frequencies; 1Hz, 1.5 Hz, 2.26 Hz, 3.41Hz, 5.14 Hz, 7.74 Hz, 11.66 Hz, 17.56 Hz, 26.4 Hz, 39.84 Hz and 60 Hz. The values were selected because the frequency was measured in logarithmic values. At each increment of 5°C of temperature, the ribbon was subjected to a series of harmonic tension-tension loading corresponding to the specified frequencies above.

All the results from the tests were then postprocessed using the DYNATEST software controlling the viscoanalyser machine. DYNATEST offers a wide range of representations in the form of tables, values and graphs, which can be accessed in the windows menu. The precision of the results mainly depends on the user competence while preparing the test.

From the Table 5.1, the Mf, Ms, As and Af can be identified as 38°C, 50°C, 58°C and 76°C respectively. The results from the viscoanalyser test for the heating and cooling are presented in Figures 5.10 and 5.11.
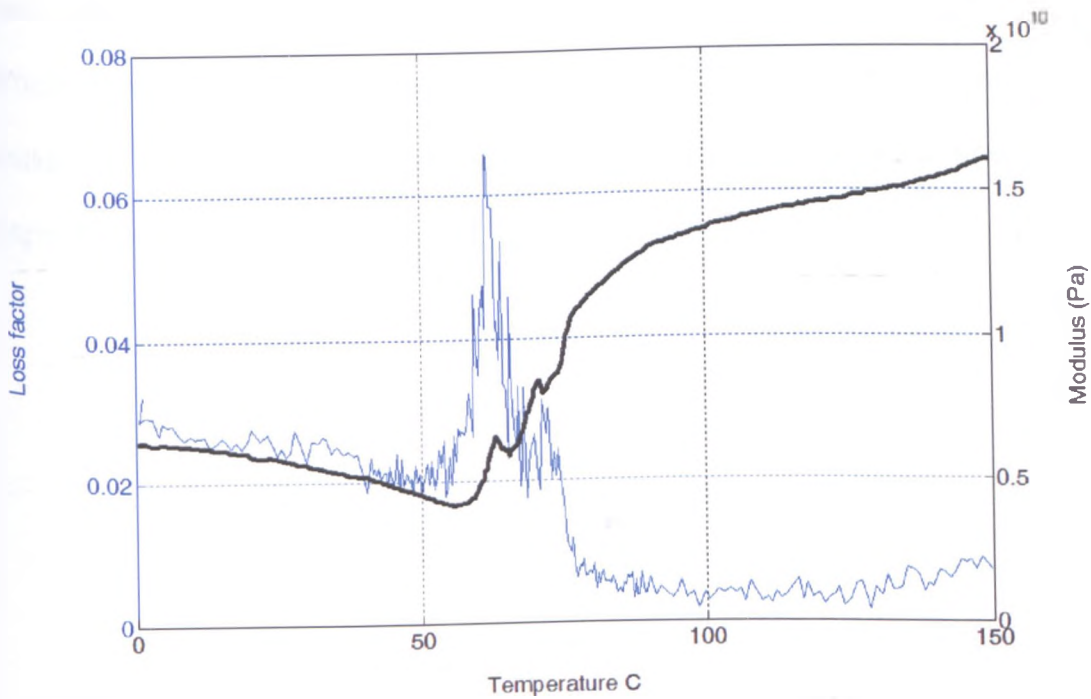
Figure 5.10 Storage modulus and loss factors of the ribbon during heating

Figure 5.10 shows the storage modulus and loss factor of the ribbon during heating when subjected to a sinusoidal loading of 5 Hz. This graph shows a significant variation of the storage modulus between 50°C and 100°C. From 0°C to 100°C, there are two significant change of structure occurring to the SMA at the austenite start temperature and austenite finish temperature. The storage modulus increases from 4 GPa at 55°C to 13 GPa at 100°C. As the temperature continues to increase above the Af temperature, the modulus increases slightly in value. However, in the martensite region, one can record a diminishing value of the modulus as temperature increases, while suddenly increasing when the phase transformation begins. This specific behaviour will be explained in discussion.

On the damping side, the damping peak can be noticed around 62°C. The loss factor suddenly reaches 6.5% compared to 2% at 50°C. After this temperature one can record a sudden drop to 1.5% after 76°C. Two small peaks can be noticed on the modulus curve, occurring at 62°C and 76°C respectively.
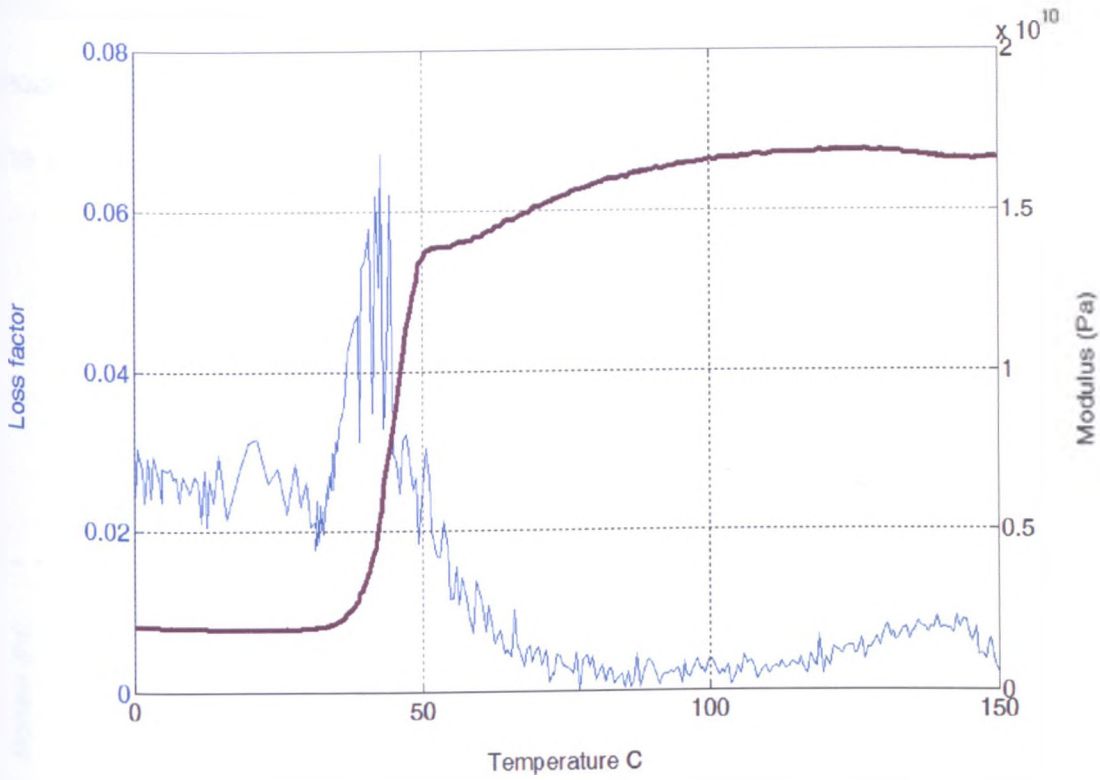
Figure 5.11   Storage modulus and loss factors of the ribbon during cooling

Figure 5.11 shows the cooling process or reverse process of heating for the same sample (from right to left). The storage modulus is almost constant during the whole austenite phase, between 150°C and 100°C, starting. to decrease slightly from 100°C to 50°C, while declining dramatically between Ms (50°C) and Mf temperatures (38°C). At full martensite phase, the storage modulus is constant, giving a modulus ratio of 5. The loss factor presents at value less than 1% in austenite phase. A sharp peak reaching a maximum value around 6.5% occurs in the transition zone, similar to the heating phase. In the martensite region, the loss factor assumes an average value of 2.5% over the temperature range.

Figure 5.12 shows the storage modulus of the SMA ribbon over temperature at different frequencies from 1 Hz up to 60 Hz during the heating process.

Within the selected frequency range, it can be noticed that the storage modulus is almost independent of the excitation frequency, including during the austenitic transition phase.
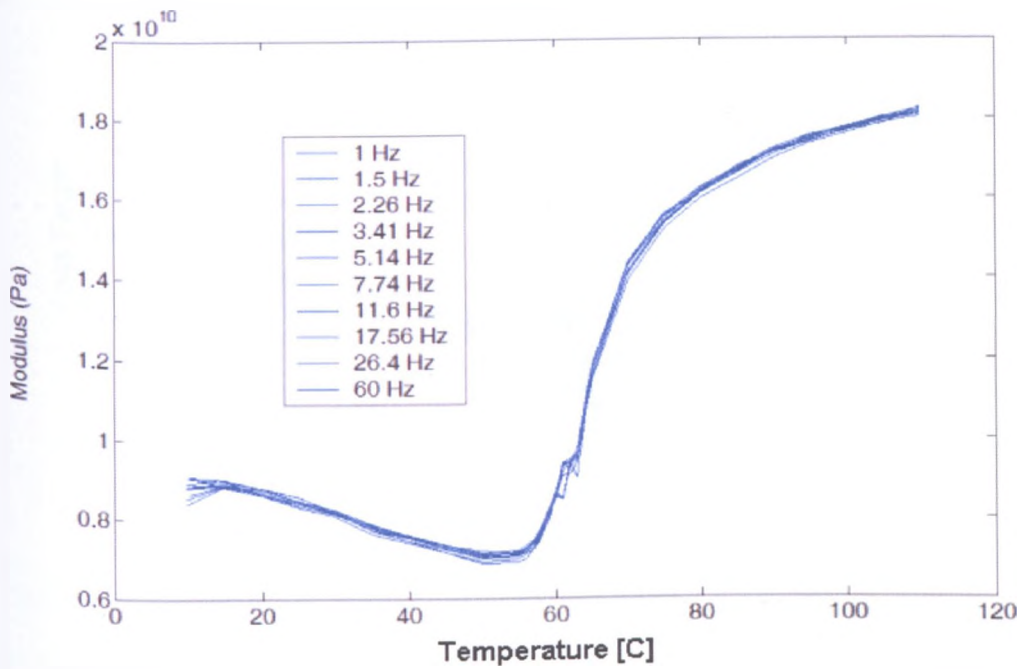
Figure 5.12 Storage modulus versus temperature for different frequencies

Figure 5.13 shows the results of the frequency dependent test on the storage modulus of the ribbon during the heating process at various excitation frequencies indicated in Figure 5.12. For completeness, the behaviour of the loss factor with frequencies is also presented in Figure 5.13. The loss factors corresponding to the first six frequencies (from 1 Hz to 7.74 Hz) are shown with a star mark (*), while the other values are represented with a circle (°). The behaviour of the loss factor for the first six frequencies of excitation is similar, with a major peak around the phase transition, and decreasing value for the austenite form. At higher frequencies, the loss factor of the martensite

phase increases significantly, while the sharp clear peak during the phase transformation seems to disappear.
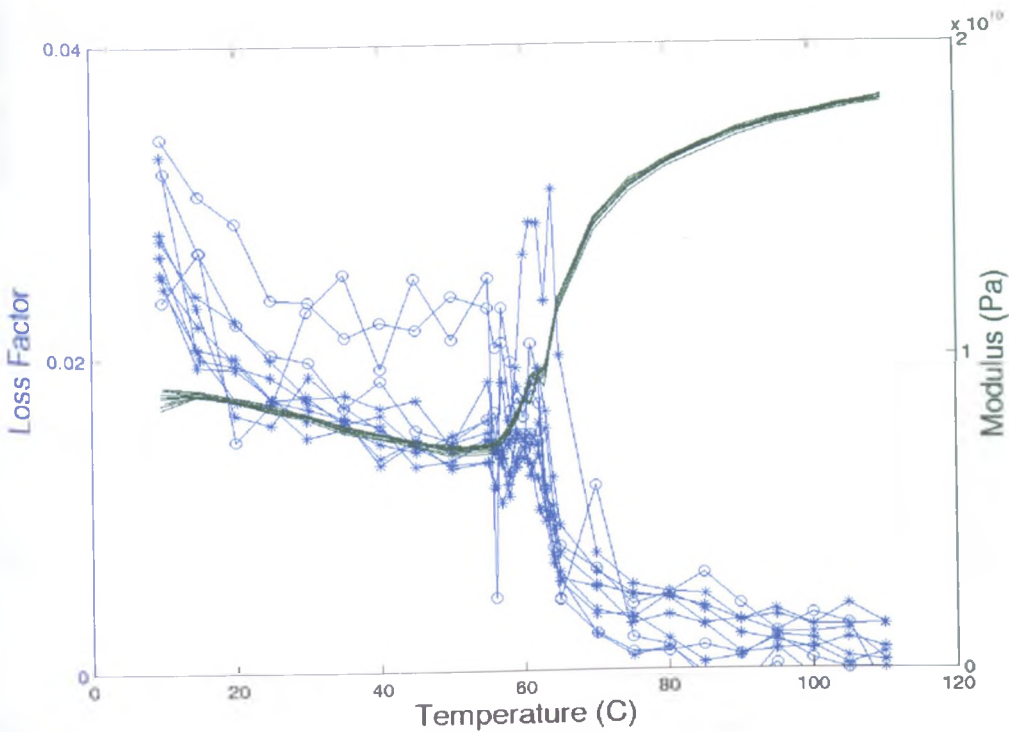
Figure 5.13 Storage modulus and loss factor versus temperature and frequency

5.7 Modelling the SMA ribbon

Figure 5.14 shows the comparison between the single ribbon nonlinear FE model and the experimental results up to 8% tensile strain. The original data obtained from FE model were load and strain. The FE model represents with significant accuracy the uniaxial tensile loading behaviour of the full martensite ribbon component, in particular the linear elastic behaviour, the first yielding point, the transition towards the plateau stress and the second elastic branch.
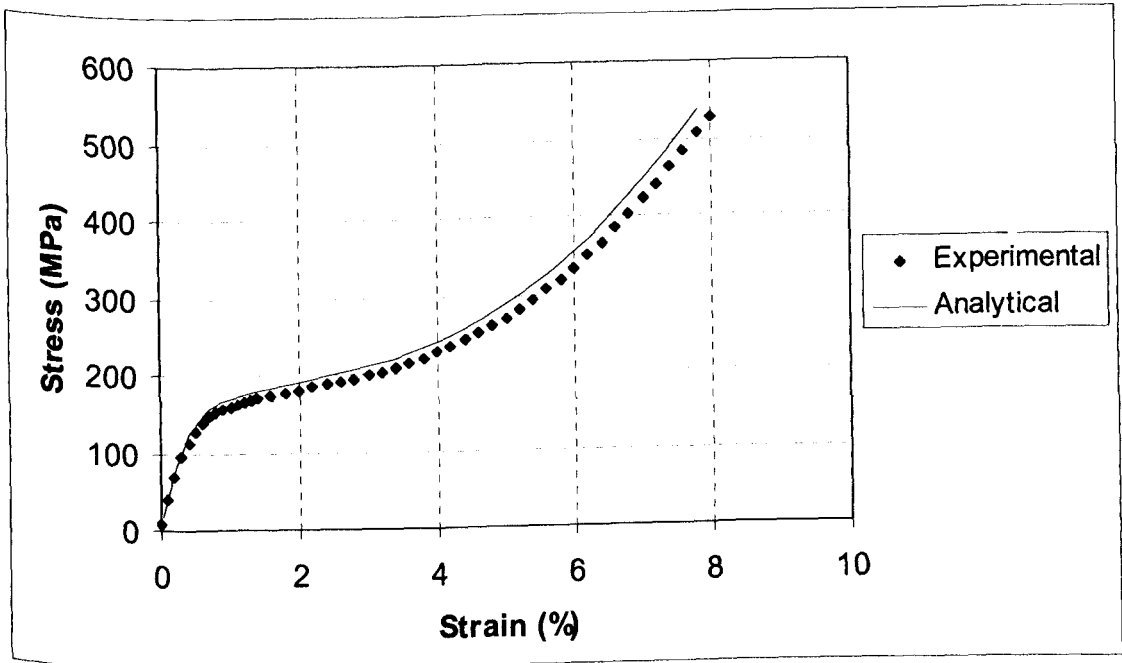
Figure 5.14 Comparison between FE and experimental results of tensile loading of SMA ribbon

These results indicate that the TB, MELAS option with BEAM23 element in ANSYS is capable of modelling the non-linear behaviour of shape memory alloys, when only strain-hardening capabilities have to be represented. This type of approach was therefore used to simulate the pure uniaxial tensile test for an equivalent large honeycomb structure.

Chapter 6

SMA HONEYCOMB TESTING AND RESULTS

6.1 SMA honeycomb manufacturing and testing

In this work, four types of honeycomb were manufactured, a hexagonal centresymmetric honeycomb with $\alpha=1$, hexagonal honeycomb with $\alpha=2$, an auxetic (re-entrant) honeycomb with $\alpha=2$ and a full cell of chiral honeycomb. A centresymmetric hexagonal honeycomb made of 6 X 4 cells and hexagonal honeycomb with $\alpha=2$ made of 4 X 4 cells was fabricated using the SMA ribbon. In fabricating the honeycomb, the untrained ribbon was used. For honeycomb, pre cycled or trained ribbon was not considered necessary because regular phase transformation was not expected.

6.1.1 Hexagonal and re-entrant honeycomb fabrication

The single layer of honeycomb unit cell was manufactured by joining two faces of the core ribbon using a few steps. Initially each ribbon was shaped into half honeycomb cell using a two-piece metal mould as shown in Figure 6.1a and Figure 6.1b. An aspect ratio α of 1 was chosen to represent a

conventional regular centresymmetric honeycomb. The technique of joining process that has been applied must maintain the temperature of the ribbon below the transformation temperature (58°C). The shaped pieces of ribbon will return to their original form (straight line), if the temperature reaches the phase transformation temperature.
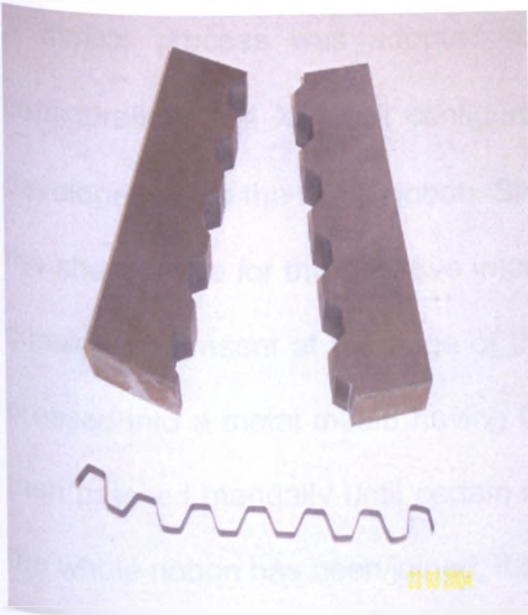
Figure 6.1a Mould for hexagonal honeycomb
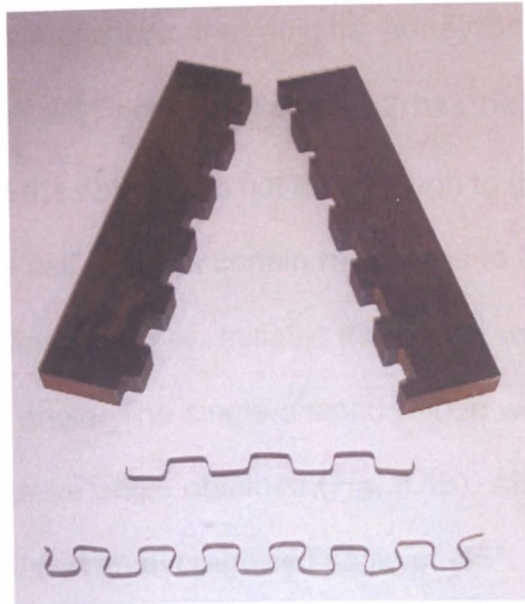
Figure 6.1b Mould for re-entrant honeycomb

A special high temperature resistance cyanoacrylate adhesive supply by Bondloc, designed to operate up to 200°C, was used to join two faces of the SMA ribbon. Before the joining, the oxide layer had to be removed in order to get a strong joint. The curing process for the glue took up to 3 hours; therefore the complete joining was completed using special clips as shown in Figure 6.2. The joining process was then performed layer by layer until a full honeycomb structure was obtained. For the 6 X 4 honeycomb, it required twelve SMA ribbons while for the 4 X 4 honeycomb, only eight ribbons were

used. The complete structure of the centresymmetric SMA honeycomb is shown in Figure 6.3a and 6.3b. The average cell angle obtained from the centresymmetric SMA honeycomb was 42 degrees even though the original angle at the block was 30 degrees. For the hexagonal honeycomb with $\alpha = 2$, the average cell angle was 40 degrees.

A similar process was adopted to manufacture the auxetic honeycomb configuration. A 4 X 4 cell configuration with aspect ratio α = 2 has been developed using the same ribbon. Since the ribbon was not thin enough to get the sharp angle for the negative internal cell angle, a certain radius has to be considered present at the edge of the final samples. Initially, the ribbon was pressed into a metal mould having 90° angle. The single-shaped ribbon was then pressed manually until certain negative angle obtained (Fig. 6.1b). After the whole ribbon has been joined, it exhibited an average cell angle of -15°.

Type	Num. of Cell	Dimension (mm)	Aspect ratio	Cell angle
Centresymmetric Hexagonal	6 x 4	135 x 82	1	42
Hexagonal	4 x 4	200 x 72	2	40
Centresymmetric re-entrant	4 x 4	140 x 100	2	-15

Table 6.1   Type of SMA honeycomb
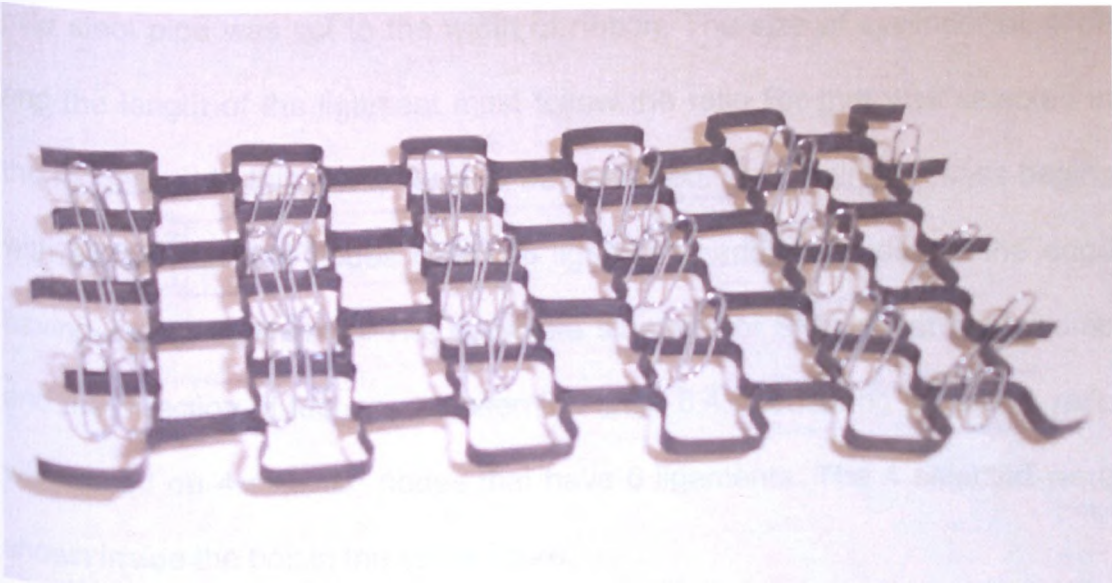
Figure 6.2 Re-entrant honeycomb during curing process
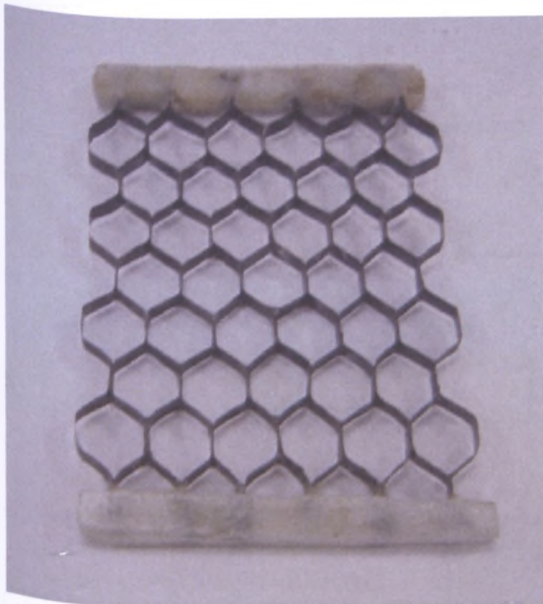
Figure 6.3a Hexagonal honeycomb   6.3b Auxetic honeycomb
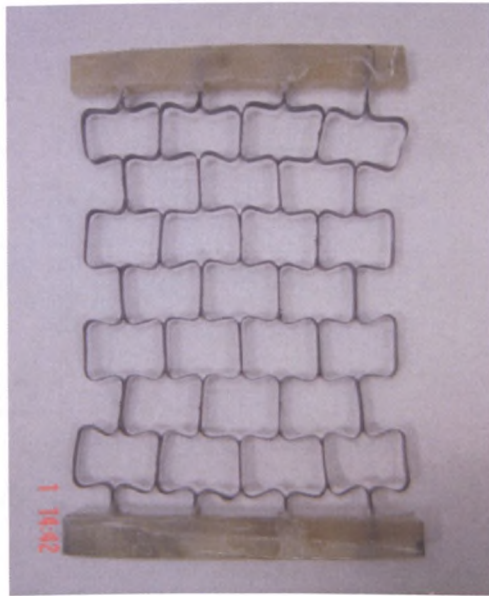
6.1.2 Chiral honeycomb fabrication

A few cells of chiral honeycomb were fabricated using two types of materials. The ligaments of the chiral honeycomb were made from SMA ribbon while the nodes or cylinders were made from mild steel. Mechanical fastening (screws) were selected. Firstly, the ribbon was cut to length for such ligament. Then the

mild steel pipe was cut to the width of ribbon. The size of cyclinder or node and the length of the ligament must follow the ratio R/r that was selected in the modelling. In this work, R/r of 5 was selected. The joining process begins with all the selected nodes having 6 ligaments, and the nodes at the edge having 3 or 4 ligaments. The complete structure of SMA chiral honeycomb and the direction of test can be seen in Figure 6.4. Measuring Poisson's ratio was based on 4 selected nodes that have 6 ligaments. The 4 selected were shown inside the box in the same figure.
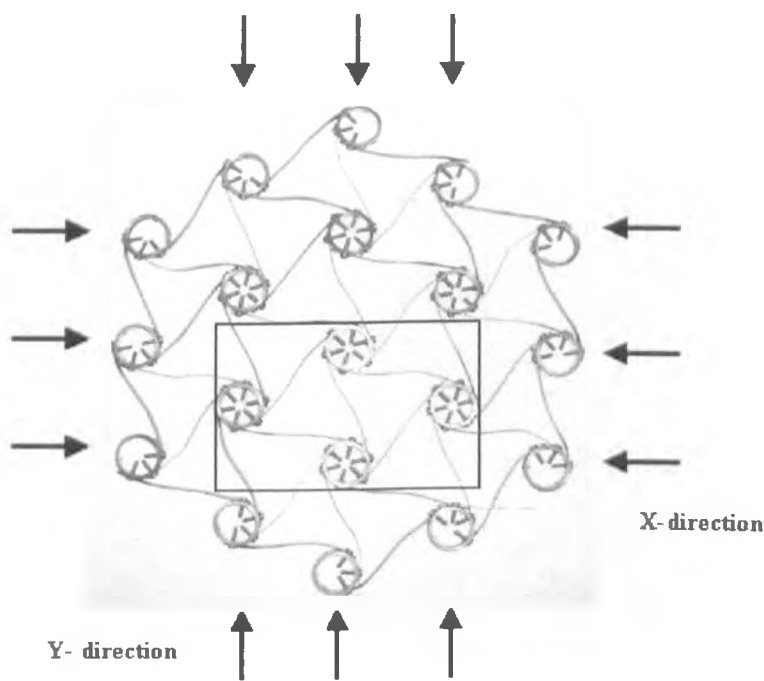
Figure 6.4   Loading directions of chiral honeycomb

6.1.3 Centresymmetric Honeycomb Tensile Test

The tests on the honeycomb samples were conducted on an INSTRON 5567 universal testing machine with 5 kN load cell at room temperature. A special frame in cast epoxy resin was applied at the top and bottom of the

honeycomb samples to fix the cellular solids to the clamps. The complete structure of hexagonal and auxetic honeycomb with the frame is shown in Figure 6.3a and 6.3b. It was observed that with the use of the epoxy resin frame, the vertical and horizontal displacements of the constrained sides of the honeycombs were virtually zero when loading in the vertical direction. The attachment of the honeycomb-epoxy frame combination to the tensile machine grips was assured using a special steel extension rod. The feed rate for the tensile testing of the honeycomb samples was 0.25 mm/min. Figure 6.5 shows the honeycomb during testing. The images of the honeycomb during the test was captured every two minutes.

Figure 6.5   Honeycomb during testing

6.1.4 Chiral honeycomb test

The test for measuring the Poisson's ratio was carried out for the chiral honeycomb. The test only involved compression of the chiral honeycomb in the austenite region (105°C). It was tested in this region due to a potential future application of chiral honeycomb. The chiral honeycomb has been seen to have great potential to work in pseudoelastic effect because all ligaments are in very strong condition in the austenite phase.

In order to allow the honeycomb to wind freely at the node, the honeycomb was placed in a special metal slot. To allow the honeycomb to stay in the slot, a small pre strain was applied to the honeycomb. The position of the chiral honeycomb in the slot during the compression test inside the environmental chamber is shown in Figure 6.6.

In this test, the feed rate used was 5 mm/min. After trials, it was noted that a lower feed rate did not make any significant difference to the accuracy of the test results. The output data for this test was obtained from images captured using a Sony DSC-F828 digital camera. The image was captured every 1 minute. The images show the location of the 4 nodes measured in the test. The camera must be set up at the same configuration and was located 500 mm from the test specimen.

Figure 6.6   Chiral honeycomb during compression test

6.1.5 Poisson's Ratio Measurement

The Poisson's ratio of the honeycomb was obtained by post processing the images captured during the test. A Matlab-based program was used to measure the locations of the honeycomb nodes. The program required a picture at each stage. From the locations of the nodes, one can measure the expansion or contraction between two nodes. These data are then used to calculate the strains along the X and Y directions. The in-plane Poisson's

ratios of the honeycomb were then evaluated using standard definitions. The Matlab program for the image processing is listed in Appendix D.

The image processed for the chiral honeycomb is shown in Figure 6.7a and 6.7b. The exact location for the 4 nodes can be obtained using the zoom function in the Matlab figure file window as shown in Figure 6.7b. The dimension obtained from this window was not scaled in metric units but based on pixels.
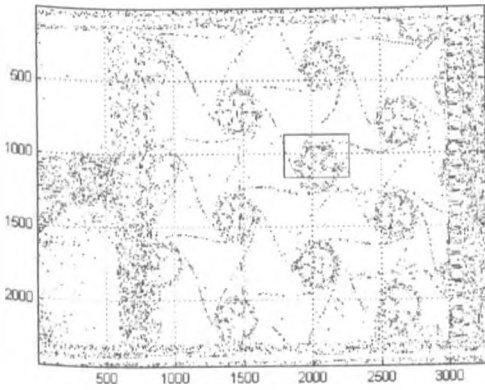
Figure 6.7a   Image chiral honeycomb in full window
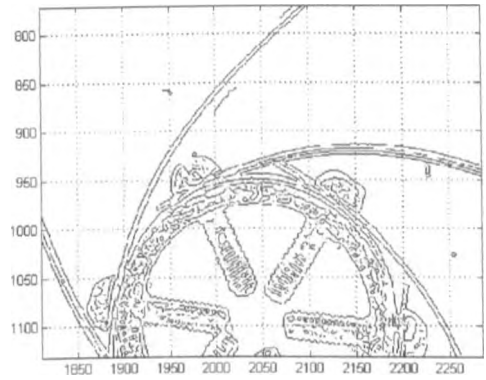
Figure 6.7b   Image chiral honeycomb in zoom window

6.2 SMA Honeycomb Results

In this section, the results from uniaxial tensile loading of centresymmetric hexagonal and re-entrant honeycombs are presented. The behaviour of the Poisson's ratio for the hexagonal, re-entrant and chiral honeycomb are also described. All experimental results have been carried out in the martensite region, except for the case of Poisson's ratio of the hexagonal chiral honeycomb. The motivation behind the particular loading condition of the hexagonal chiral honeycomb is explained in section 6.1.4.

6.2.1 Hexagonal centresymmetric honeycomb

At the beginning of this work, the hexagonal centresymmetric honeycomb with $\alpha = 1$ ($\theta = 42°$) was used to evaluate a basic honeycomb configuration representing a classical honeycomb structure with double thickness cell walls. A comparison of measured and predicted behaviour under tensile loading is shown in Figure 6.8.
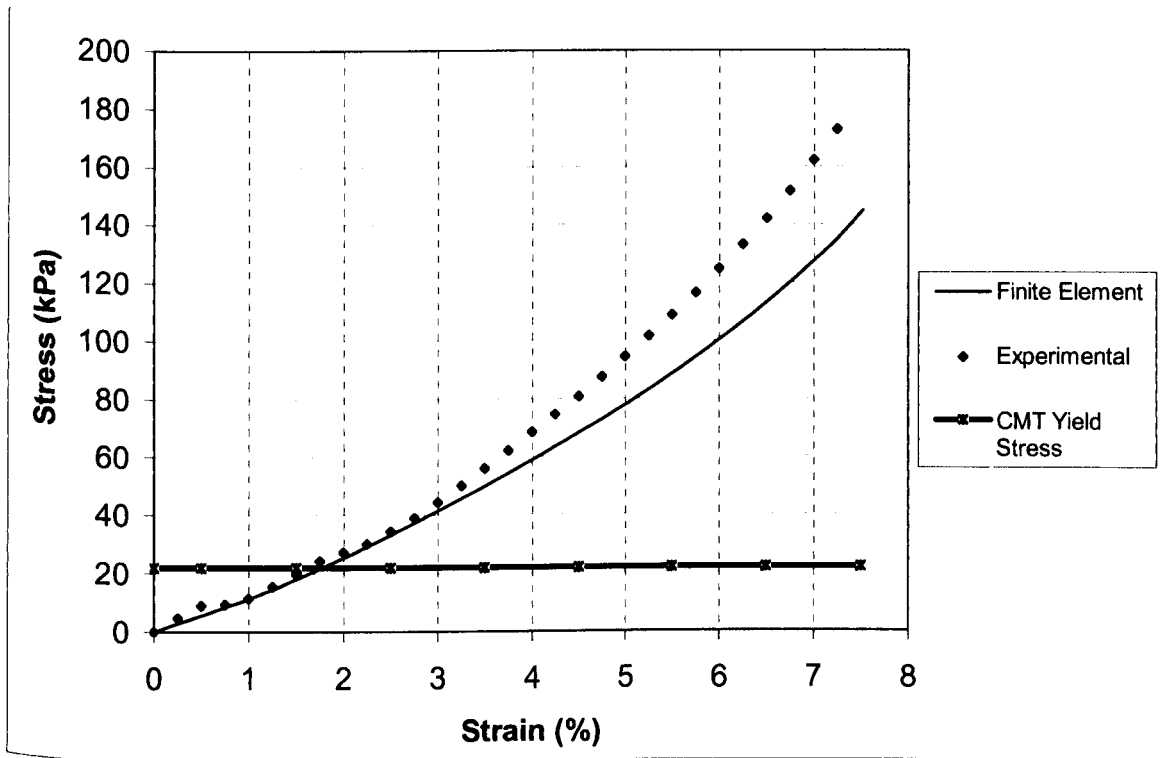
Figure 6.8 The result of tensile test for hexagonal honeycomb $\alpha = 1$

One can observe good agreement between experimental and FE non-linear analysis. The topology of the curve is as expected for positive Poison's ratio centresymmentric hexagonal honeycombs under tensile loading. Further explanations of the result are discussed in the next chapter.

6.2.2 Re-entrant centresymmentric honeycomb

The results for the uniaxial test of the re-entrant honeycomb are presented in Figure 6.9. The elastic modulus obtained from the FE analysis is slightly higher compared to the experimental one. For example, at 15% strain, 6% higher stress can be noticed for the experimental data compared to the FE

analysis. However, the shapes of both curves also represent the behaviour induced by the presence of an in-plane negative Poisson's Ratio. Further tensile loading would result in the honeycomb cells assuming a hexagonal shape, changing from re-entrant to convex configuration. The results presented in Figure 6.9 are only up to 17% of strain, where the honeycomb cells still retain a general re-entrant structure.
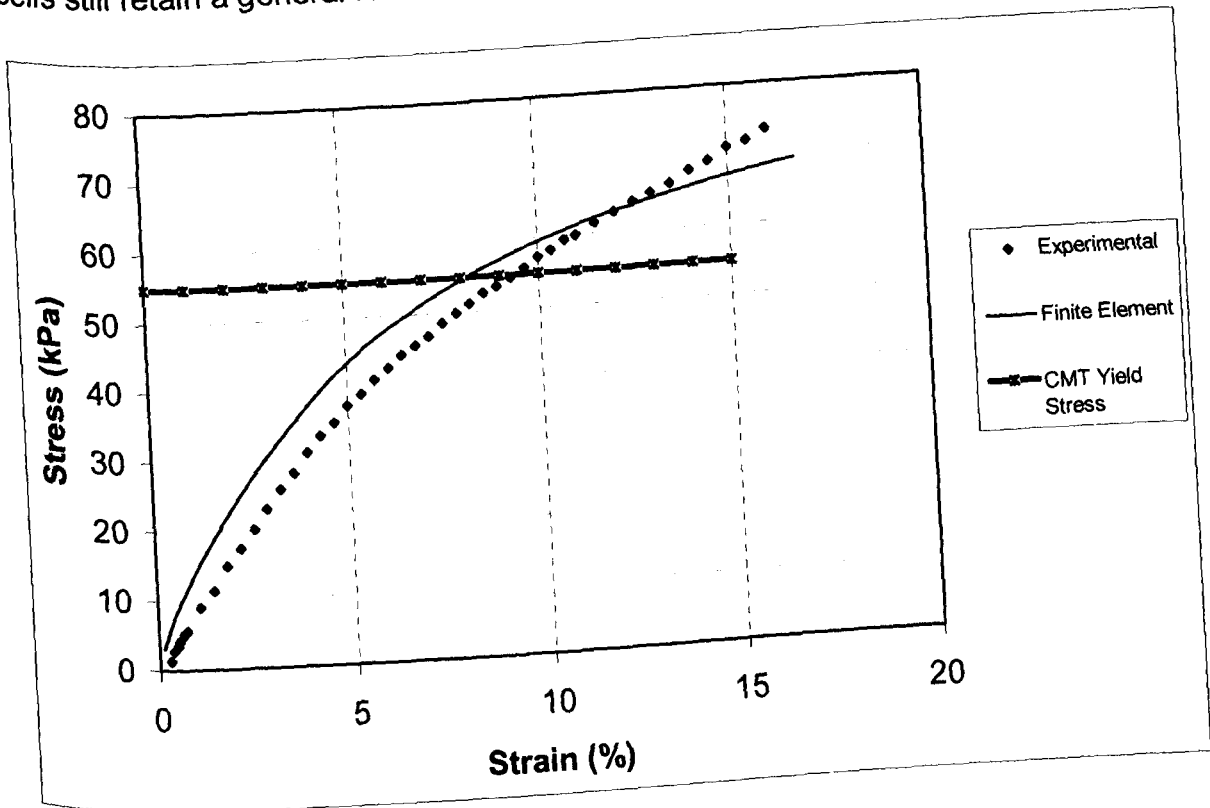
Figure 6.9 Re-entrant Honeycomb $\alpha = 2$

6.2.3 Analysis of CMT approach

The results in Table 6.2 are based on the results related to the hexagonal honeycomb for $\alpha = 1$. The table highlights the comparison between Equations 4.3 and the linear elastic FE models representing the theoretical boundary conditions and reduced size.

CMT (Eq. 4.3)	FE Static (24x16 cells)	FE Static (6x4 cells)
238 kPa	237 kPa	232 kPa

Table 6.2 Comparison the linear elastic modulus of hexagonal honeycomb $\alpha = 1$

As one can observe, there is agreement between the CMT approach and the FE linear elastic results, also when reduced size samples are considered, with a maximum percentage error of 2 %.

A further comparison between the nonlinear FE and the experimental results of hexagonal honeycomb $\alpha = 1$ is also shown in Table 6.3.

FE nonlinear	Experimental
1.15 MPa	1.45 MPa

Table 6.3 Comparison the modulus of FE and Experimental of hexagonal honeycomb $\alpha = 1$

A major effect was given by the presence of fully clamped conditions (translations and in-plane rotations) applied to the experimental sample. In this case, the linear FE analysis would provide a 4.8 times overestimate compared to the CMT approach. This is in good agreement with the experimental results and the nonlinear FE analysis, for which a comparison is shown in Figure 6.8. The nonlinear FE model predicts a slightly smaller initial elastic slope (1.15 MPa against 1.45 MPa).

6.2.4 In-plane Poisson's ratio of hexagonal and re-entrant centresymmetric honeycomb

Figures 6.10 and 6.11 show the results related to the Poisson's ratio of hexagonal and re-entrant centresymmetric SMA honeycombs for 4x4 cell with α = 2. For a maximum up to 10% of displacement along the Y direction of the hexagonal honeycomb, the simulation has shown that the Poisson's Ratio ranges between 2.5 to 4. However, the experimental results show the Poisson's ratio varies instead between 1.5 and 2.2.
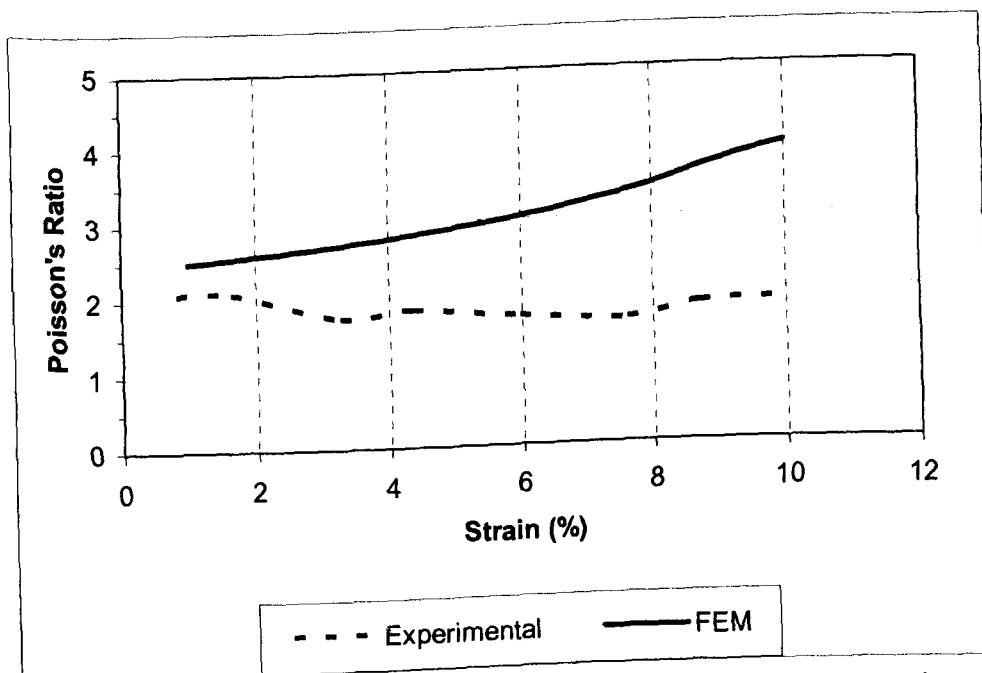
Figure 6.10 Poisson Ratio versus strain for hexagonal honeycomb α =2

For the re-entrant honeycomb, the FE simulation shows a range of available Poisson's ratios between -0.3 to -0.2 for tensile strains from 1% to 10%. The experimental test reveals that, for a tensile strain interval between 1% and 9%, the honeycomb exhibits negative Poisson's Ratio behaviour. For higher

strain loading, the honeycomb starts to display positive Poisson's ratio values. The overall range of Poisson's ratio for the test is from -0.3 to 0.1.
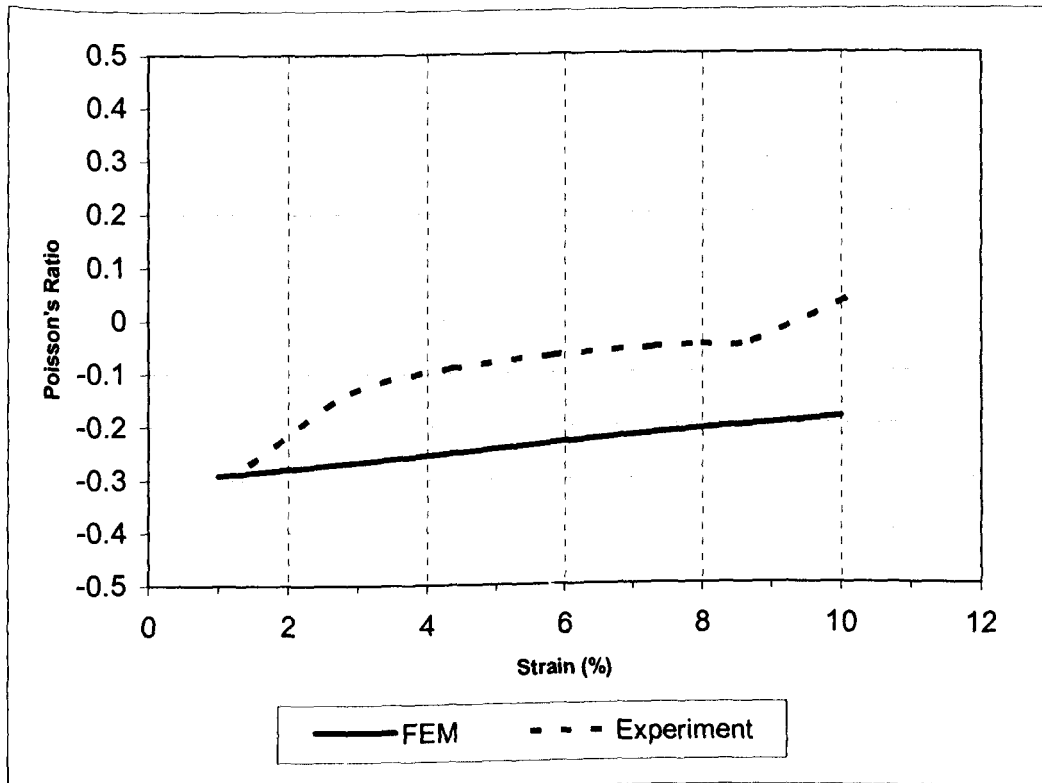
Figure 6.11 : Poisson ratio of auxetic honeycomb α =2

6.2.5 Results of the Poisson's Ratio for the Hexagonal Chiral Honeycomb

The results for the Poisson ratio of the hexagonal chiral honeycomb was obtained from the measurement of the strains for the four nodes as explained in the Section 4.6. In the martensite phase, the ligaments can be easily wound on the cylinder of the chiral structure. When heated, the same ligaments tend to straighten and therefore the chiral honeycomb structure will expand in all directions.

Since the chiral honeycomb is a 2D isotropic structure [Prall&Lakes, 1997], it is assumed that the expansion of the structure due to phase transformation will be the same. The numerical results for expansions along the X and Y directions show a general trend towards -1 as the tensile strain increases. To verify the numerical model, a compression test at austenite phase was carried out on the manufactured honeycombs. The result of the test is presented in Figure 6.12. Based on the simulation results, within the range between 1% to 20% compressive strain, the Poisson's Ratio along Y direction ranges from -0.95 to -1.05 while in X direction, the range is between -1.22 to -1.32. For the experimental test, both directions have shown an average value towards -0.75.
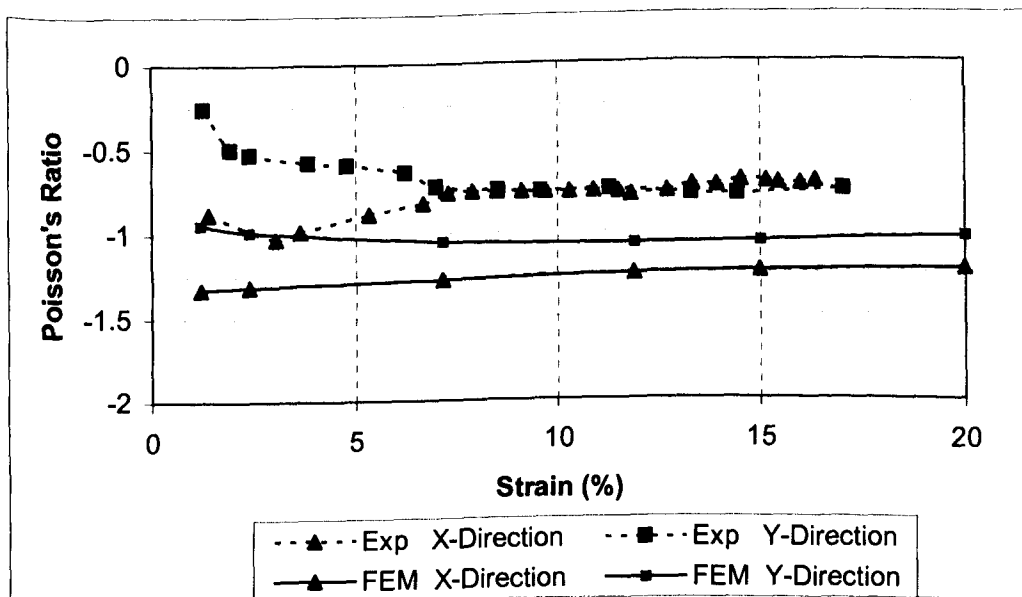
Figure 6.12 Poisson's Ratio vs. strain for Chiral Honeycomb structure.

Chapter 7

DISCUSSIONS

7.1 Shape memory alloy ribbon

7.1.1 Static test of ribbon

Nitinol components (in particular wire) are reported in the literature (Qidwai & Lagoudas, 2000) as having an effective operating maximum strain of about 8%. This value is based on engineering strain. Therefore understanding the behaviour of SMA within this region is very important.

Based on Figures 5.3 and 5.4, at initial loading, the specimen exhibited linear elastic behaviour until the first yield point at 120 MPa and 0.5% of strain, after which the stress was nearly constant at increasing strain loading. After the plastic deformation plateau, the specimen reached the second elastic region. Continuing the application of the load one would obtain a stress-strain path tending towards the second yield point (890 MPa), which is the true plastic deformation of the martensite structure SMA ribbon at 20% of tensile strain. When it reaches this region, it will not recover its original dimensions and tends to fail. Therefore, the ribbon fails at 23% strain. From Figure 5.4, the

ribbon showed elastic deformation up to 0.5% of strain before the start of plastic deformation. The modulus of the ribbon was defined in this region. Please note that all the strain mention in this work was based on the engineering strain.

For the test in the martensite phase, the phase transformation of martensite from twinned to detwinned appeared to happen at the plateau region. On the other hand, for the test in the austenite phase, the phase transformation from austenite to martensite happened at the plateau as well. This is called stress induced martensite.

7.1.2 Residual Strain of SMA Ribbon

Based on Figures 5.6 and 5.7, a cyclic test has been performed to define the residual strain of SMA as the stress was released from the sample. Table 5.2 has shown the residual strain of SMA ribbon in the austenite phase and the martensite phase. In the martensite phase, this residual strain can be recovered upon heating to the austenite finish temperature (76°C). This residual strain is very important in the design of actuators that works with the principle of the shape memory effect.

In Figure 5.7, the SMA ribbon was tested in the austenite phase. Upon loading, the austenite structure changed to stress induced martensite. It happened after 2% of strain even though it is not clearly shown on the curve. When the load was released, the stress induced martensite changed back to

austenite structure again. From the same figure, one can notice a permanent residual strain for 1.2%, which tended to decrease as the number of cycles increased. Based on the pre cycle test illustrated in section 5.5, the ribbon showed stability after 30 cycles. In order to remove the permanent residual strain in the austenite region, the SMA must be subjected to precycle at least 30 cycles. This step is very important in designing actuators working under pseudoelastic behaviour.

7.1.2 Effect of strain rate

The shape of the stress-strain curves that have been presented in this work is common for SMA alloys made from polycrystal nickel titanium alloys. Our specimens are derived from polycrystal NiTiCu alloys. If the specimen were made from single crystal CuAlNi, it would exhibit an extremely flat stress plateau during transformation as shown in Figure 2.4.

Few comprehensive studies on macromechanical investigation during tension of single crystal [Howard & Shield 1995] and polycrystal [Brinson et.al, 2002; Brinson et.al, 2004] martensite have been reported. The microstructure of the martensite structure is shown in Figures 7.1 and 7.2. As mentioned in the literature [Brinson et.al, 2002], with increasing strain rate, the threshold stress increases slightly and a significant slope to the transformation regime is observed. The reverse transformation stress increases significantly, resulting in a decrease in the width of the hysteresis cycle. Therefore, for cyclic SMA loading, a slower rate of strain is preferable to obtain a constant result. In this

case, the rate of 0.5 mm/min has been used. Therefore, using a slower rate, (i.e., 0.25 mm/min), one could expect lower stresses and larger hysteresis loops, as illustrated in Figure 5.7.

Figure 7.1 NiTi polycrystal [Brinson et.al, 2004]
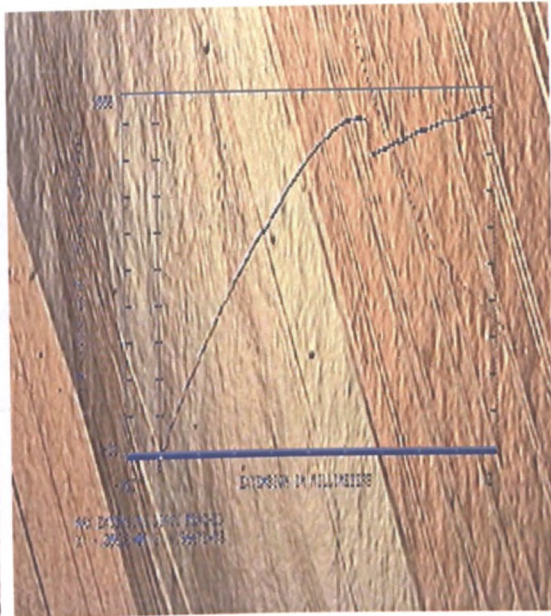
Figure 7.2 CuAlNi Single crystal [Howard & Shield,1995]

7.2 Damping Characteristic of SMA Ribbon

Figure 5.10 shows the storage modulus and loss factors of the ribbon during the heating process and subjected to a sinusoidal loading of 5 Hz. The values of the storage modulus were obtained using:

$$E_s = k \cdot F_c \cdot F_f \qquad \qquad \dots (7.1)$$

Where k is the measured stiffness [N/m], F_c is the correction factor:

$$F_c = E \cos \delta \qquad \qquad ...(7.2)$$

Where δ is phase angle and E is the complex modulus. F_f is defined by,

$$F_f = h/S_e \qquad \qquad ...(7.3)$$

Where h is the specimen height and $S_e = b \cdot t$ is the specimen cross section. The loss factor (or tangent modulus) has been computed using the classical formulation [Sun & Lu,1995]

$$\tan \delta = \frac{E_I}{E_S} \qquad \qquad ... (7.4)$$

Where E_I is the imaginary part of the SMA complex modulus, and E_S the storage modulus. The results were post processed using the DYNATEST software controlling the DMA machine.

7.2.1 Storage modulus

The storage modulus represents the stiffness of a viscoelastic component and is proportional to the effective Young's modulus of the SMA material by a factor of 0.64. The storage modulus tends to increase after the As temperature, with a significant increase during the transformation phase. More specifically, two peaks of the storage modulus are present around As and Af temperatures. The storage modulus tends to increase further until full

austenite, with a gradual build up of the real part of the complex modulus until 150°C. The ratio of storage modulus between austenite and martensite phase is 2.6, well in line with the ratio of Young's modulus between austenite and martensite phase recorded during the quasi static tests.

From Figure 5.10, one can notice that in the martensite region, the storage modulus tends to decrease as the temperature increases. A similar phenomenon has been reported by Cross [Cross et.al, 1969] and Turner [Turner et.al, 2001]. The results by Turner are shown in Figure 7.3, related to a material having As and Af at 40°C and 60°C respectively. Recently Wang and Wu from the University of Birmingham have provided information on temperature effects related to the modulus of Ti49.9%Ni [Wang&Wu, 2006]. The modulus of this specific SMA changes with temperature, with the lowest modulus value at 80°C. This temperature was very close to the As temperature. The stress strain curves at different temperatures are shown in Figure 7.4.
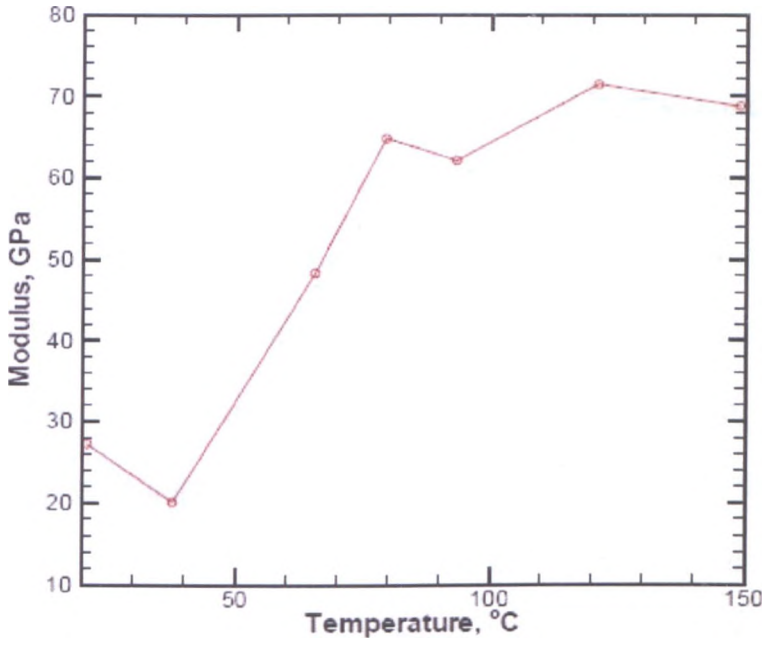
Figure 7.3   Modulus vs temperature for Nitinol Ribbon (Turner et.al, 2001)
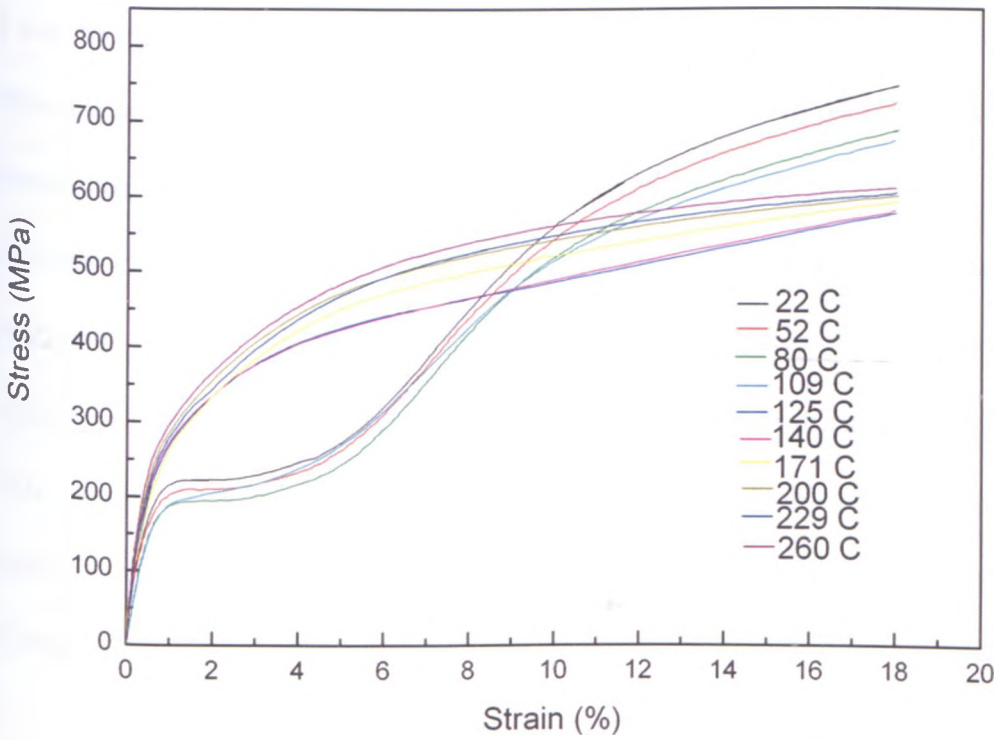
Figure 7.4 Tensile testing results for Ti49.9%Ni
(Courtesy of Wang and Wu, The University of Birmingham)

7.2.2 Loss Factor

From Figures 5.10 and 5.11, a loss factor features some interesting characteristics. The loss factor shows an almost constant damping value of 2%, with a subsequent steep increase to around 6% at the austenite start temperature (58°C). In principle, a second (smaller) peak could arguably be identified around the Af temperature. The loss factor of the full austenite phase has average values around 1%, well below the ones of the martensite phase, as the illustrated in literature [Piedboeuf & Gauvin,1998; Biscarini et al.,2003; Lu et al.,2003 and Zak et al., 2003]. A step increase of loss factor up to 6% is recorded during the transition phase, while a smaller peak could always be identified around Af temperature.,

It can be noticed that the peak of the loss factor (or damping peak) occurs at different temperatures even for the same specimen. The peak location in the temperature domain is heavily dependent on the condition of the thermal process experienced by the SMA. For heating conditions the damping peak occurs at the As temperature (58°C), while in cooling the damping peak occurs at the Mf temperature (38°C). At the As temperature, the structure of SMA is still 100% martensite, while at Mf all the structure in SMA has already become martensite. Both peaks therefore happen at the full martensite phase.

7.2.3 Frequency dependence

The result presented in this work was based on $Ni_{48}Ti_{46}Cu_6$ subjected to pre cycle for 30 cycles. The presence of peaks (Figures 5.10 and 5.11) during heating have been recorded as transition peaks P_{H1} and P_{H2} in $Ni_{30}Ti_{50}Cu_{20}$ alloys [Biscarini at.el.,2003], although transition effects tend to disappear above frequencies of 1 kHz.

Based on Figure 5.13, the behaviour of the loss factor during heating for the first five excitation frequencies is quite similar, with the presence of a peak during the martensite to austenite transition. However, for higher pulsations this behaviour is not observed, with increase of the loss factor for martensite and no presence of peaks during transition, while the curves do not show regular patterns as in the lower frequency range. This behaviour could suggest that transient effects effectively generate the peaks during transition. However, above 10 Hz the DMA used experienced some resonance problems. This was because the dynamic stiffness of the head had been designed to test softer materials than the SMA alloy used. While this resonance behaviour does not particularly affect the real part of the complex modulus extracted using Equation 7.1, the phase shift between real and imaginary parts of the mechanical response is influenced. In fact, the loss factor changes significantly even during the full martensite phase, opposite to the stable behaviour showed at excitation frequencies up to 7.74 Hz. This fact suggests that the measurements taken from 11 Hz, especially for the loss

factor, could be prone to experimental error, and should be considered with care.

This study is in line with results from Humbeeck and co-workers [Humbeeck 2003, Humbeeck et.al, 2000]. It has been concluded that shape memory alloys can exhibit a high damping capacity during transformation of the martensite structure when they are in the martensitic state under small harmonic strain loading. Since the internal friction is strongly related to the interaction between defects and interfaces, the damping capacity will strongly depend on the mobility, the distribution and the concentration of those defects and interfaces [Humbeeck and Liu, 2000].

7.2.4 Errors

Although the cooling curve showed in Figure 5.11 features all the characteristics of regularity and smoothness typical of classical viscoelastic testing, the final storage modulus (corresponding to full martensite) is significantly lower compared to the one presented in Figure 5.10, with a decrease of almost 50 %, although the dynamic strain applied was constantly monitored and did not show any sign of clamp slip. At this stage we cannot provide a full satisfactory explanation about this aspect during phase transition. However, the average loss factors at martensite and austenite phase are substantially the same for the two processes, indicating that motions of twin boundaries for the high damping in martensite was still present both after heating and cooling.

7.3   SMA Honeycombs

7.3.1   Static tests

The Cellular Material Theory (Gibson and Ashby, 1997) was used to perform the preliminary design of shape memory alloy honeycombs, in order to understand the change of elastic modulus of SMA cellular structures versus the cell geometric parameters (internal cell angle, wall aspect ratios and relative density) under uniaxial loading. The in-plane Young's moduli and elastic collapse stress are given by the following formulas (Gibson and Ashby, 1997):

$$E^{*}_{Y} = E_{s}\beta^{3}\frac{(\alpha + \sin\theta)}{\cos^{3}\theta}\frac{1}{\left(1 + (2.4 + 1.5v_{s} + \tan^{2}\theta + \left(\frac{2\alpha}{\cos^{2}\theta}\right))\beta^{2}\right)} \qquad ...(7.5)$$

$$\frac{\left(\sigma^{*}_{pl}\right)_{Y}}{\sigma_{ys}} = \beta^{2}\frac{1}{2\cos^{2}\theta} \qquad ...(7.6)$$

Since SMA ribbons exhibits elastic and plastic properties at martensite temperature, the identification of the plastic collapse stress of SMA honeycombs under pseudoplastic and pseudoelastic loading can be performed using Equation 7.6.

The Young's modulus derived from the FE nonlinear simulation and the experimental results are however higher compared to the analytical model and the ones derived from the linear FE analysis. The discrepancy could be

explained not only by the approximations introduced by the numerical boundary conditions imposed, but also by initial slack during the tensile loading given by the specific combination of connecting rod-epoxy frame used for the test rig. It must be also emphasised that the nonlinear FE model was intended to represent the boundary conditions of the experimental model, with degrees of freedom fully clamped and added DOFs with slide conditions, to simulate the complex constraint given by the epoxy resin clamps.

The FE nonlinear simulation follows the experimental results with good accuracy up to a tensile strain of 3%, after which the numerical simulation tends to underestimate the tensile loading behaviour of the honeycomb, with a percentage error of 18% at 5% strain. It is worth noticing, however, that the numerical model describes the increase in tensile stress versus strain well for regular hexagonal honeycomb configurations.

This phenomenon can be explained by a virtual density increase that occurs in convex cellular solids under tensile loading [Gibson and Ashby, 1997]. Figure 7.5a shows the deformation field of the FE nonlinear model corresponding to a tensile strain of 8%. It can be noticed that the honeycomb undergoes a significant deformation, with the ribs away from the edges tending to align towards the loading direction and leading to a strong contraction of the cells (positive Poisson's ratio) which cause a virtual densification under tensile loading.

The opposite happens for a re-entrant honeycomb configuration. Figure 6.9 shows the comparison for static test between the experimental and nonlinear FE model of the auxetic re-entrant SMA cellular solid. The stress-strain curve presents strain hardening-type behaviour, which is consistent to an equivalent increase in density during tensile loading. Figure 7.5b provides a qualitative explanation of this characteristic, showing the displacement field of the re-entrant honeycomb with the same geometric cell characteristics of the one used during the experimental tests at 10 % strain loading conditions. During the deformation, the cell is expected to expand because of the negative Poisson's ratio effect, providing a virtual increase of the overall cross section of the sample during tensile loading, and therefore leading to the decrease of density for the cellular material. At the maximum level of tensile loading imposed, the re-entrant honeycomb tends to assume the shape of a rectangular cell grid work.

| Figure 7.5a Hexagonal Honeycomb | Figure 7.5b Re-entrant Honeycomb |
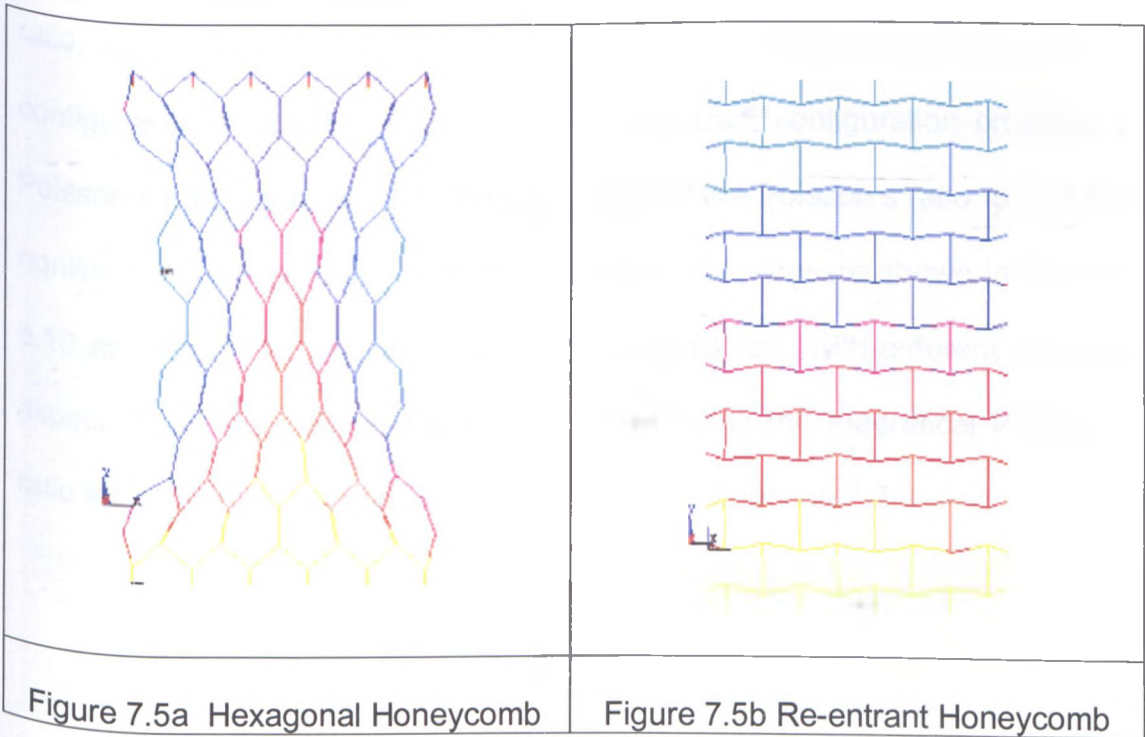
According also to the CMT approach, Equation 7.6 should provide an indication of the first yielding point in the full martensite phase of the honeycomb loading. Assuming a first yield point of 140 MPa (Figure 5.4) for the single ribbon only, the conventional hexagonal configuration would provide a yield stress of 22 kPa (Figure 6.8), while the re-entrant topology would present a yield value of 55 kPa (Figure 6.9). The experimental results provide more conservative results, with values of 16 kPa and 44 kPa for the conventional and re-entrant configurations respectively. However, the FE simulations provide closer results to the analytical ones, with 19 kPa and 48 kPa, leading to percentage errors around 13 % versus the theoretical results for the hexagonal and re-entrant configuration respectively.

7.3.2 Poisson Ratio of Hexagonal and Re-entrant Honeycombs

According to Gibson and Ashby (1997) and Scarpa et.al (2000), the Poisson's ratio v_{xy} within the linear elastic range for the conventional honeycomb configuration is equal to 0.35, while the re-entrant configuration provides a Poisson's ratio value of –2.1. The behaviour of the Poisson's ratio for the full nonlinear behaviour of the martensite phase for α =2 were shown in Figures 6.10 and 6.11. The complete value of Poisson's ratio with different cell wall aspect ratios is shown in Figure 7.8, representing the theoretical Poisson's ratio for centresymmetric honeycombs based on Equation 7.7.

$$v_{yx} = \frac{\sin \theta (\alpha + \sin \theta)}{\cos^2 \theta} \frac{1 + (1.4 + 1.5 v_c) \beta^2}{\left[1 + \left(2.4 + 1.5 v_c + \tan^2 \theta + \frac{2\alpha}{\cos^2 \theta} \right) \beta^2 \right]} \qquad ...(7.7)$$

The 4X4 model has a Poisson's ratio sensibly decreased compared to the infinite honeycomb model from 2-3 % above. However, please note the solution of the Poisson's ratio from CMT for small strains is 1.86. Also for strains between 1 and 2 %, the 4 X 4 model provides a consistent comparison. The increase in magnitude of the Poisson's ratio with increasing tensile strain is expected. The value of the Poisson's ratio for the hexagonal honeycomb is in good agreement with the theoretical calculations.

For re-entrant honeycomb, the CMT approach gives a Poisson's ratio of -0.36. From the experimental, the value of Poisson's ratio shows a negative value up to 9% of strain. Above that value, the Poisson's Ratio has become positive due to the change of cell angle cell become positive [Wu et al, 2004]. At higher level of strain this sample tends to behave as hexagonal honeycomb. The experimental and numerical show a slight different due to the present of small radius at the edge of re-entrant honeycomb sample of SMA as shown in Figure 6.3b. The drastic change of Poisson's ratio to positive indicates that the value of strain in x direction is very small.

According to Wu and co-worker [Wu et al., 2004], Poisson's ratio for the auxetic structure would increase progressively towards zero, and possibly assume positive values for large tensile strains. It has to be noticed also that at 10% tensile strain, the auxetic honeycomb already approached values typical of the rectangular grid topology, which corresponds to pure axial deformation behaviour of the ribs and zero Poisson's ratio [Gibson and Ashby,

1997], as shown in Figure 7.5b. Also, the reduced size of the samples would amplify Saint-Venant effects from the boundaries, and not represent correctly the "infinite honeycomb" conditions that are used to determine the Poisson's ratio effects on cellular solids [Silva et al, 1995; Scarpa et al., 2000].
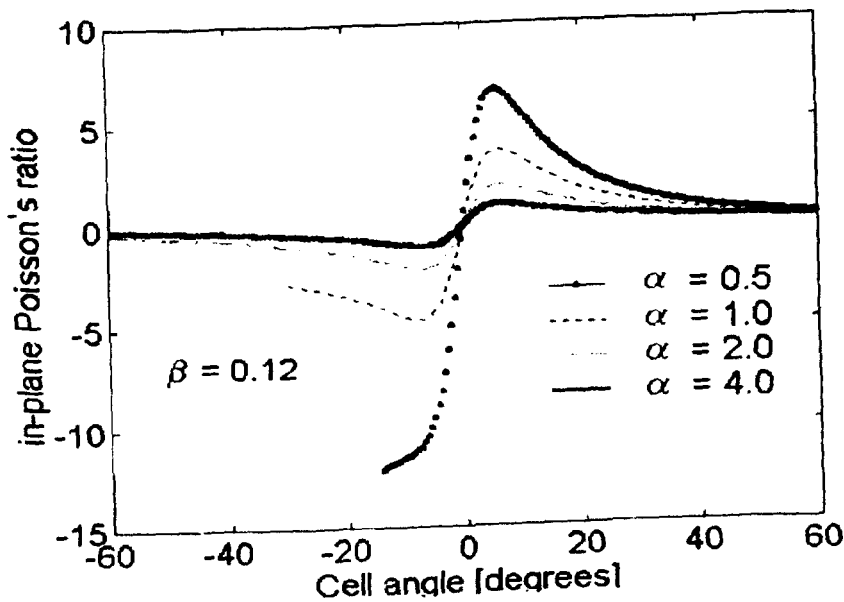
Figure 7.6   In plane theoretical Poisson's ratio [Scarpa et.al, 2000]

According to the study by Wan et al.(2004) on Poisson's ratios in auxetic honeycombs based on large deflection, it can be concluded that, the magnitude of Poisson's ratio decreases significantly at high strain when the re-entrant centresymmetric honeycomb is compressed in the X direction loading or stretched in the Y direction, while it increases significantly at high strain when the re-entrant honeycomb is stretched in the X direction loading of is compressed in the Y direction. The reason for re-entrant honeycombs to exhibit a substantial nonlinearity is due to the changes in the angles between

the structural elements, which governs the Poisson's ratio for the structure [Prall & Lakes,1997].

(a)   (b)
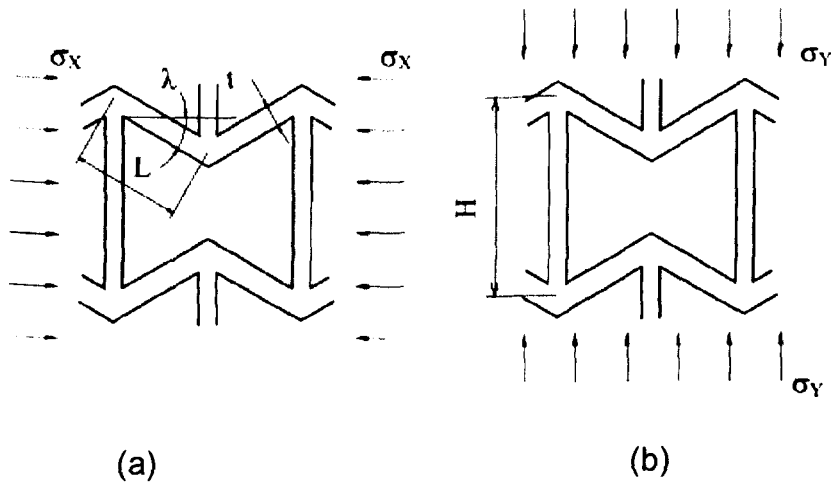
Figure 7.7, Re-entrant Honeycomb Under compressive loading;
(a) X loading (b) Y Loading [Wu et al, 2004]
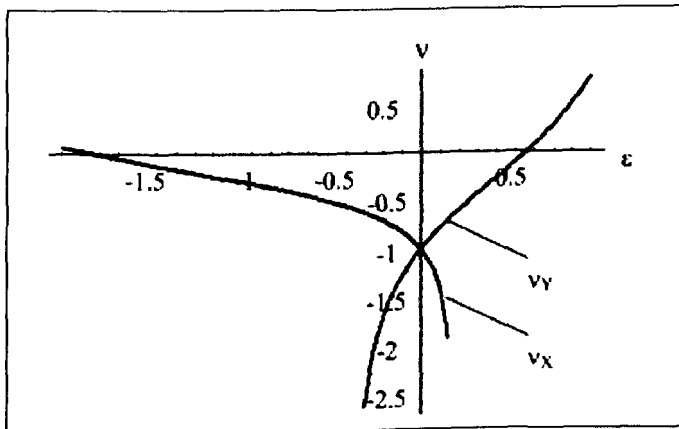
Figure 7.8   Poisson's ratios vary with strain for re-entrant Honeycomb cell
[Wu et al, 2004]

7.3.3 Poisson ratio of chiral honeycomb

The compression test for the chiral honeycomb has to be done at austenite phase temperature because the modelling of Poisson's ratio for the SMA chiral honeycomb was based on pseudoelastic behaviour. Recalling that it is possible to induce phase transformation by pure mechanical loading in SMA components [Gandhi & Wolons, 1999] in the austenite phase, one can assume that the SMA chiral honeycomb would behave in a linear elastic regime when subjected to compression loading.

The stress-induced phase transformation is therefore an important aspect to be considered when investigating the Poisson's ratio behaviour. When the test is performed in the austenite phase, the results can be used to derive values for the in-plane Poisson's ratio that can be compared with the analytical results from Prall & Lakes (1997). It was assumed, in the austenite phase, that the SMA chiral honeycomb was undergoing elastic behaviour.

The FE model, made by 2D plane strain elements, would consider also axial and shear deformation of the ligaments. Additional departures from the pure bending model would be provided by the cylinders. Although they were modelled using a very stiff material (steel), some marginal flexibility could still be achieved. Please noted, in order to obtain node displacement similar to the experimental, in the FE modelling, the unit cell was constrained at the mid way of centre ligament. The direction of loading to the chiral honeycomb models is shown in Figures 7.9 and 7.10.
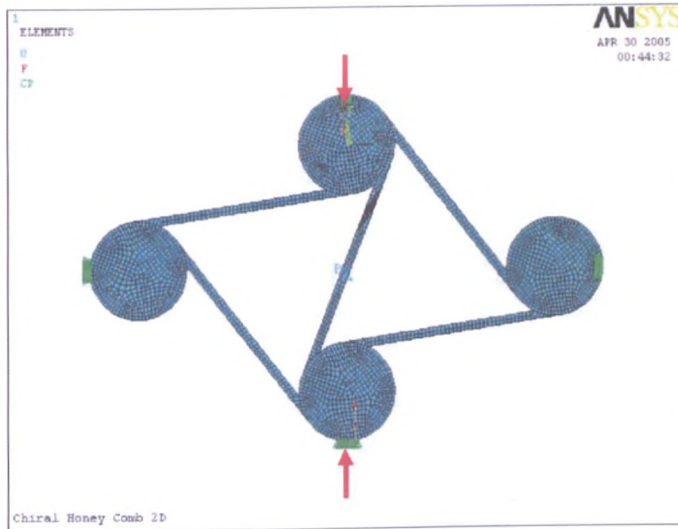
Figure 7.9 Compression loading of a Unit Cell Compression in the Y direction
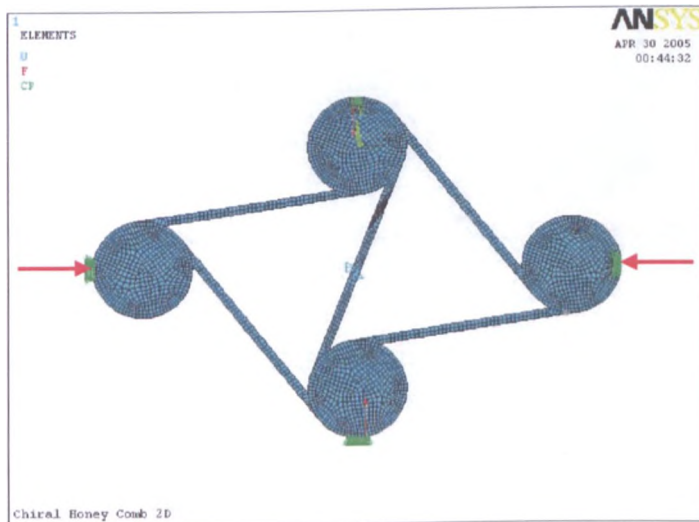
Figure 7.10 Compression loading of a Unit Cell in the X direction

Figure 7.11 shows the deformation of the FE unit cell under compressive loading along the Y-direction. After compression it is observed that the ligaments bend and wind in to the node, which was one of the deformation mechanisms giving rise to the negative Poisson's ratio effect.

From Figure 7.11 it is possible to obtain the displacement of the structure along the x and y directions. Nodes 1 and 2 give the displacement value for

the unit cell in the X direction, while nodes 3 and 4 give the displacement value along the Y direction. The actual length of the structure along the two perpendicular directions provides the strain values for ε_x and ε_y, obtained by dividing the displacements by the lengths of the cell.
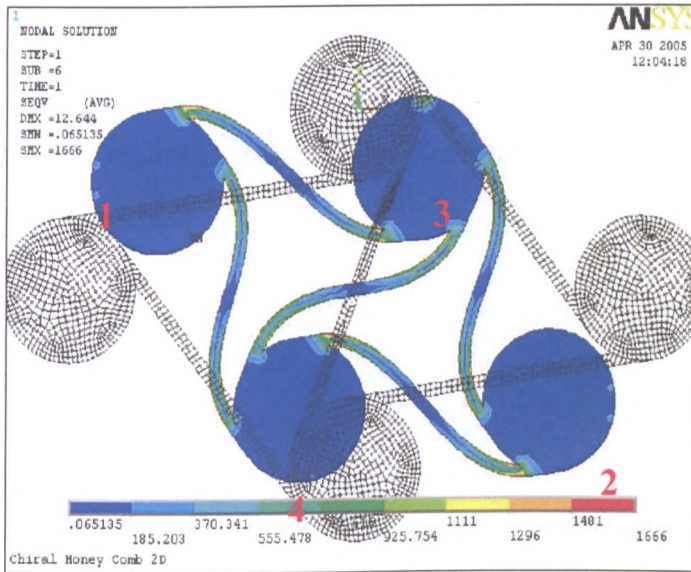
Figure 7.11 Deformed Unit Cell due to compression in the Y direction

The Poisson's ratio along the Y direction shown in Figure 6.12 has revealed some similarity to the behaviour of the experimental results obtained by Prall and Lakes. The Poisson's ratio shows constancy in a value close to -1.

One can suggest, therefore, that the Poisson's ratio of the chiral honeycomb is independent of strain, at least for quasi-static loading. Observing the results from this analysis, it is evident that the integration of shape memory alloys as core ligament material for the structure does not effect the negative Poisson's ratio characteristics of the structure.

The Poisson's ratio of the honeycomb is a function of the deformation mechanism of the honeycomb – the loading considered is nonlinear geometric elastic, but the elasticity of the material is constant. The geometry of the hexagonal chiral honeycomb panel also plays a certain effect upon the Poisson's ratio, with a reduction of the magnitude of the in-plane Poisson's ratio for a decrease in number of cells available. However, it is apparent that the Poisson's ratio is strain independent for quasistatic loading, because the structure shows constancy in the value of the Poisson's ratio even at higher or lower strain values.

7.3.4 Analysis of errors

As for the values of the Poisson's ratio for the centresymmetric SMA honeycomb (Figure 6.10 and 6.11), the limited number of cells available in our samples conditioned the final Poisson's ratio results. A higher number of cells of chiral honeycomb would provide experimental results closer to the values of −1. The tests confirm also the constancy of the Poisson's ratio value over a significant range of tensile strain. This is considered as unusual and differs from the behaviour of other materials and structures that also depicts the negative Poisson's ratio effect, such as re-entrant centresymmetric honeycombs.

For chiral honeycomb, some ligaments are not exactly tangential to the cylinders, and could have a small radius of curvature near the node implying a stiffening effect and therefore a decrease of the deformations due to pure

bending. Probably, some ligaments are not completely straight as well, and that induces further curvature effects.

Based on this work, the unit cell for hexagonal chiral honeycomb model which was suggested by Prall & Lakes (1996) as in Figure 3.7 is not appropriate to represent an infinite SMA honeycomb. This might be the main reason to the discrepancies between FE and experimental result. The 3 and 4 ligaments for each node are not suitable to represent the 6 ligaments at each node. Therefore, a new way of modelling unit cell with 6 nodes for each node as shown in Figure 7.12, would expect to give more accurate result.
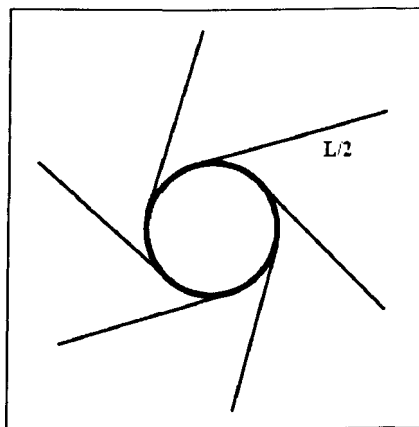
Figure 7.12   Proposed new unit cell for chiral honeycomb modelling

In term of shear effect, the experimental sample rotates during uniaxial loading. The type of clamps used tends to impede this shear deformation, and therefore stiffening with decrease of Poisson's ratio effects occurs. This is a consequence of the Saint Venant effect due to the experimental clamps conditions, while the FE unit cell model is prevented from these Saint Venant mechanisms. The detail explanation of the effect on negative Poisson's ratio material has been explained by Lakes [Lakes, 1992].

Chapter 8

CONCLUSIONS AND RECOMMENDATIONS

8.1 Conclusions

A number of important conclusions can be drawn from the work reported in this thesis. These are given in the following section.

8.1.1 SMA ribbon

Modelling the SMA as a two dimensional structure was among the crucial activities related to the application of SMAs to define new cellular structures. Common practice is to use wire models in their applications since it is relatively easy to simulate one-dimensional structures. Very few attempts have been made to use two dimensional structures such as ribbon due to the complexity of the micromechanical modelling involved.

In this work, an effort to provide a simplified modelling of SMA ribbon using a commercial finite element package had been performed. The numerical simulations performed in the martensite region provided good agreement with the experimental values. This fact suggests that the approach taken could be

a viable option for further developments of SMA components in more complex structures.

8.1.2 SMA as a damping material

SMA are known to give useful levels of damping when subjected to strain. In this work small amplitude dynamic tests have been performed on a NiTiCu ribbon to extract characteristics for broadband low amplitude damping applications. Test were conducted for excitation up to 60 Hz for heating and cooling between 10°C and 150°C. Storage modulus and loss factors measured using DMA equipment properties did not show frequency dependence at low frequency, while changes in stiffness between martensite and austenite were similar to the ones recorded during quasistatic tests. Loss factors around 3% were measured for martensite while for austenite loss factor levels were much lower and similar to normal metals.

8.1.3 SMA Honeycombs

Tensile properties of a novel class of honeycomb structures made of shape memory alloy have been investigated. The cellular solids have been tested with the core material being in full the martensite phase for an initial assessment of their basic properties. Linear and nonlinear finite element models have been developed to simulate the strain hardening-type behaviour of the honeycomb ribbon and the full tensile loading simulation on the cellular solids. The use of the equations from the Cellular Material Theory to identify

the linear elastic part and the first yielding stress point of the honeycombs in full martensite phase has been discussed and validated with the numerical and experimental results.

The conventional and negative Poisson's ratio SMA honeycombs exhibited equivalent density variations according to their topological layout during tensile loading. Adaptive materials such as shape memory alloys (SMAs) suggest new opportunities for the design of multifunctional structures and components for aerospace structures. The combinations of SMA and auxetic technology have been proposed for the first time in this work. The use of SMA as a core honeycomb could improve the structural integrity of the panel because of the enhanced fatigue properties of NiTiCu alloys (Psarras et.al, 2001), increased damping capabilities compared to classical commercial honeycombs made out of 2024 aluminium core, and also can be considered as an active morphing structure. The results of this work provide an initial assessment of the in-plane properties.

8.1.4 SMA Chiral honeycomb

This work has also analysed the effect of applying shape memory alloy material as a ligament for a chiral honeycomb structure. From the series of analysis carried out in studying the behaviour of the chiral honeycomb structure with the SMA ligaments, a few interesting results have been obtained.

The Poisson's ratio for the structure seems to comply with the experimental findings from Lakes et al. Upon compression loading the Poisson's ratio, has been found close to the theoretical value of -1. The departures from the theoretical value are to be attributed to the contribution of the axial deformation of the ligaments, in a similar manner as recorded in centresymmetric honeycomb structures. This fact is truly interesting, as other auxetic structures such as re-entrant honeycombs show a sort of nonlinearity in the Poisson's ratio upon both compression and tension loading.

This new cellular structure with shape memory alloy as core material could be attractive as a new platform for sandwich material. The memory effect that the shape memory alloy has could find applications in designing self deployable structures for aerospace applications, such as satellite antennas. It could be therefore possible to have a structure with mechanical strength characteristic of metal alloys and "smart" capabilities to deploy and retract, bringing hopefully an interesting contribution to the field of aerospace structural designs.

Chiral honeycombs made from shape memory alloys can also offer other significant advantages. The structure can be self-deployable when subjected to phase transformation of the material forming its structure. In Figure 8.1, the chiral honeycomb was made from SMA and was acting based on temperature induce transformation. It was design in such a way to make it easy to fabricate in a large cell. The ligaments of chiral honeycomb can wind into the cylinder in the martensite phase. This setup makes the honeycomb very compact and

occupies a small space. As shown in the picture, when subjected to heat flux and deployed, the area of the honeycomb can increase up to 100%.
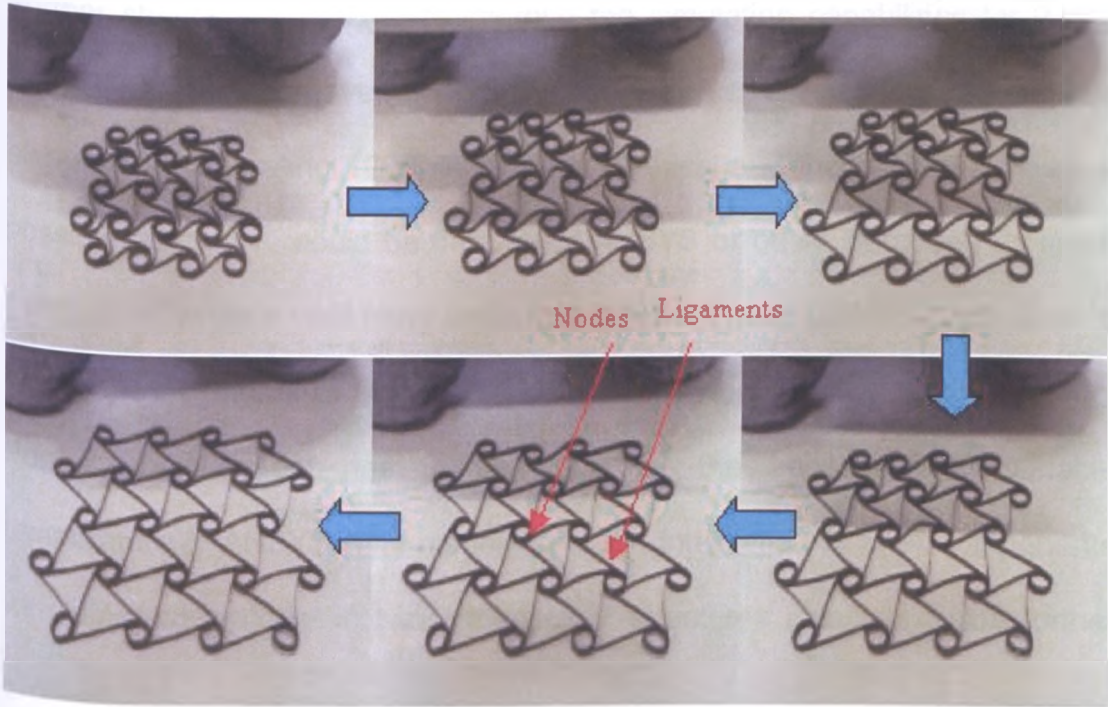
Figure 8.1 Self deploying mechanism of the chiral honeycomb structure using SMA

8.2 Recommendations and future works

8.2.1 Modelling

Further studies are needed to improve the simulation capabilities for 2-way SMA behaviour. Moreover, it would be ideal for cellular solids to have beam elements incorporating 1D SMA micromechanical and thermal capabilities. A possible alternative could be the use of ANSYS or other FE codes as mesh generators, while a third party code (MATLAB, for example) could be used to create the FE model of the whole honeycomb under uniaxial tensile loading. Further development has to be done for the application at variable temperature in ANSYS. The modelling of the integration of SMA components with different material in two dimensional structures also has to be further investigated.

8.2.2 SMA damping

The storage modulus peaks present during transition were recorded during the whole frequency sweep test. However, the results related to the loss modulus are not conclusive, because of the irregularities given by resonance of the test equipment used above 10 Hz. Further analysis is needed to improve the testing at higher frequency ranges, to improve the assessment of SMA ribbons to enhance possible implementations in broadband white noise excitation applications.

8.2.3 SMA Honeycomb

There is the need for further studies on SMA honeycomb, such as the control of the temperature for the SMA ribbon for active shaping of the honeycomb. Future studies should be also focused on the analysis of the pseudoelastic behaviour of the cellular structures, and on defining more sophisticated analytical models to describe the SMA-related behaviour of these novel structures. In order to complete the assessment for classical sandwich panel architectures, investigations on the out-of-plane mechanical properties, both considering one-way and two-ways SMA behaviour are also needed.

8.2.4 Future deployable antenna

A shape memory alloy auxetic honeycomb could be used for future deployable antennas in satellite applications. Double (synclastic) curvature typical of auxetics allows producing a dome shaped structure. However, for deployable antennas applications, the surrounding temperature is a major concern. The space temperature is constant at 2.7 Kelvin, corresponding to the 3 degree microwave background radiation. However, the parts of a satellite exposed to sunlight can become extremely hot , and only radiation dissipation is the mechanism for cooling the components.

For this application, we are essentially looking at one-way shape memory effect. It is very difficult to get the SMA in the austenite region in a space environment, with SMA components normally available with transformation temperature in the range between -100° to +100° Celsius. Therefore, in the average space environment the SMA will be in the full martensite region. To

127

achieve deployable capabilities for the SMA honeycomb, special mechanism embedding heat sources have to be introduced. Some parts of the honeycomb have to be heated up to transformation temperature to deploy the antenna and achieve the double curvature of the honeycomb. Specific studies related to heat transfer for SMA honeycomb concepts have to be performed to assess possible applications in this field, together with analysis on the structural integrity of the structure against microdebris and impacts from particles and meteorites.

8.2.5 Other Potential Applications

SMA honeycombs could potentially provide other applications. SMA auxetic honeycombs could be proposed as high performance impact absorbing structures. The pseudoelasticity of SMA would provide the structure with high strain energy storing and restoring shape capabilities. This characteristic is very important in packaging and also for crashworthiness applications. Since SMAs have been identified as good materials for damping, sandwich structures made from SMA honeycomb cores have great potential in vibration damping applications.

Other suggestions for future work include the integration of other smart material such as shape memory polymers for further studies on smart sandwich structures. Shape memory polymers can be used as the top and bottom skins for sandwich structures with the SMA or other smart honeycomb cores. With this type of sandwich configuration, it is conceivable that the overall surface of the structural component could be deformed controlling the temperature.

REFERENCES

Abel, E., Luo, H., Pridham, M., Slade, M., 2004, Issues Concerning the Measurement of Transformation Temperatures of NiTi alloys Smart Mater. Struct. 13 1110-1117

Allen, H.G. 1969, Analysis and Design of Structural Sandwich Panels. Pergamon Press, Oxford

Amalraj, J. J., Bhattacharyya, A. and Faulkner, M. G., 2000, Finite-Element Modeling of Phase Transformation in Shape- Memory Alloy Wires with Variable Material Properties Smart Mater. Struct. 9 622-631

Anderson, A., 1999, A triumph of lateral though, Chemistry & Industry, 17 May 1999, pp 384-391.

Auricchio, F., Sacco, E., 1997, A 1D model for Superelastic Shape-Memory Alloys with Different Elastic Properties Between Austenite and Martensite J. Non-linear Mech, 32(6), 1101-1114

Ayuela, A., Enkovaara, J. and Nieminen, R. M., 2002, Ab-initio Study of Tetragonal Variants in Ni_2MnGa Alloy. Journal of Physics: Condensed Matter 14, pages 5325-5336. © 2002 Institute of Physics Publishing Ltd.

Barras C.D., Myers, K.A. ,2000, Nitinol: its use in vascular surgery and other applications, Eur J Vasc Endovasc Surg, 19, pg. 564-569.

Biscarini, A., Coluzzi, B., Mazzolai, G., Tuissi, A. and Mazzolai, F., 2003, Extraordinary High Damping of Hydrogen-Doped NiTi and NiTiCu Shape Memory Alloys, J. Alloys Comp., 355, pp. 52-57.

Boyd, J. G. and Lagoudas, D. C., 1996, A Thermodynamical Constitutive Model for Shape Memory Materials Part I: The Monolithic Shape Memory Alloy Int. J. Plasticity 12 805-42

Brinson, L.C., Schmidt, I., Lammering, R., Micro and Macromechanical Investigations of CuAlNi Single Crystal and CuAlMnZn Polycrystalline Shape Memory Alloys, Journal of Intelligent Material Systems & Structures, 13 (12): pp. 761-772 (2002).

Brinson, L.C., Schmidt, I., Lammering, R., Micro and Macromechanical Investigations of Transformation Behavior of a Polycrystalline NiTi Shape Memory Alloy Using in situ Optical Microscopy, J. Mechanics and Physics of Solids, vol. 52:7, pp. 1549-1571 (2004).

Bubner, N., 1996, Landau-Ginzburg, Model for a Deformation-Driven Experiment on Shape-Memory Alloys, Continuum Mechanic and Thermodynamic, Volume 8, Number 5, pp.293 - 308

Buehler, W.J., Wang, F.E., (1968), A Summary of Recent Research on the Nitinol Alloys and Their Potential Application in Ocean Engineering. Ocean Eng 1: 105-120.

Buehler,W.J., Gilftrich, J.V. & Wiley, R.C., 1963, Ams.I. Physic. Vol 34 ms.1475

Bullough, W. A., Johnson, A. R., Hosseini-Sianaki, A., Makin, J. and Firoozian, R., 1993, Electro-Rheological Clutch: Design, Performance Characteristics and Operation, Proceedings of the Institution of Mechanical Engineers, Part I, Journal of Systems and Control Engineering, Vol. 207, No. 2, pp. 87-95.

Caddock, B. D., and Evans, K. E., 1989, Microporous Materials with Negative Poisson's Ratio: I. Microstructure and Mechanical Properties J. Phys. D., Appl. Phys.,. 22, 1877-1882

Caddock, B. D., Evans, K. E., Masters, I. G., 1991, Honeycomb with Negative Poisson Ratio for Use in the Composite Sandwich Panels, preceeding of ICCM/8, Honolulu, section 1-11,3-E

Cingolani E., Humbeeck J.V., Ahlers, M., 1999, Stabilization and Two-Way Shape Memory Effect in Cu-Al-Ni Single Crystals Metallurgical and Materials Transactions A1, March 1999, vol. 30, no. 3, pp. 493-499(7)

Crone, W. C., Wu, D. and Perepezko, J. H., Pseudoelastic Behavior of Nickel–Titanium Melt-Spun Ribbon, Materials Science and Engineering A, Volumes 375-377, 15 July 2004, Pages 1177-1181

Cross, W.B., Kariotis, A.H., Stimler, F.J., 1969, Nitinol Characterization Study, NASA CR-1433

Culshaw, Gardiner & Mc Donach, 1992, First European Conference on Smart Structures and Material .Bristol : Institute of Physics Publishing.

Culshaw, B., 1996, Smart Structure and Material. Norwood : Artech House

Davies, G.(Chairman), 2004, Smart material for the 21st Century, Material Foresight, IOM3 publication, London

Dimier, F., Vergnes, B., Vincent, M., 2004, Relationships between mastication conditions and rheological behavior of a natural rubber, Rheologica Acta, Volume 43, Issue 2, , Pages 196 - 202

Duclos, T., Carlson, J., Chrzan, M. and Coulter, J. P., 1992, Electrorheological Fluids – Materials and Applications, in Intelligent Structural Systems, Tzou

and Anderson (editors), Kluwer Academic Publishers, pp. 213-241, Netherlands

El-Sayed, A, F.K., Jones, R. and Burgess, I.W., 1979, A Theoretical Approach to the Deformation of Honeycomb Based Composite Materials. Composites 10, pp. 209–214.

Enkovaara, J., Ayuela, A., Nordström, L. and Nieminen, R. M., 2002, Structural, Thermal and Magnetic Properties of Ni_2MnGa. Journal of Applied Physics 91, No. 10, pages 7798-7800. © 2002 American Institute of Physics

Evans, K. E., Alderson,A., 2000, Auxetic Materials: Functional Materials and Structures from Lateral Thinking, Advanced Materials , Volume 12, Issue 9 , Pages 617 – 628

Evans, K. E., Design of Doubly Curved Sandwich Panels with Honeycomb cores.Computers & Structures 17 (1991), pp. 95–111

Evans, K. E., Nkansah, M.A., Hutchinson, I. J. and S.C. Rogers, S. C., 1991, Molecular network design, Nature Vol. 353, p. 124

Evans, K.E., Donoghue, J.P., Alderson, K.L., 2004, The Design, Matching and Manufacture of Auxetic Carbon Fibre Laminates, Journal of Composite Materials, January 2004, vol. 38, no. 2, pp. 95-106(12)

Falk, F., 1983, One Dimensional Model of Shape Memory Alloys. Arch. Mech. Vol 35. ms.63-84.

Florin Andrei Nae, Yuji Matsuzaki and Tadashige Ikeda , 2003, Micromechanical Modeling of Polycrystalline Shape-Memory Alloys Including Thermo-Mechanical Coupling, 2003 Smart Mater. Struct. 12 6-17

Fu,Y.Q., Luo,J.K., Hu,M., Du,H.J.,FlewittA.J., Milne,W.I., 2005, Micromirror structure actuated by TiNi shape memory thin films J. Micromech. Microeng. 15 1872-1877

Fukada, E., Yasuda, J., Jpn J. Appl. Phys. No. 3 (1964) p. 117

Gandhi, F. and Chapuis, G., 2002, Passive Damping Augmentation of a Vibrating Beam using Pseudoelastic Shape Memory Alloy Wires Journal of Sound and Vibration, Volume 250, Issue 3, Pages 519-539

Gandhi, F. and Wolons, D., 1999, Characterization of the pseudoelastic damping behavior of shape memory alloy wires using complex modulus, Smart material and structure Volume 8, Number 1, February 1999

Gandhi, M. V. and Thompson, B. S., Smart Materials and Structures, Chapman & Hall, London ,1992.

Gibson, L. J. and Ashby, M. F., Cellular solids : Structure and Properties, Cambridge University Press, Cambridge 1982.

131

Gibson, L. J. and Ashby, M. F., Cellular solids : Structure and Properties,2nd Edition, Cambridge University Press, Cambridge   1997.

Gibson, L.J., Ashby, M.F., Schajer,G.S., Robertson,C.I., 1982,The Mechanics of Two-Dimensional Cellular Materials ,Proceedings of The Royal Society of London. Series A, Mathematical and Physical Sciences, Volume 382, Issue 1782, pp. 25-42

Gil, F. J., Planell, J. A., 1999, Effect of Copper Addition on the Superelastic Behavior of Ni-Ti Shape Memory Alloys for Orthodontic Applications Journal of Biomedical Materials ResearchVolume 48, Issue 5, Pages:682-688
Glieck, J., 1987,The New York Times, 14 April 1987.

Grima, J.N., Jackson,R., Alderson, A. and Evans, K.E.,2000, Adv. Mater. Vol. 12(24), 1912.

Hamamoto, N., Hashimoto, Y., Sakasai, M., Tsuchihashi, Y., Yoneda, M.,1998, An Experimental Multimedia Mobile Satellite Communication System Using the ETS-VIII Satellite, AIAA International Communications Satellite Systems Conference and Exhibit, 17th, Yokohama, Japan, pp. 408-416.

Heydt, R., Pelrine, R., Joseph, J., Eckerle, R., 2000, Acoustical Performance of an Electrostrictive Polymer Film Loudspeaker, The Journal of the Acoustical Society of America , Volume 107, Issue 2, pp. 833-839

Hexcell Corp. , 2005, http://www.hexcel.com/About/Our+Business/ Fabrics/

Hodgson, D.E., Using Shape Memory Alloys, Shape Memory Applications, 1988

Howard, G., Shield T.W. Orientation Dependence of the Pseudoelastic Response of Cu-Al-Ni in Tension, The Journal of the Mechanics and Physics of Solids, 43(6), 1995, pp. 869-895.

Hu, L., Chen, Z.M., Qian, C.L and Zhou, L.W., 2003, Viscoelasticity of Compressed Granular Assembly, International Journal of Modern Physics B, Vol. 17, Nos. 1 & 2 (2003) 217–220

Humbeeck, J., 1996, Damping Properties of Shape Memory Alloys During Phase Transformation, Journal de Physique IV, Volume 6, Issue 8 , 1996, Pages 371-380

Humbeeck, J., 1999, Non-Medical Applications of Shape Memory Alloys Materials Science and Engineering A, Volumes 273-275, 15, Pages 134-148

Humbeeck, J., 2003, Damping Capacity of Thermoelastic Martensite in Shape Memory Alloys. Journal of Alloys and Compounds 355:1 pp. 58-64

Humbeeck, J., Liu, Y., 2000, Shape Memory Alloys as Damping Materials Materials Science Forum (Switzerland). Vol. 327-328, pp. 331-338

Hutzler, S., Weaire, D.,1997, Buckling Properties of 2D Regular Elastomeric Honeycombs Journal of Physics: Condensed Matter, vol. 9, no. 22, pp. L323-L329(1)

James, R. D., and Wuttig, M., Magnetostriction of Martensite, Philosophical Magazine, 77A (1998), 1273-1299.

Jenner, A.G., Wilkinson, A.W. & Greenough, R.D., 1995, Actuation and Control by Giant Magnetostriction, Innovative Actuators for Mechatronic Systems, IEE Colloquium , 18 Oct 1995,pp 4/1-4/3

Jones, B., Chen Liang, 1996, Magnetostriction: Revealing the Unknown Aerospace and Electronic Systems Magazine, Volume 11, Issue: 3, pp 3-6
Jones, D. I., 2002, Handbook of Viscoelastic Vibration Damping. John Wiley & Sons, Ltd, Chichester, UK.

Jonnalagadda, K. D., Sottos, N. R., Qidwai, M. A. and Lagoudas, D. C., In situ Displacement Measurements and Numerical Predictions of Embedded SMA Transformation, Smart Mater and Struct. 9 No 5 (October 2000) 701-710

Jonnalagadda, K. D., Sottos, N. R., Qidwai, M. A. and Lagoudas, D. C., 1998, Transformation of embedded shape memory alloys J. Intell. Mater. Syst. Struct. 9 379-90

Kahn, H., Huff, M., Heuer, A. H., 1998, The TiNi Shape-Memory Alloy and its Applications for MEMS, Journal of Micromechanics and Microengineering, 8, 213-2211998

Kakeshita, T., Shimizu, K., Funada, S. and Date, M., Magnetic Field-Induced Martensitic Transformations In Disordered and Ordered Fe-Pt Alloys, Transactions of Japan Insitute of Metals, 25 (1984), 837-844.

Kawai, H., The Piezoelectricity of Polyvinylidene Fluoride, Japan. J. Appl. Phys. , Vol. 8, (1969) pp. 975-976.

Kim, H., Miyazaki,S., 2004, Martensitic transformation behavior in Ni–Al and Ni–Al–Re Melt-Spun Ribbons, Scripta Materialia, Volume 50, Issue 2, Pages 237-241

Kulkarni, Ravi, Bellamy, Elizabeth, 2001,Nickel-Titanium Shape Memory Alloy Memokath 051 Ureteral Stent for Managing Long-term Ureteral Obstruction: 4-year experience. Journal of Urology. 166(5):1750-1754

Lakes, R.S., 1992, Saint-Venant end effects for materials with negative Poisson's ratios, J. Applied Mechanics, Vol 59, pp 744-746.

Lakes, R. S., 1993, Advances in negative Poisson's ratio materials, Advanced Materials (Weinheim, Germany), 5, 293-296, 1993.

Lakes, R. S., 1999, Viscoelastic Solids. CRC Press, London.

Larsen, U. D., Sigmund, O. and Bouwstra, S., 1997. Design and fabrication of compliant mechanisms and structures with negative Poisson's ratio. Journal of Microelectronic Systems, 1997, 6(2), 99-106

Lee, J. H., Choi, J. B. and Choi, K., Journal of Materials Science 31, 1996, 4105)

Lew, T.L., Spadoni, A. Scarpa,F., Ruzzene,M., 2005, Chiral hexagonal cellular sandwich structure: a vibro-acoustic assessment, Proceedings of SPIE -- Volume 5760, Smart Structures and Materials 2005: Damping and Isolation, pp. 559-568

Li, X., 2004, Integration of GPS, Accelerometers and Optical Fiber Sensors for Structural Deformation Monitoring. 17th Int. Tech. Meeting of the Satellite Division of the U.S. Institute of Navigation, Long Beach, California, 21-24 September, 211-224.

Lim, T.C., 2003. Constitutive relationship of a material with unconventional Poisson's ratio. Journal of Materials Science Letters, 22, pp 1783-1786).

Lines, M. E. and Glass, A.M., Principles and Applications of Ferroelectric Related Materials, Clarendon Press, Oxford, (1977).

Lu, X. L., Cai, W. and Zhao, L. C., 2003, Damping Behaviour of a $Ti_{44}Ni_{47}Nb_9$ Shape Memory Alloy, J. Mat. Sci. Lett., 22, pp. 1243-1245.

MacCraith, B.D., McDonagh, C., McEvoy, A.K.,1997, Optical Chemical Sensors Based on Sol-Gel Materials: Recent Advances and Critical Issues, Journal of Sol-Gel Science and Technology ,Volume 8, Numbers 1-3, pp.1053 - 1061

Masters, I. G. and Evans, K. E., 1996, Model foe Elastic Deformation of Honeycombs, Composite Structures, vol 35, pp. 403-422.

Miller, D.A. and Lagoudas, D.C., 2000, Thermo-Mechanical Characterization of NiTiCu and NiTi SMA Actuators: Influence of Plastic Strains, Smart Materials and Structures, Vol. 9, No. 5, pp. 640-652

Milton, G., 1992, Composite Materials with Poisson's Ratios Close to -1, J. Mech. Phys. Solids, 40, 1105-1137

Mitchell, P.F., 2003, Development of Advanced Actuation Concepts to Provide a Step Change in Technology Used in Future Aero engine Control System, Technical Report, ADVACT-STREP PartB, , Rolls-Royces plc, Julai 2003.

Newnham, R.E., Amin, A., 1999, Smart systems : Microphones, Fish Farming, and Beyond, Chemtech, Volume 29, No. 12, 38-46.

Oberaigner, F.R., Tanaka, K. and Fischer, F. D., 1996, Investigation of the Damping Behavior of a Vibrating Shape Memory Alloy Rod using a Micromechanical Model Smart Mater. Struct.3 456-63

Oh, K., Furuta, A., Uchino, K., 1990, Field Induced Strain in Antiferroelectrics, IEEE Ultrasonic Symposium, pp. 743-746.

Oikawa, K., Wulff, L., Iijima, T., Gejima, G., Ohmori, T., Fujita, A., Fukamichi, K., Kainuma, R. and Ishida, K., Promissing Ferromagnetic Ni-Co-Al Shape Memory Alloy System, Applied Physics Letters, 81 (2001), 3290-3292.

Okada, R. and Kortschot, M.T., The role of the resin fillet in the delamination of honeycomb sandwich structures. Composites Science and Technology, 2002. 62(14): p. 1811-1819.

Ota, S., Radiation Physics Chemistry, 1981, 18(1–2), 81– 87.
Papka, S., Kyriakides, S., 1994, In-Plane Compressive Response and Crushing of Honeycomb. J. Mech. Phys. Solids 42, pp. 1499–1532.

Perkins, J., Hodgson, D., 1990, The Two Way Shape Memory Effect, in Engineering Aspect of Shape Memory Alloys. Edited by Duerig. T.W., Melton. K.N., Stöckel. D. & Wayman. C.M. Butterworth-Heinemann. pp. 195-206

Piedboeuf, M. C. and Gauvin, R., 1998, Damping Behaviour of Shape Memory Alloys: Strain Amplitude, Frequency and Temperature Effects, J. Sound Vib., 214(5), pp. 885-901.

Pilling, John., 2005, Mechanics of Honeycombs, electronic version of Composite Materials (MY4150), http://www.mse.mtu.edu/~drjohn//my4150/

Prall, D., Lakes, R., 1997, Properties of a Chiral Honeycomb with a Poisson's Ratio -1, Int. J. of Mechanical Sciences, 39, 305-314.

Predki, W., Knopik, A., Klönne, M., 2004, Damping Factors and Fatigue Notch Factors of Pseudoelastic NiTi-Shape Memory Alloys Materialwissenschaft und Werkstofftechnik Volume 35, Issue 5, 307-312

Psarras, G.C., Parthenios, J. and Galiotis, C., Adaptive composites incorporating shape memory alloy wires; Part 1: probing the internal stress and temperature distributions with a laser Raman sensor, Journal of Material Science, 36, 1-12, 2001

Qidwai, M.A., and Lagoudas, D.C., 2000, Numerical implementation of a shape memory alloy thermomechanical constitutive model using return mapping algorithms , Int. J. Numer. Meth. Eng, vol. 47, pp. 1123-1168

Rey, N., Gregory Tillman, Robin, M., Miller, Thomas Wynosky, Michael J. Larkin, Jeffrey, D., Flamm, Linda, S., Bangert, 2001, Shape Memory Alloys for a Variable Fan Nozzle, Proc. SPIE Vol. 4332, p. 371-382

Richter, L., Zipser, L., Lange, U., 2001, Properties of Magnetorheologic Fluids. Sensors and Materials. Vol. 13, no. 7, pp. 385-397.

Ruzzene, M. and Scarpa, F., Control of Wave Propagation in Sandwich Beams with Auxetic Core, Journal of Intelligent Materials Systems and Structures, July 2003, vol. 14, no. 7, pp. 443-453(11)

Ruzzene, M., Mazzarella, L., Tsopelas, P., Scarpa, F., Wave Propagation in Sandwich Plates with Periodic Auxetic Core, Journal of Intelligent Materials Systems and Structures, 1 September 2002, vol. 13, no. 9, pp. 587-597(11)

Ryhanen, J., 1999, Biocompatibility evaluation of nickel-titanium shape memory metal alloy, Academic Dissertation Faculty of Medicine, University of Oulu

Saadat, S., Noori, M., Davoodi, H., Hou, Z., Suzuki, Y. and Masuda, A., 2001, Using NiTi SMA Tendons for Vibration Control of Coastal Structures, Smart Mater. Struct. Vol.10 No 4, 695-704

Scarpa, F, Smith, F.C., Chambers, B., Burriesci, G., 2003, Mechanical and Electromagnetic Behaviour of Auxetic Honeycomb Structures, Aeronautical Journal, Volume 107, Number 1069

Scarpa, F. and Tomlinson, G., 2000, Theoretical Characteristics of the Vibration of Sandwich Plates with In-plane Negative Poisson's Ratio Values, Journal of Sound and Vibration, Volume 230, Issue 1, Pages 45-67

Scarpa, F., Panayiotou, P. and Tomlinson, G., 2000, Numerical and Experimental Uniaxial Loading on In-Plane Auxetic Honeycombs, Journal of Strain Analysis and Engineering Design, 35(5): 383-388.

Sigmund, O, Torquato, S   Composites with extremal thermal expansion coefficients APPL PHYS LETT 69 (21): 3203-3205 NOV 18 1996

Silva, M. J., Hayes, W. C. and Gibson, L. J., 1995, The Effects of Nonperiodic Microstructure on the Elastic Properties of Two-Dimensional Cellular Solids, International Journal of Mechanical Sciences, 11: 1161-1177.

Smith, F. C. and Scarpa, F., 2004. Design honeycomb-like composites for electromagnetic and structural applications. IEE Proceedings Vol. A, Science, Measurement and Technology, 151(1),(2003), 9-15.

Smith, F. C., Scarpa, F. and Chambers, B., 2000. Electromagnetic properties of re-entrant dielectric honeycombs. IEEE Microwave and Optical Technologies Letters, 10(11), p. 451-453.

Spadoni, A., Ruzzene, M. Scarpa, F., 2005. Global and local linear buckling behavior of a chiral cellular structure. Physica Status Solidi (b), special issue on negative Poisson's ratio, Volume 242, Issue 3, (p 695-709)).

Stalmans, R., 1999, Adaptive Hybrid Composites with a Focus on the Integration of Shape Memory Elements, in: Advances in Science and

Technology, 25: Smart Materials Systems, Ed. P. Vincenzini, Techna, Faenza (Italy), pp. 83-94

Stanway, R., 2001, Electrorheological and Magnetorheological fluids, Encyclopedia of Vibration, Academia Press.

Stanway, R., Sproston, J. L., and El-Wahed, A. K., 1996, Applications of Electro-Rheological Fluids in Vibration Control: A Survey, Smart Materials and Structures, Vol. 5, No. 4, pp. 464-482.

Sun, C.T. and Lu, Y. P., 1995, Vibration Damping of Structural Elements. Englewood Cliff, NJ: Prentice Hall.

Sypeck, D.J and Wadley, H., 2002, Cellular Metal Truss Core Sandwich Structures, Advanced Engineering Materials, Vol. 4, No.2, pp. 759-764.

Tamura, M., Yamguchi, T., Oyaba, T. and Yoshimi, T., Electroacoustic Transducers with Piezoelectric High Polymer Films, J. Audio Eng. Soc. , Vol. 23, No. 1, (1975), pp. 21-26.

Tasaka, S. and Miyata, S., Effects of Crystal-Structure on Piezoelectric and Ferroelectric Properties of CoPoly-(Vinylidenefluoride-Tetrafluoroethylene), J. Appl. Phys., Vol. 57, No. 3, (1985), p. 906-910.

Taylor, E. A., Herbert, M. K., Vaughan, B.A.M., McDonnell, 1999, Hypervelocity Impact on Carbon Fibre Reinforced Plastic/aluminium Honeycomb: Comparison with Whipple Bumper Shields, International Journal of Impact Engineering , Vol. 23, Part II, no. 1, pp. 883-893. Dec. 1999

Tobushi, H., Hashimoto, T., Hayashi, S., Yamada, E., J Intelligent Material Systems and Structures 1997, 8(8), 711–718.

Turner, T.L., Lach, C.L., Cano, R.J., 2001, Fabrication and Characterization of SMA Hybrid Composites, Smart Structures and Materials;SPIE Vol. 4333, Paper No. 4333-60

Tzou, H.S. & Fukuda, T., 1992, Precision Sensors. Actuators and Systems. Dordecht Kluwer Academic Publishers.

Tzou, H.S., 1993, Piezoelectric Shells. Dordrecht: Kluwer Academic Publishers.

Uchino, K., 1998, Shape Memory Ceramic, Otsuka & Wayman. Shape Memory Material. Cambridge University Press.

Uchino, K., 2000, Ferroelectric devices, Marcel Dekker, New York

Ullakko, K., Huang, J.K., Kantner, C., O'Handley, C. and Kokorin, V.V., Large Magnetic-Field-Induced Strains in Ni2MnGa single Crystals, Journal of Applied Physics Letters, 69 (1996), 1966-1968.

Wan, H., Ohtaki, H., Kotosaka, S. and Hu, G., 2004, A study of negative Poisson's ratios in auxetic honeycombs based on a large deflection model, European Journal of Mechanics - A/Solids, Volume 23, Issue 1, pp 95-106

Wang, L., & Wu, X, 2006, private conversation at Birminghan University on 27 March 2006.

Wang, T.T., Herbert, J, M. and Glass, A.M., (Ed.), The Applications of Ferroelectric Polymers, Chapman and Hall, New York (1988).

Warren, W. E. and Kraynik, A.M., 1987, Foam Mechanics: The Linear Elastic Response of Two-Dimensional Spatially Periodic Cellular Materials Mech. Mater. 6 27 31

Whitty, J. P. M., Alderson, A., Myler, P. and Kandola, B., 2003. Towards the design of sandwich panel composites with enhanced mechanical and thermal properties by variation of the in-plane Poisson's ratios. Composites A 34, 525-534

Winslow, W. M., 1949, Induced Fibrillation of Suspensions, Journal of Applied Physics, Vol. 20, pp. 1137.

Wojciechowski, K. W., 1989, Two-dimensional isotropic systems with a negative Poisson ratio', Physics Letters A137, 60-64

Wuttig, M., Li, J. and Craciunescu,C., A New Ferromaggnetic Shape Memory Alloy System, Scripta Materialia, 44 (2001), 2393-2397.

Yang, W., Li, Z.M., Shi,W., Xie,B.H., Yang, M.B., 2004, Review on auxetic materials, Journal of Materials Science, Volume 39, Number 10, pp. 3269 – 3279.

Yong Liu, Mechanical and Thermomechanical Properties of a $Ti_{50}Ni_{25}Cu_{25}$ Melt Spun Ribbon, Materials Science and Engineering A, Volume 354, Issues 1-2, 15 August 2003, Pages 286-291

Zak, A. J., Cartmell, M. P., Ostachowicz, W. M. and Wiercigroch, M., 2003, One-Dimensional Shape Memory Alloy Models for Use with Reinforced Composite Structures, Smart Mat. Struct., 12, pp. 338-346.

Zenkert, D., 1997, The Handbook of Sandwich Construction, Engineering Material Advisory Services Ltd, London.

Zhang, Q. M., Wang, H., Zhao, J., Fielding, J. T. and Newnham, R. E., 1996. A high sensitivity hydrostatic piezoelectric transducer based on transverse piezoelectric mode ceramic honeycomb. IEEE Transactions on Ultrasonics, Ferroelectrics and Frequency Control 45(1), 36-43)

Zipser L., Richter L., Lange U., 2001, Magnetorheologic fluids for actuators, Sensors and Actuators A: Physical, Volume 92, Number 1, 1 August 2001, pp. 318-325(8)

APPENDICES

Appendix A

Smart Materials

A1. Piezoelectric materials

Piezoelectric materials produce electrical charges when mechanically stressed. Conversely, an applied electric field can cause a piezoelectric material to change dimensions. The piezoelectric effect was discovered by the Curie brothers in 1880. The practical use of piezoelectric materials became possible with Paul Langevin's discovery in 1916 of the piezoelectric characteristics of quartz crystals. Following this discovery, it was observed that some crystalline materials demonstrate a spontaneous polarization along one axis of the crystal, ferroelectric behaviour. For many years, Rochelle salt was the only crystal that was known to have this ferroelectric property [Lines and Glass, 1977]. Among the natural materials with this property are quartz, human skin, and human bone, though the latter two have very low coupling efficiencies. Common industrial piezoelectric materials used for sensoring and actuators are polyvinylidene fluoride (PVDF) and lead zirconate titanate (PZT).

Piezoelectric materials can be classified in two further categories piezoelectric ceramics and piezoelectric polymers [Tzou,1993]. An example of an application for piezoelectric ceramics is in acoustic transducers converting acoustic waves into electric fields and vice versa [Newnham & Amin, 1999]. Piezoceramic transducers are found in telephones, HiFi music systems, and

musical instruments such as guitars and drums. They also find applications in clocks and watches [Uchino, 2000]. Piezoelectrics also have been embedded in skis in order to dampen amplitudes of deformations close to resonance helping keep the ski edges in contact with the snow [Newnham & Amin, 1999].

The existence of piezoelectric polymers was already known since 1924 [Culshaw et.al,1992]. However, the early known piezoelectric polymers did not receive much attention until the work by Fukada in the fifties and sixties [Fukada, 1964]. Fukada and his co-workers discovered that rolled films of polypeptides and numerous other polymers induce surface charges when stressed.

Piezoelectric polymers are produced by a variety of techniques, where in the case of PVDF [polyvinylidene fluoride] the material is mechanically drawn and polarized in order to form a useful transducer material. The drawing techniques include extrusion and stretching while the film material is subjected to a strong electrical polarization field. Without drawing, PVDF shows a very weak piezoelectric behaviour, the higher the molecular orientation the stronger the resultant response of the polarized film.

After polarization, PVDF exhibits considerably stronger piezoelectric response than most other known polymers [Kawai, 1969]. The discovery of the piezoelectric and later of the pyroelectric propeities of PVDF and the growing applications of this polymer [Tamura, 1975] sparked extensive research and

development activities. Some of the piezoelectric polymers that are known today include polyparaxylene, poly-bischloromethyuloxetane, aromatic polyamides, polysulfone, polyvinyl fluoride, synthetic polypeptide and cyanoethul cellulose [Wang et.al, 1988].

A2. Electrostrictive materials

The electrostrictive effect (dimensional change under the influence of applied field) is found in all materials although it is usually too small (approximately 10^{-5} to 10^{-8} of strain) for practical use [Gandhi and Thompson,1992]. Electrostrictive materials are not piezoelectric and possess no spontaneous polarisation. When correctly used they can be virtually loss free for bandwidths of hundreds of kHz. Electrostrictive ceramics, based on a class of materials known as relaxor ferroelectrics, however show strains comparable to piezoelectrics and have already found application in many commercial systems [Culshaw,1996].

The lack of a spontaneous polarisation means that electrostrictors display little or no hysteretic loss even at very high frequencies of operation. The advantages are however gained at the expense of temperature stability. Relaxors operate best in situations where the temperature can be stabilised to within approximately 10°C. This may seem extremely limiting at first glance, but given that electrostrictors excel at high frequencies and very low driving fields, then the applications tend to be in specialised micro actuators. Temperature stabilisation of such small devices is relatively simple and often

presents only a minor problem in the overall design and development process [Culshaw,1996].

Most commercial electrostrictive ceramics are based upon the classical relaxor ferroelectric PMN (lead magnesium niobate) and its doped derivatives. The most useful family of actuator materials are solid solutions of PMN and lead titanate (PT). PMN-PT materials are available from virtually all piezoelectric suppliers although they remain a minority low volume product in most cases.

The new class of electrostrictive polymeric materials offers high performance and flexibility in a cost-competitive device. They contain a flexible backbone polymer and grafted crystalline groups and offer high strain under an applied electric field better than previous electrostrictive polyurethane elastomers. The electrical, mechanical, and electromechanical properties can be tailored by varying the fraction of the polymer phases, their molecular weights, and their thermal treatments. Thin-film, electrostrictive polymers are prepared by film casting techniques. The films are conformable and can be readily packaged for applications like membrane surface accuracy control. The baseline materials exhibit excellent processing capabilities [Heydt et.al,2000].

A3. Magnetostrictive materials

Magnetostriction is defined as the dimensional change of a magnetic material caused by a change in its magnetic state and the reverse effect, by which an

applied stress causes a change in the material's magnetic state. All magnetic materials exhibit varying degrees of magnetostriction, however only some materials exhibit sufficient magnetostriction for practical use. Early magnetostrictive devices used nickel as the magnetostrictive core, this principle being used for the first sonar applications [Jones&Liang , 1996].

In the early 1960's the magnetostrictive properties of terbium and dysprosium were identified but, due to the low Curie temperatures of the two elements, they were not suitable for use at room temperature. To attempt to produce a material that would exhibit large magnetostriction at room temperature terbium and dysprosium were alloyed with transition metals. In 1971 this process led to giant magnetostriction at room temperature of the alloys $TbFe2$ and $DyFe2$ [Jenner et. al 1995]. Terfenol-D, which has the composition $Tb0.3Dy0.7Fe2$, provides a magnetostriction of over 1000×10^{-6}. When a specimen of Terfenol-D is placed near a magnet, the special rare-earth-iron material will change shape slightly. This rather remarkable phenomenon, which physicists call the magnetostriction effect, has been the focus of efforts by engineers at ETREMA Products Inc., to devise simple, high-reliability linear-motor-based actuators [Jones&Liang , 1996].

The design of these devices is straightforward. The basic concept consists of constricting a rod of Terfenol-D into a metal tube whose bore size is slightly smaller than the diameter of the rod. A series of electromagnetic induction coils are then wrapped around the tube (or stator) and used to generate a moving magnetic field that courses wavelike down the successive windings along the stator tube. As the travelling magnetic field causes each succeeding

cross section of Terfenol-D to sequentially elongate and contract when the field is removed, the rod would actually "crawl" down the stator tube like a worm. Repeated propagating waves of magnetic flux will then translate the rod along the length of the tube, producing a useful stroke and force output. The amount of motion generated by the material is proportional to the magnetic field provided by the coil system, which is a function of the electrical current. This type of motive device, which features a single moving part, is called an elastic-wave or peristaltic linear motor [Gandhi and Thompson, 1992].

Magnetostrictive materials can provide both actuating and sensing capabilities. When used as an actuator, a change in dimensions of the material is obtained by applying a magnetic field. The deformation of the material can then be controlled with high precision (10^{-1} to 10^{-3} μm). Moreover, the response is fast (within microseconds) and may deliver large output forces [Jenner et. al 1995].

A4. Electro-rheological fluids

Electro-rheological fluids (ERF) are fluids that experience dramatic changes in rheological properties in the presence of an electric field. Willis M. Winslow first explained the effect in the 1940s using oil dispersions of fine powders [Winslow, 1949]. The fluids are made from suspensions of an insulating base fluid and particles of the order of 10^{-1} to 10^{-2} μm in size. The electro-rheological effect, sometimes called the Winslow effect, is thought to arise from the difference in the dielectric constants of the fluid and particles. In the

presence of an electric field, the particles, due to an induced dipole moment, will form chains along the field lines. This induced structure changes the ERF viscosity, yield stress, and other properties, allowing the ERF to change consistency from that of a liquid to something that is viscoelastic, such as a gel, with response times to changes in electric fields on the order of milliseconds.

Control over a fluid's rheological properties offers the promise of new possibilities in engineering for actuation and control of mechanical motion. Any device that relies on hydraulics can benefit from ERF quick response times and reduction in device complexity [Bullough et al., 1993]. Early development of practical applications of ERF was hampered by the multidisciplinary approach required to understand them. Today's scientists continue to improve upon ERFs, making them with more desirable properties. Their solid-like properties in the presence of a field can be used to transmit forces over a large range and have found a large number of applications [Duclos et al., 1992]. Devices designed to utilize ERFs include shock absorbers, active dampers, clutches, adaptive gripping devices, and variable flow pumps [Bullough et al., 1993; Choi, 1999]. An engineering application of ERF's is vibration control and a good review of the subject can be found in [Stanway et al., 1996].

A5. Magnetorheologic fluids

Magnetorheologic fluids (MR fluids) are similar to ER fluids but they harden and become liquid when subject to magnetic field. They have ability to transform from liquid to solid and from solid to liquid in less than a second

[Richter et.al,2001]. The MR fluids consist of a suspension of magnetically soft particles in carrier liquids such as mineral or silicone oil. The particles sizes quoted in literature are generally smaller than those in ER fluids and lie in the range 0.1-10 μm [Stanway,2001]. MR fluids is activated through the application of magnetic field. This causes the particles to form chains, which link the poles. In consequence of it, the viscosity and the flow behaviour of the fluid are considerably changed. This reversible effect can be used in actuators, especially for controlled damping of shocks and vibrations, or in fluid devices for the electro-magnetical influencing of flows [Zipser et al., 2001]. It was used in the design of semi active suspension.

A6. Shape memory polymer

Shape-memory polymers (SMP) are easily formed, lightweight, provide large recoverable deformations, and show good processing performance. A shape memory polymer, like a shape-memory alloy, may remember its original shape after being deformed. When the SMP, after being deformed, is heated to a temperature higher than a predetermined one, the stress imposed on the shape-memory polymer is relieved, leading to the recovery of the original shape. In this sense, it is called a thermally stimulated shape-memory solid. The first SMP of practical importance was made out of polyethylene cross linked by the reaction with ionising radiation during processing (Ota, 1981). It was used for cable joint, tube joint, and goods packing. Its response temperature related to the melting temperature of polyethylene is usually near or above 120°C. Various kinds of shape memory polymers are needed to

match the requirements of different applications. Special attention has been put on lowering the response temperature of the shape-memory effect. A SMP of lower response temperature may be applied in daily life and may be important for applications of special biological or medical considerations, where the use of high temperature should be avoided. An important approach to solve this problem is the use of segmented copolymers, like in the work of Hayashi et.al (1997), where two series of different chemical structure and dynamic mechanical properties of polyurethane with shape memory behaviour have been considered.

A7. Shape memory ceramic

Ceramic shape memory has been reported for certain ferroelectricity related transitions, namely paraelectric-ferroelectric and antiferroelectric-ferroelectric transition [Uchino, 1998], Shape-memory ceramic (SMC) materials, which can be activated by an electric field instead of heat, are still at the developmental stage. SMCs look similar to piezoelectric ceramics, but the dimensional change is based on the phase-change from antiferroelectric to ferroelectric state. In the lead zirconate stannate based system, the longitudinal strain reaches more than 0.3%[Uchino, 2000] while in conventional piezoelectric or electrostrictive, the strain is about 0.1% .

In a ferroelectric material, an electric field can cause mechanical strain due to the polarization of the material. However, since antiferroelectrics contain two spontaneous sub lattices, very little strain is achieved when applying low

electric fields [Oh et al, 1990]. If the composition of an antiferroelectric material is close to the ferroelectric phase boundary, a phase transition from antiferroelectric to ferroelectric can be induced by the application of a large electric field. This phase transition is accompanied by a lattice distortion leading to a net volume expansion in the material. The isotropic expansion manifests itself as a sharp jump in the strain level of the material. As the electric field is reduced, the material may either return to its original state, or remain in the ferroelectric state (exhibiting shape memory), depending on the exact composition. The ceramics lacking shape memory are only stable in the antiferroelectric state at zero field, while those with shape memory are metastable in either of ferroelectric and antiferroelectric states at zero field. In the latter case, a field in the opposite direction must be applied to remove the residual strain.

A8. Ferromagnetic shape memory alloys

Ferromagnetic shape memory alloys are metals exhibiting both ferromagnetism and the shape memory effect. The materials constitute a new class of active solids combining the properties of ferromagnetism with those of a diffusionless, reversible martensitic transformation. These materials have been the subjects of recent studies due to the unusually large magnetostriction exhibited in the martensitic phase [Ullako et al, 1996].

Ferromagnetic shape memory alloys have attracted significant attention since the discovery of large magnetic-field-induced strain of several percent in Ni-

Mn-Ga alloy [Ullako et al, 1996]. This strain was attributed to the motion of the martensitic twins, and is different from the conventional (magnetoelastic) magnetostriction, making this type of solid an attractive candidate for a new class of magnetic actuator materials. Since then, various ferromagnetic shape memory alloys, e.g., Fe-Pd [Jemes et al, 1999], Fe-Pt [Kakeshita et al, 1984], Co-Ni-Al [Oikawa et al, 2001], Co-Ni-Ga [Wuttig et al, 2001] have been investigated. Apart from the practical interests, these materials also offer an excellent opportunity to investigate the various aspects of phase transformations and microstructural formation because magnetic and structural phase transformations can be realized in a single system. In Ni-Mn-Ga alloy, which is one of the prototypical ferromagnetic shape memory alloys, a high temperature cubic phase of this alloy has the L21 ordered structure, also known as the Heusler structure. The alloy has relatively high Curie temperature (~363 K), and changing chemical composition of the alloy can control the martensitic transformation temperature.

A9. Fibre optics

Fibre optics have found many uses in a variety of industries, especially in telecommunication industries. When an optical fibre is subjected to perturbations of different kind, it experiences geometrical (size, shape) and optical (refractive index, mode conversion) changes to a greater or lesser extent depending upon the nature and the magnitude of the perturbation. In fibre optic sensing, this response to external influence is deliberately enhanced so that the resulting change in optical radiation can be used as a

measure of the external perturbation. So the optical fibre serves as a transducer and converts measurement like temperature, stress, strain, rotation or electric and magnetic currents into a corresponding change in the optical radiation. Since light is characterized by intensity, phase, frequency and polarization, any one or more of these parameters may undergo a change. The usefulness of the fibre optic sensor therefore depends upon the magnitude of this change and our ability to measure and quantify the same reliability and accuracy.

Some of the advantages of fibre optic sensors are freedom from electro magnetic interference, wide bandwidth, compactness, geometric versatility and economy. In general, fibre optic sensors are characterized by high sensitivity when compared to other types of sensor. It is also passive in nature due to the dielectric construction. Fibre optic sensors can also be classified on the basis of their application. Firstly is a physical sensor, which used to measure physical properties like temperature and stress. The second is a chemical sensor, which used for pH measurement, gas analysis and spectroscopic studies. Finally as bio-medical sensors which used in bio-medical applications like measurement of blood flow and glucose content [MacCraith et.al, 1997].

Fibre Bragg gratings are one of popular sensors widely used in industry for measurement of deformation and temperature. The development of a fibre Bragg grating measuring system plays a significant role in monitoring and recording the actual seismic responses of underground structures, rock mass and bridges [Li, 2004].

Appendix B

Constitutive Modelling of Shape Memory Alloys

B.1 Mueller & Achenbach Model

The Muller-Archenbach model originally developed describes the time-dependent thermomechanical behavior of SMA wire. It is motivated by experimental evidence of the underlying micromechanics and the resulting mathematical structure is given by a set of differential algebraic equation. When a tensile loading has been carried out at martensite phase, it results in the transition of M+ and M- leading to elongation [Mueller & Archenbach, 1985]. The structure of M+ and M- as shown in Figure B2 .This was described as a phase transition in a crystal lattice structure. Figure B1 shows the behavior of these layers in a tensile test experiment. At low temperature, the structure in martensite stage, half layer M+ and the other M-. With the external tensile loading, it straightens the whole structure. At a critical load level, the M- will transform into M+ and contribute to a considerable length change.
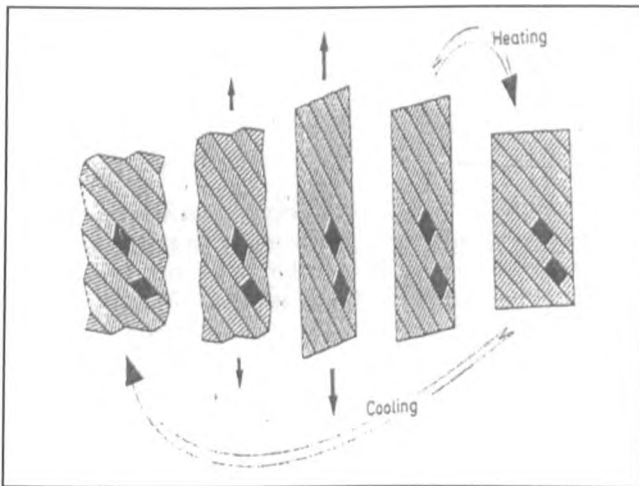

Figure B1   Transition model of martensite layer into austenite
[Archenbach 1989]

The total length change is calculated as the sum of the length changes of the individual layer.

$$D = N[x_A(\Delta_A) + x_+(\Delta_+) + x_-(\Delta_-)] \qquad \ldots \text{(b.1)}$$

From statistical thermodynamics, the average length change can be calculated as:

$$(\Delta_A) = \frac{\int_{-\Delta_s}^{+\Delta_s} \Delta \exp- \dfrac{\Phi(\Delta, P)}{kT} d\Delta}{\int_{-\Delta_s}^{+\Delta_s} \exp- \dfrac{\Phi(\Delta, P)}{kT} d\Delta} \qquad \ldots \text{(b.2)}$$

Where T is the temperature, k the Boltzmann's constant and $\Phi(\Delta, P)$ the Potential energy present in a layer.

The phase fractions, x_+ and x_- are defined according to:

$$\dot{x}_+ = -x_+ p^{+A} + x_+ p^{A+} \qquad \ldots \text{(b.3)}$$

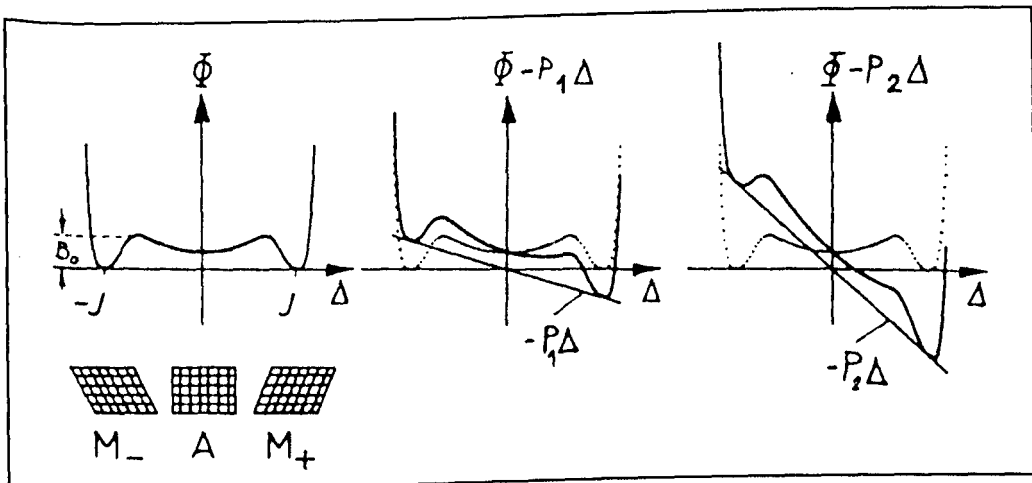$$\dot{x}_- = -x_- p^{-A} + x_+ p^{A-} \qquad \ldots \text{(b.4)}$$

Figure B2 : Lattice particle and coresponding potential energy [Archenbach 1989]

The quantity $p^{\alpha\beta}$ is the transition probability from α to β phase, which also can be calculated from statistical thermodynamics. In particular:

$$p^{+A} = \sqrt{\frac{kT}{2\pi m}} \frac{\exp{-\dfrac{\Phi(\Delta_s, P)}{kT}}}{\int_{+\Delta_s}^{+\infty} \exp{-\dfrac{\Phi(\Delta, P)}{kT}} d\Delta} \exp{\frac{A(1-2x_A)}{kT}} \qquad \text{... (b.5)}$$

Where A is the interfacial energy coefficient responsible for the alloy hysteretic behaviour and m the mass of the layer.

This axial extension enters the balance of energy, leads to:

$$mc\dot{T} = \alpha(T - T_E(t)) + j(t) - \dot{x}_+ H_+(P) - \dot{x}_- H_-(P) - A(1-2x_A)\dot{x}_A \qquad \text{... (b.6)}$$

B.2   Liang & Roger Model

There are 2 constitutive modelling of SMA that have been developed by Liang & Roger, the cosinus and exponential models [Liang & Roger 1990]. This thesis presents the cosinus model only, being the most used in phenomenological approaches. The original SMA model by Tanaka, which explains the relation between the stress, strain and martensite fraction has been modified by Liang & Roger (1990) as below:

$$\sigma - \sigma_0 = D(\varepsilon - \varepsilon_0) + \theta(T - T_0) + \Omega(\xi - \xi_0) \qquad \text{... (b.7)}$$

Liang & Roger have added the martensite fraction at the free stress condition for transformation from martensite to austenite, M-A and austenite to martensite, A-M as:

$$\xi = \frac{1}{2}\left\{\cos[a_A(T - A_s)] + 1\right\} \qquad \text{... (b.8)}$$

$$\xi = \frac{1}{2}\left\{\cos[a_M(T - M_f)] + 1\right\} \qquad \text{... (b.9)}$$

Constants for material a_A and a_M are given by,

$$a_A = \pi / (A_f - A_s)$$
$$a_M = \pi / (M_s - M_f)$$

$\qquad$ ... (b.10)

Therefore, the martensite fraction for stress induced in transformation from mertensite to austenite and transformation from austenite to martensite is given as:

$$\xi = \frac{\xi_M}{2} \left\{ \cos[a_A(T - A_s) + b_A \sigma] + 1 \right\}$$

$\qquad$ ... (b.11)

$$\xi = \frac{1 - \xi_A}{2} \cos[a_M(T - M_f) + b_M \sigma] + \frac{1 + \xi_A}{2}$$

$\qquad$ ... (b.12)

The constants I b_A and b_M are given by :

$$b_A = -\frac{a_A}{C_A}$$
$$b_M = -\frac{a_M}{C_M}$$

$\qquad$ ... (b.13)

The other phenomenological constants, C_A and C_M are defined as :

$\qquad C_M = \tan(\alpha)$

$\qquad C_A = \tan(\beta)$

$\qquad$ ... (b.14)

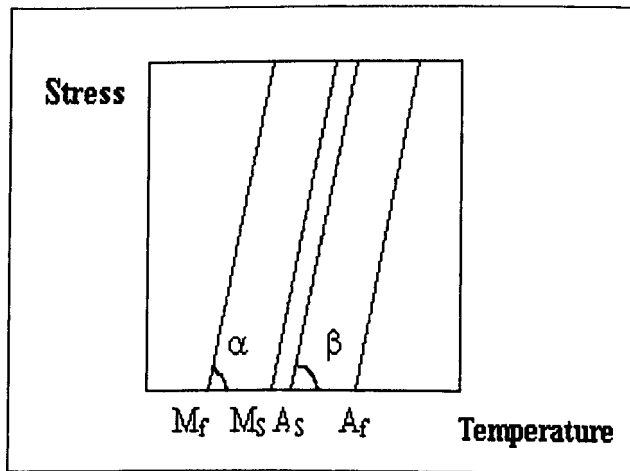With α and β providing the values of the angles shown in Figure B3

Figure B.3   Stress versus transformation temperature [Liang & Roger 1990]

B.3 Brinson Model

Brinson had suggested that the martensite fraction could be divided into two categories [Brinson 1992]:-

$$\xi = \xi_S + \xi_T \qquad \qquad \ldots\text{(b.15)}$$

Where ξ_T is the martensite fraction due to induced temperature, while ξ_S represents the martensite fraction due to stress induced, which has been transformed into detwinned martensite. This martensite has produced a strain in the shape memory alloy. Based on this fraction, Brinson had modified the Tanaka Model as below:

$$\sigma - \sigma_0 = D(\varepsilon - \varepsilon_0) + \Omega(\xi_S - \xi_{So}) + \Omega(\xi_T - \xi_{To}) \; \Theta(T - T_0) \qquad \ldots\text{(b.16)}$$

where σ, ε and T represent stress, strain and temperature. D is Young modulus of SMA, while Θs and Ω represent the thermoelastic and the phase transformation constants respectively. The relation between D, Ω and the strain recovery limit, ε_L is provided by:

$$\Omega = -\varepsilon_L D \qquad \qquad \ldots\text{(b.17)}$$

The equations for phase transformation for this model are represented in the following manner [Wong & Shinpoor 1996]-

i) Transformation to detwinned martensite (ξ_s)

a) For $T > Ms$ and $\sigma_s^{cr} + C_M(T - M_s) < \sigma < \sigma_f^{cr} + C_M(T - M_s)$

$$\xi_S = \frac{1 - \xi so}{2} \cos\left[\frac{\pi}{\sigma_s^{cr} - \sigma_f^{cr}} \left(\sigma - \sigma_f^{cr} - C_M(T - Ms)\right)\right] + \frac{1 + \xi so}{2} \qquad \ldots\text{(b.18)}$$

$$\xi_T = \xi_{T0} - \frac{\xi_{T0}}{1 - \xi_{s0}}(\xi_s - \xi_{s0}) = \xi_{T0}\left(\frac{1 - \xi_s}{1 - \xi_{s0}}\right) \qquad \ldots\text{(b.19)}$$

b) For $T < Ms$ and $\sigma_s^{cr} < \sigma < \sigma_f^{cr}$

155

$$\xi_s = \frac{1-\xi_{so}}{2}\cos\left[\frac{\pi}{\sigma_s^{cr}-\sigma_f^{cr}}\left(\sigma-\sigma_f^{cr}\right)\right]+\frac{1+\xi_{so}}{2} \qquad \ldots (b.20)$$

$$\xi_T = \xi_{T0} - \frac{\xi_{T0}}{1-\xi_{s0}}\left(\xi_s - \xi_{s0}\right)+\Delta_{T\xi} = \xi_{T0}\left(\frac{1-\xi_s}{1-\xi_{s0}}\right)+\Delta_{T\xi} \qquad \ldots (b.17)$$

c) If Mf < T < Ms and T < T$_0$

$$\Delta_{T\xi} = \frac{1-\xi_{To}}{2}\left[\cos(a_M(T-M_f))+1\right] \qquad \ldots (b.18)$$

ii) Transformation to austenite

For T > As and C$_A$(T-Af) < σ < C$_A$ (T-As)

$$\xi = \frac{\xi_0}{2}\left[\cos(a_A(T-As-\frac{\sigma}{C_A}))+1\right] \qquad \ldots (b.19)$$

$$\xi_s = \xi_{s0} - \frac{\xi_{s0}}{\xi_0}\left(\xi_0 - \xi\right)=\frac{\xi_{s0}}{\xi_0}\xi \qquad \ldots (b.20)$$

$$\xi_T = \xi_{T0} - \frac{\xi_{T0}}{\xi_0}\left(\xi_0 - \xi\right)=\frac{\xi_{T0}}{\xi_0}\xi \qquad \ldots (b.21)$$

σ_s^{cr} and σ_f^{cr} are the critical stress at the start and finish martensite transformation below

The constants a$_M$ and a$_A$ are indicated as,

$$a_A = \pi/(Af - As) \qquad \ldots (b.22)$$
$$a_M = \pi/(Ms-Mf) \qquad \ldots (b.33)$$

If the phase transformation effect is to be taken into account to describe the Young's modulus of the SMA 1D component, the following relationship can be used:

$$D = D_A + \xi(D_M - D_A) \qquad \ldots (b.34)$$

Where D_A was the Young Modulus at austenite and D_M was Young modulus at martensite.

APPENDIX C

Finite Element Program

C1. ANSYS programme for tensile test of Hexagonal Honeycomb

/TITLE, TWO-DIMENSIONAL DOUBLE WALL THICKNESS SMA
HONEYCOMB COMPRESSION TEST
!* Geometry build

```
*afun,deg
l=0.01
alpha=1
h=l*alpha
b=0.00467
beta=0.027
t=beta*l
Area=b*t
Area_2=b*t*2
Izz=(b*t**3)/12
Izz_2=(b*(2*t)**3)/12

theta=42

/prep7

k,,l*cos(theta),l*sin(theta)+(h/2)
k,,l*cos(theta),l*sin(theta)
k,,0,0
k,,0,-(h/2)
k,,2*l*cos(theta),0
k,,2*l*cos(theta),-(h/2)

l,1,2
l,2,3
l,3,4
l,2,5
l,5,6

lsel,s,line,,1
lsel,a,line,,2
lsel,a,line,,3
```

```
lesize,all,,,1
allsel,all
lsel,s,line,,3
lesize,all,,2,2
allsel,all


ET,1,BEAM23          ! Element type
r,1,Area,Izz,t
r,2,Area_2,Izz_2,2*t

MP,EX,1,23.5e10      ! Young's modulus
MP,PRXY,1,0.33       ! Poisson's ratio

TB,MELA,1,1,38,      ! Create a table of 38 data points
                     ! to map the stress-strain curve


TBPT,,.0,0           ! Data points
TBPT,,.0001,8.6e6
TBPT,,.0005,26e6
TBPT,,.001,41e6
TBPT,,.002,70e6
TBPT,,.004,113e6
TBPT,,.005,128e6
TBPT,,.006,138e6
TBPT,,.007,147e6
TBPT,,.008,152e6
TBPT,,.009,156e6
TBPT,,.01,160e6
TBPT,,.011,163e6
TBPT,,.012,165e6
TBPT,,.013,168e6
TBPT,,.014,170e6
TBPT,,.016,173e6
TBPT,,.02,180e6
TBPT,,.026,191e6
TBPT,,.03,199e6
TBPT,,.036,215e6
TBPT,,.04,227e6
TBPT,,.046,251e6
TBPT,,.05,270e6
TBPT,,.056,306e6
TBPT,,.06,334e6
TBPT,,.066,384e6
TBPT,,.07,421e6
TBPT,,.076,483e6
TBPT,,.08,527e6
```

```
!*meshing

/PREP7

lsel,s,,,1,5,2   !*additional
real,2
lmesh,all
allsel,all

lsel,u,,,1,5,2   !*additional
real,1
lmesh,all
allsel,all


!* generations in the x and y directions

nx=6
ny=4

KWPAVE,      6
CSYS,4
FLST,3,5,4,ORDE,2
FITEM,3,1
FITEM,3,-5
LSYMM,Y,all, , , ,0,0
allsel,all
lgen,nx,all,,,2*l*cos(theta),,,,0,0
allsel,all
lgen,ny,all,,,,2*l*sin(theta)+2*h,,,,0,0
allsel,all
nummrg,all
numcmp,all


nsel,s,loc,x,min_x
esln,s
emodif,all,real,1
allsel,all

nsel,s,loc,x,max_x
esln,s
emodif,all,real,1
allsel,all

dy=2*l*sin(theta)+2*h
dx=2*l*cos(theta)

LOCAL,11,0,(l/2)*cos(theta),(l/2)*sin(theta),0, , , ,1,1,
csys,11
```

```
*get,min_x,node,0,mnloc,x
*get,max_x,node,0,mxloc,x

*get,min_y,node,0,mnloc,y
*get,max_y,node,0,mxloc,y

l_y=(max_y-(h/2))-(min_y+(h/2))
l_x=max_x-min_x

!* Imposed displacements in the y direction

!* MAXIMUM IMPOSED STRAIN: str_fin

str_fin=15/100              !* change the strain value
n_strain=15                 !* Load step
*dim,load_y,array,n_strain,3     !* only one row (file written at every cycle in
APPEND mode)
del_str=str_fin/n_strain


NSEL,S,LOC,y,max_y
d,all,ux,0.0
NSEL,a,LOC,y,max_y-(h/2)
d,all,uy,del_str*l_y     !* Strain in Y direction
d,all,ux,0.0                    !* additional
allsel,all

nsel,s,loc,y,min_y
d,all,ux,0.0
d,all,uy,0.0
d,all,rotz,0.0
NSEL,a,LOC,y,min_y+(h/2)
d,all,ux,0.0
d,all,uy,0.0
d,all,rotz,0.0
allsel,all

finish

!* First loadstep

/solu

antype,static
nlgeom,on
pstres,on
solcontrol,on
autots,on
```

```
nsubst,10
lnsrch,on
outpr,basic,last
outres,all,all
cnvtol,rot
nsel,s,loc,y,max_y-(h/2)
d,all,uy,del_str*l_y
OUTRES,ALL,ALL
solve
lswrite,1
finish

allsel,all

/post1
set,last,last
csys,11
NSEL,S,LOC,y,max_y

NSEL,a,LOC,y,max_y-(h/2)
force,static
fsum
*get,Fy_eq,FSUM,0,item,fy
Area_s=l_x*b

sig_y=abs(Fy_eq)/Area_s
allsel,all

load_y(1,2)=sig_y
load_y(1,1)=del_str*l_y
load_y(1,3)=Fy_eq

fini

!* First results saved

*cfopen,hexa4,txt,,APPEND
*vlen,1
*vwrite,load_y(1,1),load_y(1,2),load_y(1,3)
(1x,3(E17.11,1X))
*cfclose

!* generations of loadsteps

*do,count,2,n_strain

        /solu
        antype,static
        nlgeom,on
        solcontrol,on
```

161

```
                pstres,on
                autots,on
                nsubts,10
                lnsrch,on
                outpr,basic,last
                outres,all,all
                cnvtol,rot
                !*nsel,s,loc,y,max_y-(h/2)
                nsel,s,loc,y,max_y-(h/2)
                d,all,uy,del_str*l_y*count
                allsel,all
                lswrite,count
                fini
      *enddo

      *do,count,2,n_strain
                /solu
                allsel,all
                antype,static
                lssolve,1,count
                fini
      /post1
      set,last,last
      csys,11
      NSEL,S,LOC,y,max_y
      NSEL,a,LOC,y,max_y-(h/2)
      force,static
      fsum
      *get,Fy_eq,FSUM,0,item,fy
      Area_s=l_x*b
      sig_y=abs(Fy_eq)/Area_s
      allsel,all
      fini

                load_y(count,1)=del_str*l_y*count
                load_y(count,2)=sig_y
                load_y(count,3)=Fy_eq
                allsel,all

      *cfopen,hexa4,txt,,append
      *vlen,1
      *vwrite,load_y(count,1),load_y(count,2),load_y(count,3)
      (1x,3(E17.11,1X))
      *cfclose

      *enddo
```

C2. ANSYS programme for tensile test of Re-entrance Auxetic Honeycomb

```
/TITLE, TWO-DIMENSIONAL SMA AUXETIC HONEYCOMB TENSILE TEST
!* Geometry build
*afun,deg
l=0.01
alpha=2
h=l*alpha
b=0.0043
beta=0.029
t=beta*l
Area=b*t
Izz=(b*t**3)/12

theta=-15

        /prep7

        k,,(l/2)*cos(theta),(l/2)*sin(theta)
        k,,l*cos(theta),l*sin(theta)
        k,,l*cos(theta),l*sin(theta)+(h/2)
        k,,2*l*cos(theta),0
        k,,(5/2)*l*cos(theta),(l/2)*sin(theta)
        k,,2*l*cos(theta),-(h/2)

        l,1,2
        l,2,3
        l,2,4
        l,4,5
        l,4,6

        lsel,s,line,,1
        lsel,a,line,,2,4,2
        lsel,a,line,,5

lesize,all,,,1
allsel,all
lsel,s,line,,3
lesize,all,,,2
allsel,all

ET,1,BEAM23              ! Element type
r,1,Area,Izz,t

MP,EX,1,23.5e10          ! Young's modulus
MP,PRXY,1,0.33           ! Poisson's ratio
```

```
TB,MELA,1,1,38,      ! Create a table of 38 data points
                     ! to map the stress-strain curve

TBPT,,.0,0           ! Data points
TBPT,,.0001,8.6e6
TBPT,,.0005,26e6
TBPT,,.001,41e6
TBPT,,.002,70e6
TBPT,,.004,113e6
TBPT,,.005,128e6
TBPT,,.006,138e6
TBPT,,.007,147e6
TBPT,,.008,152e6
TBPT,,.009,156e6
TBPT,,.01,160e6
TBPT,,.011,163e6
TBPT,,.012,165e6
TBPT,,.013,168e6
TBPT,,.014,170e6
TBPT,,.016,173e6
TBPT,,.02,180e6
TBPT,,.026,191e6
TBPT,,.03,199e6
TBPT,,.036,215e6
TBPT,,.04,227e6
TBPT,,.046,251e6
TBPT,,.05,270e6
TBPT,,.056,306e6
TBPT,,.06,334e6
TBPT,,.066,384e6
TBPT,,.07,421e6
TBPT,,.076,483e6
TBPT,,.08,527e6

!*meshing

/PREP7
LSEL,ALL
lesize,all,,,10
LMESH,ALL

!* generations in the x and y directions

nx=4
ny=4

KWPAVE,      6
CSYS,4
FLST,3,5,4,ORDE,2
FITEM,3,1
```

```
FITEM,3,-5
LSYMM,Y,all, , , ,0,0
allsel,all
lgen,nx,all,,,2*l*cos(theta),,,,0,0
allsel,all
lgen,ny,all,,,,2*l*sin(theta)+2*h,,,,0,0
allsel,all
nummrg,all
numcmp,all

dy=2*l*sin(theta)+2*h
dx=2*l*cos(theta)

LOCAL,11,0,(l/2)*cos(theta),(l/2)*sin(theta),0, , , ,1,1,
csys,11

*get,min_x,node,0,mnloc,x
*get,max_x,node,0,mxloc,x

*get,min_y,node,0,mnloc,y
*get,max_y,node,0,mxloc,y

l_y=(max_y-(h/2))-(min_y+(h/2))
l_x=max_x-min_x

!* Imposed displacements in the y direction
!* MAXIMUM IMPOSED STRAIN: str_fin

str_fin=20/100              !* change the strain value
n_strain=20                 !* Load step
*dim,load_y,array,n_strain,3    !* only one row (file written at every cycle in
APPEND mode)
del_str=str_fin/n_strain


NSEL,S,LOC,y,max_y
d,all,ux,0.0
NSEL,a,LOC,y,max_y-(h/2)
d,all,uy,del_str*l_y        !* Strain in Y direction
d,all,ux,0.0                !* additional
!*d,all,rotz,0.0
allsel,all

nsel,s,loc,y,min_y
d,all,ux,0.0
d,all,uy,0.0
d,all,rotz,0.0
NSEL,a,LOC,y,min_y+(h/2)
d,all,ux,0.0
d,all,uy,0.0
```

165

```
d,all,rotz,0.0
allsel,all

finish

!* First loadstep

/solu
antype,static
nlgeom,on
pstres,on
solcontrol,on
autots,on
nsubst,10
lnsrch,on
outpr,basic,last
outres,all,all
cnvtol,rot
nsel,s,loc,y,max_y-(h/2)
d,all,uy,del_str*l_y
OUTRES,ALL,ALL
solve
lswrite,1
finish
allsel,all

/post1
set,last,last
csys,11
NSEL,S,LOC,y,max_y
NSEL,a,LOC,y,max_y-(h/2)
force,static
fsum
*get,Fy_eq,FSUM,0,item,fy
Area_s=l_x*b
sig_y=abs(Fy_eq)/Area_s
allsel,all

load_y(1,2)=sig_y
load_y(1,1)=del_str*l_y
load_y(1,3)=Fy_eq

fini

!* First results saved

*cfopen,auxtens4,txt,,APPEND
*vwrite,load_y(1,1),load_y(1,2),load_y(1,3)
(1x,3(E17.11,1X))
*cfclose
```

166

```
!* generations of loadsteps

*do,count,2,n_strain

        /solu
        antype,static
        nlgeom,on
        solcontrol,on
        pstres,on
        autots,on
        nsubts,10
        lnsrch,on
        outpr,basic,last
        outres,all,all
        cnvtol,rot
        nsel,s,loc,y,max_y-(h/2)
        d,all,uy,del_str*l_y*count
        allsel,all
        lswrite,count
        fini
*enddo
*do,count,2,n_strain

        /solu
        allsel,all
        antype,static
        lssolve,1,count
        fini


/post1
set,last,last
csys,11
NSEL,S,LOC,y,max_y
NSEL,a,LOC,y,max_y-(h/2)
force,static
fsum
*get,Fy_eq,FSUM,0,item,fy
Area_s=l_x*b
sig_y=abs(Fy_eq)/Area_s
allsel,all

fini

        load_y(count,1)=del_str*l_y*count
        load_y(count,2)=sig_y
        load_y(count,3)=Fy_eq
        allsel,all


*cfopen,auxtens4,txt,,append
```

```
*vlen,1
*vwrite,load_y(count,1),load_y(count,2),load_y(count,3)
(1x,3(E17.11,1X))
*cfclose

*enddo
```

C3. ANSYS programme to calculate Poisson's Ratio of Chiral Honeycomb

```
finish
/clear,nostart
/title,Chiral Honey Comb 2D

/prep7

*afun,deg
*set,r1,6
*set,k,60
*set,t1,51.5102
*set,t2,25.0675
*set,s1,r1*60*3.142/180


!Geometry
!---------------

k,1,0,0,0
k,2,r1*sin(t1),r1*cos(t1),0
k,3,r1*sin(t1+k),r1*cos(t1+k),0
k,4,r1*sin(t1+2*k),r1*cos(t1+2*k),0
k,5,r1*sin(t1+3*k),r1*cos(t1+3*k),0
k,6,r1*sin(t1+4*k),r1*cos(t1+4*k),0
k,7,r1*sin(t1+5*k),r1*cos(t1+5*k),0

k,8,r1*sin(t2),r1*cos(t2),0
k,9,r1*sin(t2+k),r1*cos(t2+k),0
k,10,r1*sin(t2+2*k),r1*cos(t2+2*k),0
k,11,r1*sin(t2+3*k),r1*cos(t2+3*k),0
k,12,r1*sin(t2+4*k),r1*cos(t2+4*k),0
k,13,r1*sin(t2+5*k),r1*cos(t2+5*k),0

larc,2,9,1,s1
larc,9,3,1,s1
larc,3,10,1,s1
```

larc,10,4,1,s1
larc,4,11,1,s1
larc,11,5,1,s1
larc,5,12,1,s1
larc,12,6,1,s1
larc,6,13,1,s1
larc,13,7,1,s1
larc,7,8,1,s1
larc,8,2,1,s1

l,1,2
l,1,4
l,1,6

al,1,2,3,4,13,14
al,5,6,7,8,14,15
al,9,10,11,12,15,13

agen,2,1,3,1,0,-30,,,,0

agen,2,1,3,1,30*cos(-30),30*sin(-30),,,,0

agen,2,1,3,1,30*cos(210),30*sin(210),,,,0

l,4,52
l,11,51
l,40,22
l,41,21

l,26,31
l,25,33
l,9,34
l,2,35

al,5,59,61,62
al,46,63,64,24

al,29,65,66,37
al,1,67,68,39

kbetw,3,24
kbetw,10,23
kbetw,53,54
kbetw,3,53
kbetw,10,54
kbetw,3,56
kbetw,10,57

l,3,58

```
l,58,56
l,56,53
l,53,24

l,10,59
l,59,57
l,57,54
l,54,23

l,58,59
l,56,57
l,53,55
l,55,54

al,27,72,79,80,76
al,79,80,71,78,75
al,78,70,77,74
al,3,69,77,73

aglue,all


!meshing
!---------------

ET,1,plane183
keyopt,1,3,2
R,1,10!thickness

MP,EX,1,19e3                          ! Define austenite elastic properties
MP,NUXY,1,0.3                          !

TB,SMA,1,1                            ! Define material 1 as SMA,

TBTEMP,90                         ! Define first starting temp
TBDATA,1,475,620,380,290,0.03,0.5        ! Define SMA parameters
TBDATA,7,3e4

!TBTEMP,130                      ! Define first starting temp
!TBDATA,1,490,675,435,300,0.03,0.3        ! Define SMA parameters
!TBDATA,7,4e4

!TBTEMP,150                      ! Define first starting temp
!TBDATA,1,500,780,515,420,0.03,0.3        ! Define SMA parameters
!TBDATA,7,5e4

MP,EX,2,210e3
MP,NUXY,2,0.3
TB,BISO,2
TBDATA,1,300,0.0
```

```
esize,0.5

TYPE,1
MAT,2

amap,1,1,2,4
amap,2,1,4,6
amap,3,1,6,2
amap,4,19,14,18
amap,5,19,18,23
amap,6,19,23,14

amap,7,32,27,31
amap,8,32,31,36
amap,9,32,36,27
amap,10,45,40,44
amap,11,45,44,49
amap,12,45,49,40


TYPE,1
MAT,1

amesh,13,20,1


!Solution
!------------------

/solu

NLGEOM,1
tunif,90

dk,55,all

nsel,s,loc,x,-31.98076211
cp,1,ux,all
*get,nb,node,,num,min
allsel

nsel,s,loc,x,-31.98076211
cp,2,ux,all
*get,nb,node,,num,min
allsel

nsel,s,loc,y,6
cp,3,uy,all
*get,nm,node,,num,min
```

```
allsel

nsel,s,loc,y,-36
cp,4,uy,all
*get,nn,node,,num,min
allsel

antype,static
outres,all,all
deltim,0.1
kbc,0

        time,1
        d,nm,uy,2
        d,nn,uy,-2
        lswrite,1

        time,2
        d,nm,uy,2
        d,nn,uy,-2
        lswrite,2

lssolve,1,2,1

/post1
plnsol,s,eqv,1

/post26
ANSOL,2,na,S,Y,Sygma-y,1,1,plane183
NSOL,3,na,u,Y
XVAR,3
PLVAR,2,

ANSOL,2,na,S,Y
nprint,0.1
prvar,2

nsol,3,na,uy,y
nprint,1
prvar,3

nsol,4,na,ux,x
nprint,1
prvar,4

nsol,5,nb,ux,x
nprint,1
prvar,5
```
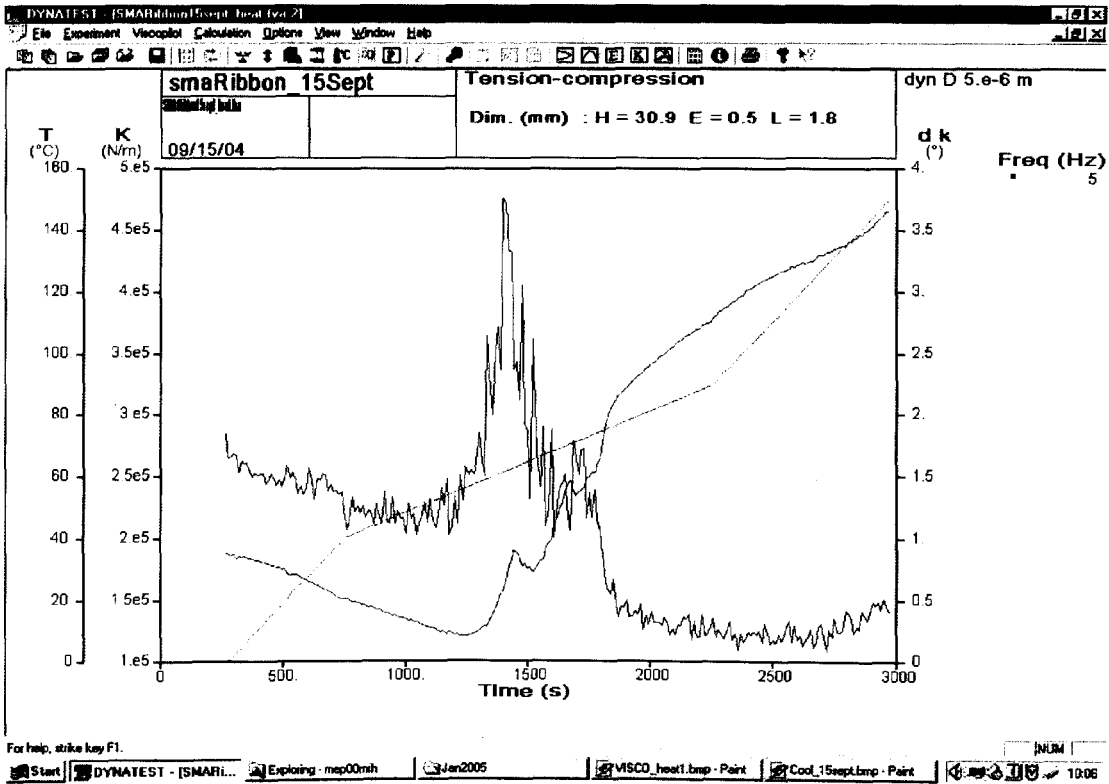
APPENDIX D

Figure D1 Result of viscoanalyser test for SMA ribbon (Heating)
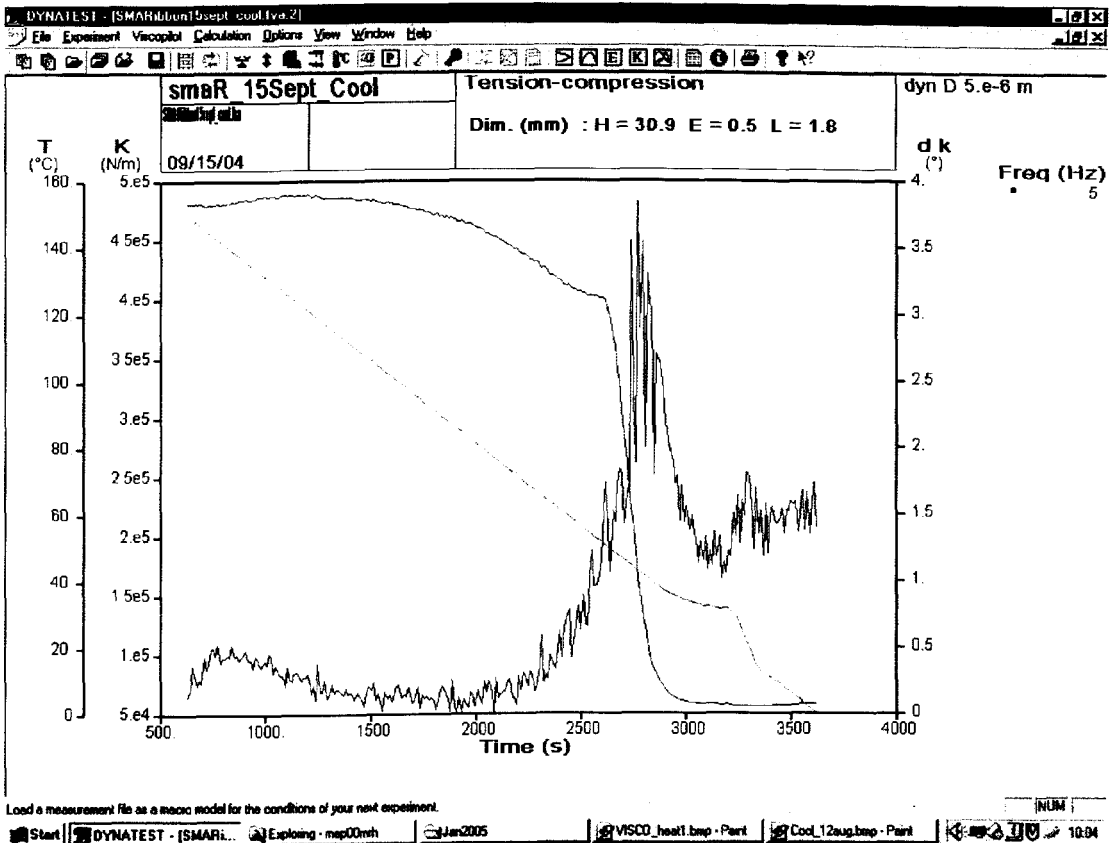

Figure D2 Result of viscoanalyser test for SMA ribbon (Cooling)

Matlab program for image processing

```
clear
clc
close all

[x19,map19]=imread('image08.jpg','jpg');
[x40,map40]=imread('image10.jpg','jpg');

%[x7,map7]=imread('picture 007.jpg','jpg');
%[x8,map8]=imread('picture 008.jpg','jpg');


i19= rgb2gray(x19);
i40= rgb2gray(x40);


[edge19, t19] = edge(i19,'canny');
[edge40, t40] = edge(i40,'canny');

%keyboard
[edge19_2, t19_2] = edge(i19,'canny',[0.03 0.0313]);
%[edge19_2, t19_2] = edge(i19,'canny',[0.027 0.029]);
[edge40_2, t40_2] = edge(i40,'canny',[0.027 0.029]);

figure(1)
grid
image(~edge19)
grid
colormap(gray(2))
%figure(200)
figure(2)
grid
image(~edge40)
grid
colormap(gray(2))
```

Matlab program for image processing

```
clear
clc
close all

[x19,map19]=imread('image08.jpg','jpg');
[x40,map40]=imread('image10.jpg','jpg');

%[x7,map7]=imread('picture 007.jpg','jpg');
%[x8,map8]=imread('picture 008.jpg','jpg');


i19= rgb2gray(x19);
i40= rgb2gray(x40);


[edge19, t19] = edge(i19,'canny');
[edge40, t40] = edge(i40,'canny');

%keyboard
[edge19_2, t19_2] = edge(i19,'canny',[0.03 0.0313]);
%[edge19_2, t19_2] = edge(i19,'canny',[0.027 0.029]);
[edge40_2, t40_2] = edge(i40,'canny',[0.027 0.029]);

figure(1)
grid
image(~edge19)
grid
colormap(gray(2))
%figure(200)
figure(2)
grid
image(~edge40)
grid
colormap(gray(2))
```

APPENDIX E

REVISION HISTORY

Rev. #.	E.C.O. #.	Description	Released By	Effective Date
1		Preliminary	D. Aslanidis G. Roebben	2002.06.08

1. DESCRIPTION

The current product is referred for shape memory applications with narrow hysteresis, high machinability and long actuation life. The product is wire with diameter in the range of 0.2 to 2.0 mm diameter and is made of Nitinol Alloy NTC05. The standard product is developed for actuations with high stiffness, high workability, high formability and high strength. They are available with either a standard oxide-free, an oxide-coated surface finish or a matte finish. The wire is supplied on spools or in specified cut lengths.

The @mt standard product description has the following format:

SME-ALLOY-[LOX, OX, SB, FA, FOX, TR]-XX.XX [DIAMETER]mm

where

SE refers to Super Elasticity
ALLOY   is notion for the type of the alloy i.e., NTC05
LOX: Smooth Light Oxidized
OX: Smooth Oxidized
SB: Rough Sand Blasted Wire
FA: Fully Annealed Wire
FOX: Free Oxide Wire
TR: Trained *or* otherwise Stabilized i.e., cycled under requested strain before delivery.
XX.XX   is for mm

2. APPLICABLE DOCUMENTATION

The following documents form a part of this specification to the extent specified herein:

AWI-0091   Mechanical Testing of Nitinol Wire
AWI-0126   Bending Wire Fatigue Testing

3. REQUIREMENTS

3.1   Material. The product shall be manufactured from @mt Nitinol Alloy NCT05 (Table 1).

3.2   Diameter. Diameter tolerance is based on flat micrometers (Table 1).

3.3　Mechanical Properties.　The tensile mechanical properties shall be per Table 1.

3.4　Cut Lengths and Ends.　The length is calculated from the weight per spool.　Specific lengths and tolerances shall be agreed with the customer.

3.5　Surface Finish.　The light oxide finish is very bright, smooth and free of contaminants wire. The oxidized wire shall be darker and the rough wire shall be grey and matte.

4.　QUALITY ASSURANCE

4.1　Lot Definition.　The same alloy batch under the same continuous processing conditions.

4.2　Responsibility for Inspection.　*@mt* is responsible for the performance of all tests specified herein.

4.3　Process Quality Control.　*@mt* takes all measures and actions to control, assure and record all quality information before and after utilisation.

5.　PACKAGING AND DELIVERY

5.1　Packaging Requirements.　Wire shall be coiled on spools or cut to specified lengths.

5.2　Labeling Requirements.　Each spool shall be labeled with the following:

　　　Date of Packaging
　　　Product Description
　　　Lot Number
　　　Quantity in meter *or/and* Kg

5.3　Certification.　All P.O. shall accompanied with a certificate of compliance with the following mnimum information:

　　　Date of Testing
　　　Customer Purchase Order Number
　　　Customer Part Number
　　　Product Description
　　　Order Number
　　　Lot Number
　　　Quantity in meter *or/and* Kg

5.4　Test Report.　When necessary, each shipment shall provide test data on the all characteristics shown in Table 1.

Table 1. Product Description

Chemical Composition

Element	Composition, WT%
Nickel	48 reference
Titanium	Balance
Copper	6
Carbon	0.050 MAX
Oxygen	0.050 MAX

Sizes

Diameter	Standard Tolerance	High Tolerance
0.200 mm< D<2.00 mm	±0.008 mm	±0.005 mm

Mechanical Properties

Tensile Parameters	Standard Product	
	+23°C	+90°C
Min Total Elongation to Failure (%)	35.0	25.0
Min Ultimate Tensile Strength over Loading Plateau Stress Ratio	1400	1000

Lot Identity

Lot Description	A	B	C
NTC05.A-B-C i.e., NTC05.10-05-12	Unique Ingot Number i.e., NTC05.10	Unique Coil Number i.e., NTC05.10-05	Unique Spool Number i.e., NTC05.10-05-12

ASTM Standards

Nitinol Alloy	Mechanical Testing	Transformation Temperatures	Others
F2063-00 F2005-00	F2082-00	F2005-00	

Material Characteristics of PowerWire (NTC05)

Physical Alloy Properties

Melting Point	1250°C
Density	6450 Kg/m^3
Electrical resistivity	Temperature, alloy and processing dependent
	80* 10^{-8} Ωm in Martensite
	90* 10^{-8} Ωm in Austenite
Thermal Conductivity	18 Wm^{-1}K^{-1}
Magnetic Susceptibility	2.4* 10^{-6} emu/g in Martensite
	3.7* 10^{-6} emu/g in Austenite
Magnetic Permeability	<1.002

Thermal Properties

Thermal Expansion Coefficient	6.6* 10^{-6} /°C in Martensite
	11* 10^{-6} /°C in Austenite
Specific Heat	490 J Kg^{-1} K^{-1}
dσ/dM$_S$	5 MPa/°C
Transformation Enthalpy	20000 J Kg^{-1}

Transformations

Austenite → R-Phase (R)
R-Phase → Martensite (M)
Martensite ↔ R-Phase (R')
R-Phase *or* Martensite ↔ Austenite (A)

[Formation of R-phase depending on the ageing temperature, time and cold working.]

Fully Annealed Condition (800°C_15min_WQ)

A$_s$		75°C
M$_s$		70°C
Temperature (°C)	*Range*	*Typical*
A$_s$	50-60	55
A$_p$	70-80	75
A$_f$	75-85	80
M$_s$	50-60	55
M$_p$	35-45	35
M$_f$	20-35	25
Hysteresis (A$_s$ - M$_f$)		*25-30*

Mechanical Properties

E-modulus	15 GPa in Martensite
	30 GPa in Austenite
Ultimate Tensile Stress	1000 MPa in Martensite
	650 MPa in Austenite
Total Elongation to Fracture	Above 32 % in Martensite
	Less than 27 % in Austenite
Loading Plateau Stress at 4% strain	450-600 MPa at 75°C

Alloy Functionality

Shape Memory Effect (SME)

Strain Recovery after 8% total deformation	95% (between +70°C and +100°C)
Strain Recovery after 4% total deformation	100% (between +70°C and +100°C)

Fatigue Life

- High fatigue life is guaranteed for strain less than 4% and stresses less than 150 MPa.
- Higher stability is guaranteed with a training process.

Comment: Fatigue results are depending on the applied strain, stress, temperature, frequency and sample dimensions.

Corrosion resistance

Resistant in environments such as the atmosphere, fresh and seawater, neutral salts and alkaline media.

Fabrication

Consistent high level of formability.   Mechanical joining techniques are preferred; crimping, swaging can be used.

Welded nitinol joints are usually brittle unless the material is subjected to a stress-relief heat treatment. In most cases, this heat treatment needs to happen at elevated temperature that seriously alters, if not wipes out, both shape memory and superelastic properties. TIG, electron-beam, plasma techniques can be used with the above reservations.
A protective inert atmosphere shall be used as well during the welding process.

Although machining is very difficult and creates a lot of tool wear, nitinol can be machined using conventional machining equipment and techniques: milling, turning, grinding, etc. Carbide tooling is strongly recommended.

It can be successfully coated with copper, nickel, gold and silver platings.

Typical Alloy Description

Every alloy is described as following

NTC05.26-01-09

Wire batch number

Rod number

Heat number

Alloy number
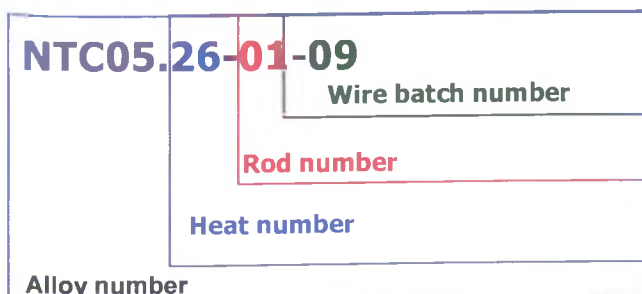
Where **NT** stands for a binary Ni-Ti, and NTX for a ternary **NiTiX** with X as an alloying element i.e. C stands for copper. If the alloy is only binary then X is omitted.
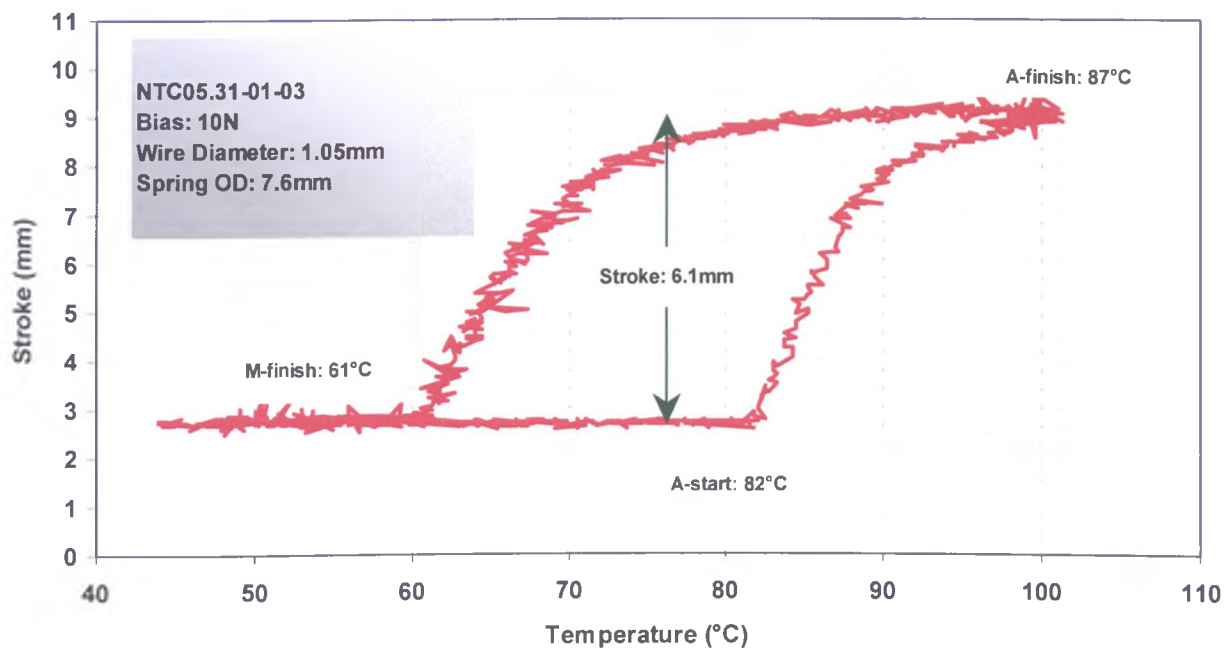
EXAMPLE: NTC05.26.01-09 is a NiTiCu alloy with a specified composition (ratio Ni:Ti:Cu, NTC05), from heat 26, part of rod 01, and produced as wire from coil 09.

Surface Finish Conditions

Standard	Light oxide (light straw colour)
Oxide coated	Dark oxide layer
Sandblasted	Grey and matte
Pickled	Grey and matte, smoother than sandblasted
Tailor made surfaces	Please consult the plant for further information

Typical Shape Memory Actuator based on NTC05 alloy

NTC05.31-01-03
Bias: 10N
Wire Diameter: 1.05mm
Spring OD: 7.6mm

A-finish: 87°C

Stroke: 6.1mm

M-finish: 61°C

A-start: 82°C

Typical Parameters of Shape Memory Actuator Design

Do-b
Dm-b
Di-b

δ

Do
Dm
DI

Cold form

Hot form